

Technische Universität Dresden

Impedance Sensors for Fast Multiphase Flow Measurement and Imaging

Dipl.-Ing. Marco Jose da Silva

von der Fakultät Elektrotechnik und Informationstechnik der
Technischen Universität Dresden

zur Erlangung des akademischen Grades eines

Doktoringenieurs

(Dr.-Ing.)

genehmigte Dissertation

Vorsitzender: Herr Prof. Dr.-Ing. habil. J. Czarske

Gutachter: Herr Prof. Dr.-Ing. habil. G. Gerlach

Herr PD Dr.-Ing. habil. U. Hampel

Herr Prof. Dr. W. Yang

Tag der Einreichung: 05.05.2008

Tag der Verteidigung: 11.08.2008

Technische Universität Dresden

Impedance Sensors for Fast Multiphase Flow Measurement and Imaging

Marco Jose da Silva, M.S.E.E.

Electrical and Computer Engineering Department at the
Technische Universität Dresden

to receive the academic degree

Doktoringenieur

(Dr.-Ing.)

approved dissertation

Chairman: Prof. Dr.-Ing. habil. J. Czarske

Referees: Prof. Dr.-Ing. habil. G. Gerlach

PD Dr.-Ing. habil. U. Hampel

Prof. Dr. W. Yang

Submission: 05.05.2008

Public defense: 11.08.2008

"And though I have the gift of prophecy, and understand all mysteries, and all knowledge; and though I have all faith, so as to remove mountains, but have not love, I am nothing."

(I Corinthians 13:2, The Bible)

Information about the electronic version of this thesis

This PhD thesis has also been published as book ISBN 978-3-940046-99-4 by TUDpress (<http://www.tud-press.de>) in the series "Dresden Contributions to Sensor Technology" edited by Prof. G. Gerlach.

Abstract

Multiphase flow denotes the simultaneous flow of two or more physically distinct and immiscible substances and it can be widely found in several engineering applications, for instance, power generation, chemical engineering and crude oil extraction and processing. In many of those applications, multiphase flows determine safety and efficiency aspects of processes and plants where they occur. Therefore, the measurement and imaging of multiphase flows has received much attention in recent years, largely driven by a need of many industry branches to accurately quantify, predict and control the flow of multiphase mixtures. Moreover, multiphase flow measurements also form the basis in which models and simulations can be developed and validated.

In this work, the use of electrical impedance techniques for multiphase flow measurement has been investigated. Three different impedance sensor systems to quantify and monitor multiphase flows have been developed, implemented and metrologically evaluated. The first one is a *complex permittivity needle probe* which can detect the phases of a multiphase flow at its probe tip by simultaneous measurement of the electrical conductivity and permittivity at up to 20 kHz repetition rate. Two-dimensional images of the phase distribution in pipe cross section can be obtained by the newly developed *capacitance wire-mesh sensor*. The sensor is able to discriminate fluids with different relative permittivity (dielectric constant) values in a multiphase flow and achieves frame frequencies of up to 10 000 frames per second. The third sensor introduced in this thesis is a *planar array sensor* which can be employed to visualize fluid distributions along the surface of objects and near-wall flows. The planar sensor can be mounted onto the wall of pipes or vessels and thus has a minimal influence on the flow. It can be operated by a conductivity-based as well as permittivity-based electronics at imaging speeds of up to

10 000 frames/s. All three sensor modalities have been employed in different flow applications which are discussed in this thesis.

The main contribution of this research work to the field of multiphase flow measurement technology is therefore the development, characterization and application of new sensors based on electrical impedance measurement. All sensors present high-speed capability and two of them allow for imaging phase fraction distributions. The sensors are furthermore very robust and can thus easily be employed in a number of multiphase flow applications in research and industry.

Acknowledgments

This work is the result of my research activities at the Institute of Safety Research, Forschungszentrum Dresden-Rossendorf e.V. (FZD), Germany, between 2004 and 2007. I would like to thank all the people who have made my work with this thesis easier, better and more fun.

First and foremost, I would like to thank God for giving me wisdom and guidance throughout my life.

I am extremely grateful to my supervisor at FZD, Dr. Uwe Hampel, for his support, orientation and friendship during these years. He has provided me with the opportunity to work on interesting current scientific and engineering topics.

I also express my deeply gratitude to my supervisor at TUD, Prof. Gerald Gerlach, for accepting me as one of his PhD students and also for the support, orientation and kind assistance along these three years.

I am indebted to Prof. Wuqiang Yang from the University of Manchester, UK for accepting to be the external referee for this thesis, Prof. Frank-Peter Weiss for welcoming me in his Institute at FZD and Prof. Barry Azzopardi from the University of Nottingham, UK, for giving me the opportunity of testing the wire-mesh sensor in the inclined pipe rig and also for showing me some insights of multiphase flows.

Throughout my time at FZD, I could count on many colleagues, who had always a hand disposed to help, an ear to hear or a good advice to give. Ecki, Martin, Tobias, Friedel, and the co-fighters PhD students Andre, Martina, Christophe, and Frank, I thank you all for the support, help and friendship. I was also very lucky to have had the chance to supervise Falk, Egginhard and Sebastian in their diploma thesis. Thank you very much indeed for the good team work. I also thank all colleagues from FWSF and FWSS divisions at FZD.

Many thanks also to my family and friends who are fortunately too many to mention by name and too good for not blaming me by not doing this. They have always prayed for me, helped and supported me as best as they could. *À minha família e amigos do Brasil, minha gratidão, estima e amor para sempre.*

Finally, I would like to thank two very special persons to me: my wonderful wife, Elisabeth, for her constant support, encouragement, comprehensiveness and love, without her support none of this work would have been accomplished; and my little daughter Ana Maria, who was born in the final phase of this work, for always be drawing my attention to the real important things in the world.

The financial support of the Brazilian foundation "Coordenação de Aperfeiçoamento de Pessoal de Nível Superior" (CAPES), Brasilia, in the form of doctoral grant is gratefully acknowledged.

Dresden, September 2008

Marco Jose da Silva

Contents

Abstract.....	i
Acknowledgments.....	iii
Contents	v
Nomenclature	ix
1 Introduction	1
1.1 Motivation.....	1
1.2 Objectives.....	3
1.3 Thesis outline	4
2 Principles of multiphase flow measurement.....	5
2.1 Multiphase flow	5
2.1.1 Flow patterns.....	6
2.1.2 Modeling of multiphase flow	10
2.2 State-of-the-art multiphase flow measuring techniques.....	11
2.2.1 Phase fraction measurement	12
2.2.2 Tomographic flow imaging.....	20
2.2.3 Wire-mesh sensor	25
2.2.4 Other techniques.....	28
2.2.5 Overview	29
2.3 Conclusions.....	31
3 Electrical impedance measurements in fluids	33
3.1 Electrical properties of fluids.....	33
3.1.1 Definitions: impedance and complex permittivity	33
3.1.2 Dielectric relaxation.....	38

3.2	Impedance measuring techniques.....	41
3.2.1	Overview.....	41
3.2.2	Low-frequency methods	43
3.3	The auto-balancing bridge.....	46
3.3.1	Circuit analysis	46
3.3.2	Simple measuring cell.....	49
3.4	Conclusions.....	52
4	Complex permittivity needle probe.....	53
4.1	Introduction.....	53
4.2	System description.....	54
4.2.1	Needle probe	54
4.2.2	Measuring electronics.....	56
4.2.3	Complex permittivity measurement.....	57
4.3	Measurement uncertainty	58
4.4	Application to flow measurement	60
4.4.1	Three-phase flow.....	60
4.4.2	Two substances mixing experiment.....	62
4.5	Conclusions.....	65
5	Capacitance wire-mesh sensor	67
5.1	Introduction.....	67
5.2	System description.....	68
5.2.1	Sensor and measuring electronics	68
5.2.2	Permittivity measurement	71
5.3	Numerical field simulation.....	74
5.3.1	Model description and voltage distribution.....	74
5.3.2	Crossing point capacitance.....	76
5.3.3	Spatial sensitivity.....	77
5.4	System evaluation.....	79
5.4.1	Measurement uncertainty	80
5.4.2	Time response	82
5.4.3	Comparison with conductivity wire-mesh sensor	83
5.4.4	Influence of liquid conductivity.....	85

5.5	Application to flow measurement	87
5.5.1	Oil-air stagnant two-phase flow	87
5.5.2	Oil-air vertical pipe flow	88
5.5.3	Three-phase flow	94
5.6	Conclusions	96
6	Planar array sensor	99
6.1	Introduction	99
6.2	Interdigital array sensor	100
6.3	Conductivity-based planar sensor	102
6.3.1	System description	102
6.3.2	Data processing	103
6.3.3	System evaluation	105
6.3.4	Measurement of a buoyancy-driven flow	108
6.3.5	Fluid distributions in a fluid coupling	112
6.4	Permittivity-based planar sensor	116
6.4.1	System description	116
6.4.2	Permittivity measurement	117
6.4.3	System evaluation	119
6.4.4	Two substances mixing measurement	123
6.5	Conclusions	125
7	Conclusions	127
7.1	Conclusions	127
7.2	Outlook	128
	References	131
	Appendix A – List of author's publications	145
	Appendix B – Electromagnetic theory	147
B.1	Maxwell's equations	147
B.2	Polarization	150
B.3	Debye relaxation model	152

Nomenclature

Roman symbols*

A	Area	m^2
a, b	Proportionality factors	-
A, B, C, D	Proportionality factors (complex)	-
B	Susceptance	S
C	Capacitance	F
c	Concentration	vol%
$C(i,j)$	Reference point for calibration	-
D	Dielectric displacement	C/m^2
d	Distance	m
E	Electrical field	V/m
f	Frequency	Hz
G	Conductance	S
g	Gravity acceleration vector	m/s^2
h	Liquid level	m
I	Radiation intensity	W/m^2
I	Electrical current	A
i, j	Spatial indices	-
j	Imaginary unit $\sqrt{-1}$	-
k	Temporal index	-
k_g	Geometry factor	m
l	Size of simple cell	m
M	modulus function	-

* Note that in this thesis the bold-faced variables such as **Z** or **ε** represent a complex quantity or a vector.

N	Number of wires/time steps	-
P	Polarization density	C/m ²
P_k	phase indicator function of phase k	-
Q	Volumetric flow rate	m ³ /s
R	Resistance	Ω
s	Slip ratio	-
s	Complex frequency	
T	Time interval	s
T	Temperature	K (°C)
t	Time	s
U	Velocity	m/s
$U(x)$	Uncertainty of quantity x	-
V	Voltage	V
w	Wetting level	-
x	Position vector	m
X	Reactance	Ω
Y	Admittance	S
Z	Impedance	Ω
z	Water thickness	m

Greek symbols

$\Delta\varepsilon$	Maximal deviation from the mean value	-
Γ	Boundary	
α	Void fraction	-
β	Parameter of Cole-Cole equation	-
χ_e	Electric susceptibility	-
δ	Relative deviation from a reference value	-
ε	Electric permittivity	-
γ	Penetration depth	m
κ	Admittivity	S/m
μ	Absorption coefficient	m ⁻¹
μ	Magnetic permeability	-
θ	Angle	rad, °

ρ	Density	g/m^3
ρ	Electric charge density	C/m^3
σ	Conductivity	S/m
τ	Time constant	s
ω	Angular frequency	rad/s
ω	Rotational speed	s^{-1}

Subscripts

A	Air
a	Absolute
b	Benzene
c-s	Cross-sectional averaged
eff	Effective
G	Gas
H	High
i	Isopropanol
L	Liquid
L	Low
m	Mixture
O	Oil
r	Ressonace
s	Stray, Static
t	Threshold
W	Water
x	Unknown

Abbreviations

ac	Alternating current
ADC	Analog-to-digital converter
CFD	Computational fluid dynamics
CT	Computed tomography
DAQ	Data acquisition
dc	Direct current

DDS	Direct digital synthesizer
ECT	Electrical capacitance tomography
EIT	Electrical impedance tomography
EMT	Electromagnetic tomography
ERT	Electrical resistance tomography
FEM	Finite element method
FET	Field effect transistor
fps	Frames per second
FZD	Forschungszentrum Dresden-Rossendorf e.V.
IC	Integrated circuit
LDA	Laser Doppler anemometry
MRI	Magnetic resonant imaging
PC	Personal computer
PCB	Printed-circuit board
PDF	Probably density function
PEPT	Positron emission particle tracking
PET	Positron emission tomography
PIV	Particle image velocimetry
RAM	Random access memory
rf	Radio frequency
rpm	Rotations per minute
S	Switch
S/ \bar{H}	Sample-and-hold
TUD	Technische Universität Dresden
USB	Universal serial bus
μ C	Microcontroller

1 Introduction

This opening chapter presents the motivation and objectives of the thesis as well as summarizes the contents of further chapters.

1.1 *Motivation*

The importance of metrology in all fields of science and technology cannot be overstated. It provides experimental data on which theories are developed, and then accepted or rejected. In addition, metrological activities, such as testing and measurement, are valuable inputs to monitor and control properties of objects and behavior of processes in industrial applications.

This thesis contributes to the science of measurement and is concerned with the use of impedance measurement techniques and data processing to visualize and quantify flow of multiphase mixtures.

Multiphase flow denotes the simultaneous flow of two or more physically distinct and immiscible substances. The main characteristics of a multiphase system are the presence of phase boundaries. Hence, not only mixtures of substances in different aggregate states (i.e. gas, liquid or solid), such as gas-liquid mixtures, but also mixtures of immiscible substances of the same aggregate state, such as oil-water mixtures, are subsumed under this term.

Multiphase flows are important in a broad range of engineering disciplines, in a wide spectrum of industrial applications, and in many other scientific fields such as biology, chemistry, meteorology and physics (Crowe 2006). From environmental phenomena to chemical processes and power generation, multiphase flow can be found everywhere. Common technology-relevant examples are found in nuclear engineering, where steam-water two-phase flows occur in light water reactors, in the crude oil extraction and processing, where three-phase air-oil-water flow is

encountered in the wells, risers, and in pipelines that carry the fluids, and in chemical process engineering with different multiphase flow occurring in reactors, bubble columns, pipework and plant components. In all these cases, multiphase flows determine the efficiency and safety of processes and plants. Therefore, the correct control and prediction of such flows is crucial for efficiency and safe operation of systems.

While single phase flow is relatively well understood and many different measuring techniques and commercial solutions for single phase flow meters are available, multiphase flow being a complex phenomenon is much more difficult to model, predict and measure (Hewitt 1978). Thus, there has been an increasing need from both industry and academia for measuring techniques which allow the direct knowledge of flow parameters in multiphase systems:

- as source of reliable data for the better understanding of such flows as well as for the validation of computational simulations,
- to enable improved design and increased operational efficiency of existing and new processes and equipments, and finally
- for the online monitoring and control of processes and devices where such multiphase flow occurs.

As a consequence of this large interest, a considerable number of measuring techniques have been developed and used in the past to investigate multiphase flows. However, none of the proposed techniques can claim a universal applicability and some of them have considerable drawbacks and may fail in particular practical situations.

The motivation for the work presented in this thesis is to develop and implement innovative impedance sensors to be applied in the measurement and imaging of multiphase flows which may fulfill the gap left open by current measuring techniques. Impedance sensors, in which the measurand causes a variation of an electrical characteristics such as resistance or capacitance, have found widespread use in industrial applications mainly due to their simplicity, low fabrication costs and robustness (Pallas-Areny and Webster 2001). Impedance measurement is a common tool for the characterization of electrical properties of materials and substances, for instance in analytical chemistry or material science, in which measurement times of seconds to minutes are used to achieve high measurement accuracy in the analysis of

sometime fully unknown substances. In process diagnostics, measuring times in the range of microseconds are required to investigate instationary flow phenomena. Moreover, the substances involved (and consequently their electrical properties) are known *a priori*.

1.2 Objectives

The main goal of the present work is to investigate and develop innovative impedance sensors for the investigation of multiphase flows. Impedance measurements in multiphase mixtures allow individual phases to be distinguished from each other based on their different specific electrical properties (e.g. conductivity or permittivity). Besides of the possibility to investigate the phases of fluid mixtures, imaging of impedance structures and consequently the visualization of the structure of flows and processes may be achieved by the use of multichannel systems and proper data processing. This thesis is, thus, primarily focused on the development of novel sensor systems, measuring electronics as well as data processing routines for the measurement and imaging of multiphase flow phenomena, mainly focused on gas-liquid multiphase flows. One challenge in achieving this objective is the need for sensors and instruments which are able to perform high-speed measurements. As flow velocity increases, flow structures change from stationary to instationary and may present transient character. In order to investigate the dynamics of transient multiphase flows, typical measurement repetition frequencies of up to 10 kHz must be reached.

In accomplishing these objectives, specifically, three different sensor systems have been developed and tested:

- (i) a complex permittivity needle probe for local flow measurement,
- (ii) a capacitance wire-mesh sensor for the cross-sectional imaging of pipe flows,
and
- (iii) a planar array sensor for the visualization of fluid distributions and near-wall flows.

1.3 Thesis outline

The thesis is organized as follows.

The aim of chapters 2 and 3 of this thesis is to give an overview of the areas of multiphase flow measurement as well as the theory of electrical impedance of fluids and its measurement. Chapter 2 gives a short review on multiphase flow and an overview of state-of-the-art measuring techniques. Chapter 3 describes the theory of electrical properties of fluids; the concepts of impedance and complex permittivity are introduced and the current impedance measurement methods are described. This chapter also presents preliminary impedance measurements in fluids with a simple probe.

The following three chapters 4 to 6 introduce the above-mentioned newly developed sensors along with the evaluation of each sensor system. Furthermore, some applications of each sensor in the investigation of flow phenomena are also presented. Thus, in chapter 4 the novel needle probe based on complex permittivity for local flow measurement is described. Chapter 5 depicts the capacitance wire-mesh sensor which allows the imaging of multiphase flows with high spatial and temporal resolution. Finally, chapter 6 introduces a new planar array sensor for the visualization of fluid distributions along the surface of vessels.

The thesis finishes in chapter 7 with conclusions, a discussion of main results obtained and suggestions for future work.

Some parts of the work described in this thesis are based on papers which were already published in international journals and conferences. The papers are properly cited in the text of the thesis and were included in the references. Furthermore, a consistent list of these papers can be found in Appendix A.

2 Principles of multiphase flow measurement

The objective of this chapter is to provide a background to the work presented in this thesis in which measuring methods using impedance sensors are developed to investigate multiphase flows. The chapter starts with an explanation of some essentials of multiphase flows. The current state of the art in multiphase flow measuring technology is then described including information on design, application, advantages and disadvantages of some selected instruments. The chapter will focus on the discussion of gas-liquid flows occurring in pipes as they are most common for industrial applications.

2.1 *Multiphase flow*

As stated earlier, multiphase flow is a general term that describes multiple fluid components in a flowing stream. The main characteristic of multiphase flows is the presence of phase boundaries arriving from two or more physically distinct and immiscible substances. In industrial applications, multiphase flows are typically constrained to pipes or vessels. The so-called phases may be gas, solid or liquid, and each may be a mixture of one or more components. In this way, basically four different types of multiphase mixtures may be identified (Crowe 2006, Brennen 2005).

- Gas-liquid flow is found, for instance, in boiling and condensation operations and inside many pipelines.
- Gas-solid flow may occur in a fluidized bed and in the pneumatic conveyance of solid particles.
- Liquid-solid flow takes place during the flow of suspensions such as river bed sediments and coal-water slurry.

- Immiscible liquid-liquid flow happens, for example, as oil-water emulsions in the chemical industry.

Of primary interest in this thesis are gas-liquid flows either as two-phase flow, e.g. air-water or air-oil, or as a three-phase flow, for instance air-oil-water flow which is very common for the oil industry.

The scope of this section is limited as it is intended as a brief introduction in the field. For further information, see recent textbooks about gas-liquid flows (Azzopardi 2006) and multiphase flow in general (Crowe 2006, Brennen 2005) as well as the tutorials Ghajar (2005) and Wörner (2003).

2.1.1 Flow patterns

In gas-liquid flows, since the interfaces are deformable, there are in principle an infinite number of ways in which the interfaces can be distributed within the flow. These distributions can be classified into a number of interfacial distributions, which is a considerable aid in developing models for two-phase flows. The types of interfacial distributions are termed flow patterns (or flow regimes). While a large variety of types of flow patterns have been defined in the literature, a small number of major patterns are widely accepted, as described below.

The parameters that govern the occurrence of a given flow pattern are numerous. Among them, the most important are flow rates of each phase, fluid properties of each phase, pipe geometry, pipe inclination, and flow direction (upward, downward, co-current, counter-current). The discussion of all these parameters is out of scope of this section. The most common cases involve horizontal flow and vertical up-flow where both phases are flowing upwards. Both cases will be considered here (Azzopardi 2006).

The major flow regimes found in vertical gas-liquid up-flow in a pipe of circular cross-section are illustrated in Figure 2.1a displayed from left to right in order of increasing gas flow rate at a given constant liquid flow rate.

- Bubbly flow: at low gas flow rates this is the predominant flow regime, where the gas flows as a myriad of bubbles in a continuous liquid phase.
- Slug flow: as the gas flow rate increases, collisions between bubbles are more frequent and they coalesce, eventually forming large bullet shaped bubbles,

often called Taylor bubbles. The liquid slugs between the Taylor bubbles often contain a dispersion of smaller bubbles.

- Churn flow: with further increase in gas flow rate, the Taylor bubbles in slug flow break down into an unstable pattern in which there is a churning or oscillatory motion of liquid in the tube. The gas now exists predominately as large irregularly shaped bubbles with smaller bubbles entrained in the liquid phase.
- Annular flow: when the gas flow rate is sufficiently large to support a liquid film at the surface of the pipe, the gas flows continuously through the center of the pipe. The liquid flows along the pipe wall as an annular film and can also be carried along the central gas core as small liquid droplets.

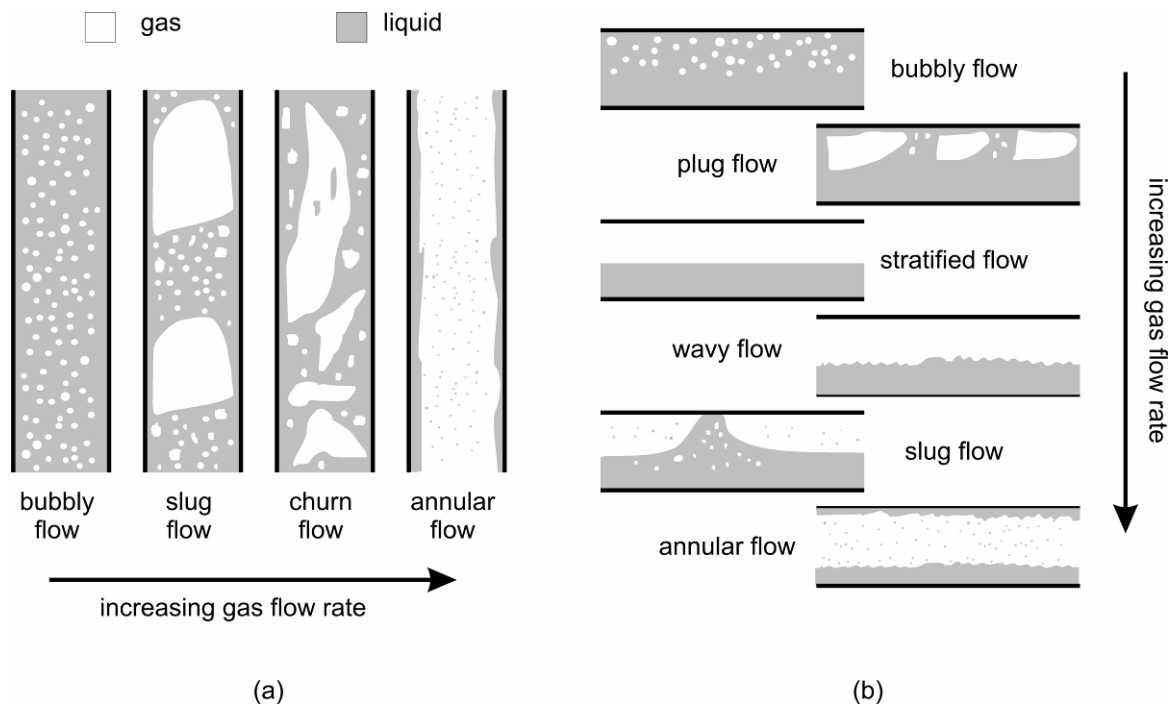


Figure 2.1: Flow regimes in (a) vertical gas-liquid up-flows and (b) horizontal gas-liquid flows.

Gas-liquid flow regimes in horizontal pipes are similar to the vertical flow regimes above, except the effect of gravity now tends to cause the gas to flow predominantly along the top of the pipe. The flow regimes are summarized in Figure 2.1b, from top to bottom in order of increasing gas flow rate.

- Bubbly flow: this, like the equivalent pattern in vertical flow, consists of gas bubbles flowing in a liquid continuum. However, gravity tends to make bubble accumulate in the upper part of the pipe, as illustrated.
- Plug flow: when the gas flow rate is increased, bubbles coalesce forming bullet shaped bubbles as also observed in vertical flow, but here they travel along the top of the pipe.
- Stratified flow: In this flow pattern the liquid flows in the lower part of the pipe the gas above with smooth interface. In real situations, the gas-liquid interface is rarely smooth, and ripples appear on the liquid surface.
- Wavy flow: it occurs as the ripples increase in amplitude generating waves due to the increase in gas flow rate.
- Slug flow: when the amplitude of the waves travelling along the liquid surface become sufficiently large that they touch the top of the pipe. The gas flows as bigger bubbles and in the liquid slugs many smaller bubbles may be entrained.
- Annular flow occurs when the gas flow rate is large enough to support a liquid film around the pipe walls. Liquid is also transported as droplets distributed throughout the continuous gas stream flowing along the center of the pipe. The liquid film is thicker along the bottom of the pipe because of the effect of gravity.

The determination of flow patterns still largely depends on visual observations, e.g. by means of a high-speed camera, but this is subjective and only possible for flows in transparent tubes. Thus, recently some analytical techniques have been made available by various types of instruments. Pressure transducers or void fraction sensors (either electrical impedance or radiation based techniques) allied with mathematical and statistical models are commonly used to analyze the signal fluctuation characteristics and thus to determine the flow pattern (Rouhani and Sohal 1983).

The regions over which the different types of flow can occur are conveniently shown on a flow pattern map in which a function of the gas flow rate is plotted against a function of the liquid flow rate and boundary lines are drawn to delineate the various regions. Transition curves on flow maps should be considered as transition zones analogous to that between laminar and turbulent conditions in single phase flows. For a more comprehensive and fundamental treatment of two-phase flow

transitions, refer to Barnea (1987). An example of a flow pattern map produced for a vertical up-flow in a round pipe is illustrated in Figure 2.2. The regime named dispersed bubbly is a sub-pattern classification of bubbly flow in which the bubbles are formed due to turbulent energy (Azzopardi 2006). Note that a map like this will only be valid for a specific pipe, particular pressure and a specific multiphase mixture.

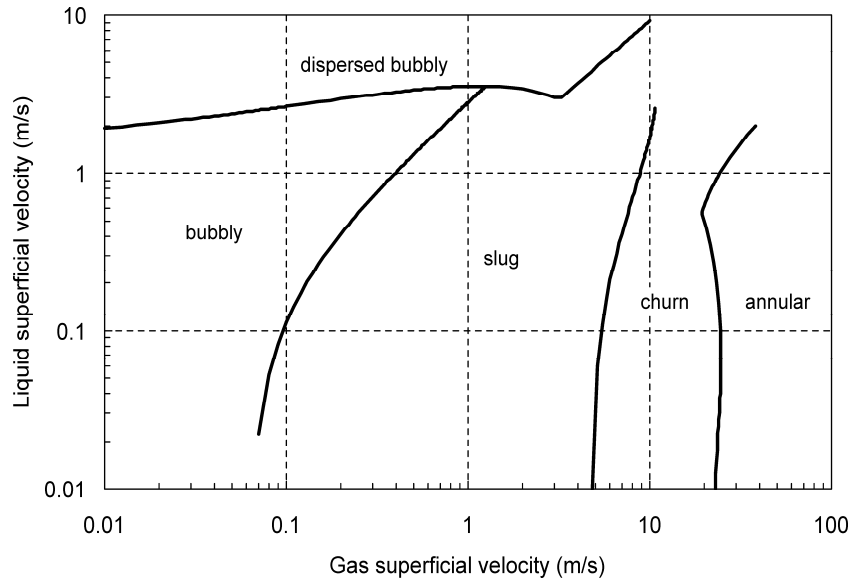


Figure 2.2: Flow pattern map for a vertical air-water up-flow in a round pipe of 67 mm diameter. Lines indicate the flow pattern transition model as described in Azzopardi *et al.* (2008). Liquid and gas superficial velocities are defined as volumetric flow rate divided by the cross sectional area of the pipe. These are the velocities which would occur if only one fluid (gas or liquid) was flowing alone in the pipe.

The various gas-liquid flow regimes discussed above still apply when the liquid is composed of two phases, as is the case in gas-oil-water three-phase flows; although the presence of different liquid phases may introduce extra complexity to the flow pattern depending on the degree of mixing of the components. In a well developed flow, oil and water may become separated and flow as distinct phases. On the other hand, the two liquid components may be well mixed or emulsified and the oil and water can often be considered as a single liquid phase in terms of flow regime and velocity. A recent discussion on three-phase flow patterns and their classification can be found by Keskin and Zhang (2007).

2.1.2 Modeling of multiphase flow

Multiphase flows are generally of complex nature due to the existence of multiple, deformable and moving interfaces, significant discontinuities of fluid properties and complicated flow fields near the interface. For instance, the flow conditions in a pipe vary along its length, over its cross section, and with time. A multiphase flow is an extremely complex three-dimensional transient problem. Furthermore, there are serious deficiencies in modeling of turbulence flows that occur in most practical cases (even for single phase flow). Thus, fundamental analytical predictions of multiphase flows are not readily achievable.

It may be possible at some distant time in the future to code the partial differential equations governing fluid flows given by the space- and time-dependent energy, mass, and momentum balances (known as Navier-Stokes equations) for each of the phases and to compute every detail of a multiphase flow. But the computer power and speed required to do this are far beyond capability for most of the flows that are commonly experienced. Therefore, simplifications are essential in realistic models of multiphase flows. The most common model used is the so-called two-fluid model (Hewitt 1999, Wörner 2003, Crowe 2006). It is based on the premise that is sufficient to describe each phase as a continuum occupying some part of the domain space (e.g. pipe). Here, effective conservation equations (of mass, momentum and energy) are developed for the two phases, including interaction terms between the phases. These equations are then solved either theoretically or computationally. By averaging terms in the equations over time, space, or other appropriate variables, the two-fluid model may be reduced to more manageable forms, such as the time-averaged one-dimensional model which is perhaps the most important and common method developed for analyzing two-phase pressure drop and heat transfer (Ghajar 2005). Other frequently used models are the homogeneous and drift-flux models (Hewitt 1999).

In recent years, the progressively increasing computer power has fostered the development and application of flow simulation codes, commonly known as computational fluid dynamics (CFD). A complete description of multiphase flow, specifying the phase present and its velocity at each point in the flow and for a given simulation time, is the approach used in CFD. Of course, space and time variables are discretized in order to be numerically solved. Furthermore, the use of some model (e.g. turbulence models) is required to reduce the computational power necessary to predict the flow phenomena. A number of commercial CFD software packages are

currently available, for instance CFX (Ansys 2008), Fluent (Fluent 2008), OpenFoam (OpenCFD 2008), and have successfully been applied for single phase flow problems. CFD codes are becoming powerful tools in the hand of engineers who design plants and have to predict flow-related safety and efficiency issues. Moreover, the use of CFD simulations of multiphase flow is still in an early stage of development. Although some workers have produced successful solutions to engineering multiphase flow problems, the ultimate accuracy and the general applicability of CFD simulations depend intrinsically on the empirical relationships and simplifications used in codes to model multiphase flow. As a result, CFD code validation has more and more risen to a key issue equally important to code development. It is obvious that successful code validation is a main quality criterion for CFD codes and only sufficiently validated code can be admitted to safety-related predictions, for instance in nuclear reactor safety. CFD code validation requires small and medium scale multiphase flow experiments with accurate, multi-dimensional and non- or minimal intrusive measurement techniques for different physical parameters, such as phase fraction distributions, temperature fields, pressure fields, velocity fields, and concentration fields. Also therefore, multiphase flow measurement techniques have got a strong impulse in recent years.

2.2 State-of-the-art multiphase flow measuring techniques

Online visualization and quantitative parameter assessment of multiphase flows are highly desirable in many research and industrial application areas, for instance as control and monitoring aid of industrial processes or as source of data for the validation of models and simulations. Because of this high interest many efforts have been made to develop measuring techniques to measure and image multiphase flows.

In addition to the already known problems encountered in any measuring method for single phase flows - amply described, for instance, in Baker (2000), further difficulties appear when attempting to measure quantities in multiphase mixtures. One of these difficulties is related to the presence of two or more phases which of course leads to the need for differentiation between the phases. For transient flow, such differentiation must occur at high temporal resolution due to the unsteady nature of the flow, i.e. a high data acquisition rate is required. Others difficulties arrive from the conditions of flow confinement, such as opaque metallic walls, or complex test section geometries. Such constraints may limit the use of some measuring

principles. Moreover, the robustness of sensors is an import issue for some industrial applications where harsh environmental conditions occur, i.e. high pressure, high temperature and/or the presence of aggressive media.

Despite these difficulties, advances in instrumentation technology and signal processing techniques have led to a rapid proliferation of available experimental methods for measurement of practical or fundamental parameters in multiphase flows with a fair degree of accuracy. The purpose of this section is to present the principles of a few state-of-the-art measuring techniques mainly focused on void fraction and phase distribution measurement in gas-liquid flows. Good reviews in this field are given by Boyer *et al.* (2002), Bertola (2003) and Hammer *et al.* (2006).

For reviews covering a broader spectrum following references are indicated.

- An overview on multiphase flow measurement in general can be gained from the review Oddie *et al.* (2004).
- For further details of measurement techniques specifically intended for
 - gas-solid flow, see Werther (1999),
 - for liquid-solid (or slurry) flow, see Mishra *et al.* (1997), and
 - for liquid-liquid flow, see Jana *et al.* (2007).
- Furthermore, two review papers have mainly focused on the discussion of experimental techniques for CFD validations (Tayebi *et al.* 2001, Prasser 2008).

2.2.1 Phase fraction measurement

The phase fraction for gas-liquid flows is commonly known as the void fraction for the gas phase and the liquid hold-up for the liquid phase. Both quantities are interchangeable with help of the continuity equation which requires the sum of gaseous and liquid phase fraction to equal unity. Thus, in the following the term void fraction will be preferably used to indicate the phase fraction.

Void fraction is a dimensionless quantity indicating the fraction of a geometric or temporal domain occupied by the gaseous phase. It is one of the most import parameters used to characterize multiphase flows. It is the key physical value for determining numerous other important parameters, such as mixture density and viscosity, for obtaining the relative averaged velocity of the phases, and is of

fundamental importance in models for predicting flow pattern transitions, heat transfer and pressure drop (Azzopardi 2006, Crowe 2006).

Phase fractions may be mathematically described by the introduction of a phase indicator (or density) function P_k which is a binary function and represents the presence or absence of phase k at a given position \mathbf{x} and given time t , hence

$$P_k(\mathbf{x}, t) = \begin{cases} 1 & \text{if } \mathbf{x} \in \text{phase } k \\ 0 & \text{if } \mathbf{x} \notin \text{phase } k \end{cases} \quad (2.1)$$

By averaging the gas indicator function P_G over different spatial or temporal domains one can obtain different definitions for the void fraction, e.g. local, radial, cross-sectional and volumetric (Delhay *et al.* 1981, Bertola 2003).

Void fraction measurement techniques are based on various principles. Usually, instruments are sensitive to some physical property which is different for each phase, such as density or electrical conductivity. In this section, measuring techniques for local and cross-sectional measurements are depicted. In addition, a brief introduction to the challenging field of three-phase flow metering in the oil industry is given.

a) Local measurement

Local void fraction is typically measured using a miniature needle-shaped probe, which determines the actual phase present at the probe tip. Needle probes are designed to pierce bubbles and droplets. In this way, they determine the phase indicator function (2.1) at a given point \mathbf{x} . From the measured gas indicator function P_G , the local time-averaged void fraction is defined as

$$\alpha(\mathbf{x}) = \lim_{T \rightarrow \infty} \frac{1}{T} \int_T P_G(\mathbf{x}, t) dt. \quad (2.2)$$

For a sufficiently long measurement time T (2.2) can be approximated by

$$\alpha(\mathbf{x}) = \frac{T_G}{T} = \frac{T_G}{T_G + T_L}, \quad (2.3)$$

where T_G and T_L denote the cumulated residence-time of the gas and liquid phases within the time interval T . By moving the probe in different positions, a mapping of the void fraction distribution in a given area or volume can be achieved, though it is sometimes a cumbersome practice.

Different measuring principles based on conductance, capacitance, optical, temperature or electrochemical measurements have been applied to the differentiation of phases. Excellent reviews are found in Cartellier and Achard (1990) and Jones and Delhay (1976). However, the most common are electrical and optical needle probes.

In the case of optical probes, a light beam is guided along the probe, usually by means of an optical fiber, to its tip. Depending on the phase present at probe tip, the light is transmitted through the medium or reflected back. A photodetector at the other end of the fiber converts the intensity of the reflected light into a voltage signal thus being an indicator for the phase.

Electrical probes use either direct current or alternating current excitation and the probe acts basically as a switch. Figure 2.3a illustrates an example of an electrical probe design. When the phase at the probe tip is electrically conducting, a current flows from the inner excitation electrode to the grounded external electrode. If the phase at probe tip is non-conducting the circuit is open and there is no current circulation. Usually, the current is converted into a proportional voltage which again is an indication of the phase present at probe tip. Typical probe signals obtained with a conductivity probe are shown in Figure 2.3b. Although the probe signal should be theoretically rectangular, the probe response is not exactly square because of the finite size of the tip, the wetting/dewetting time of interface covering the tip, and the response time of the probe and electronics. Therefore, the acquired signal is binarized by an appropriate trigger level (Jones and Delhay 1976).

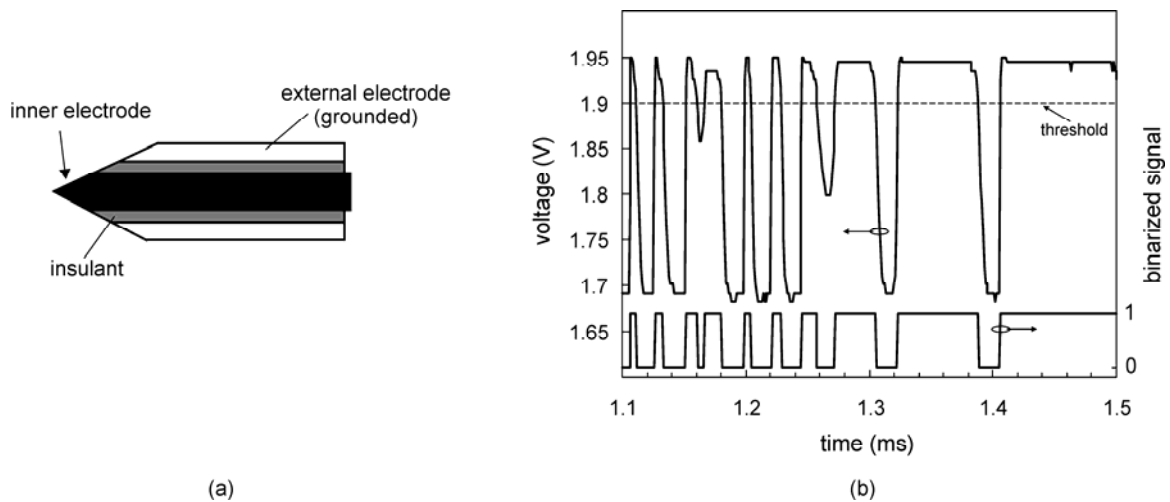


Figure 2.3: Conductivity needle probe design (Chanson 2002). (a) Lateral cut, (b) typical voltage signal obtained in a bubbly flow as well as the corresponding binarized signal by an exemplary threshold. Data were obtained by an advanced needle probe described by Schleicher *et al.* (2008a).

Choosing the one or other physical principle behind the needle probe measurements is of course a matter of the type of substances to be investigated. For instance, the first requirement to be met when using conductivity or optical probe in two-phase flow is that one phase has a significantly different electrical conductivity or refraction index, respectively.

Needle probes are used as single-tip or double-tip designs, depending on the kind of data expected: single-tip probes lead to gas fraction, and bubbling frequency; double-tip probes allow measurements of bubble velocity, mean bubble chord length and time-average local interfacial area (Cartellier and Achard 1990).

Some researchers proposed multiple point probes, for instance a four tip probe (Kim and Ishii 2001). Such probes can determine other components of dispersed phase velocity regardless of bubble shape, diameter and direction. However, the probes rapidly become bulky and so hydrodynamic interaction between bubbles and the probe can no longer be neglected. In addition, the data analysis to extract physical quantities is much more complex than for single-tips probes.

b) Cross-sectional measurement

The cross-sectional averaged void fraction α_{c-s} yields from averaging the phase indicator function (2.1) over the cross-sectional area A of a pipe or vessel at a given time

$$\alpha_{c-s}(t) = \frac{1}{A} \int_A P_G(\mathbf{x}, t) da = \frac{A_G}{A_G + A_L}, \quad (2.4)$$

where A_G and A_L denote the cumulated cross-sectional areas occupied by the gas and liquid phases, respectively, within the cross section considered. It is typically measured by means of radiation attenuation or electrical impedance techniques which are described below.

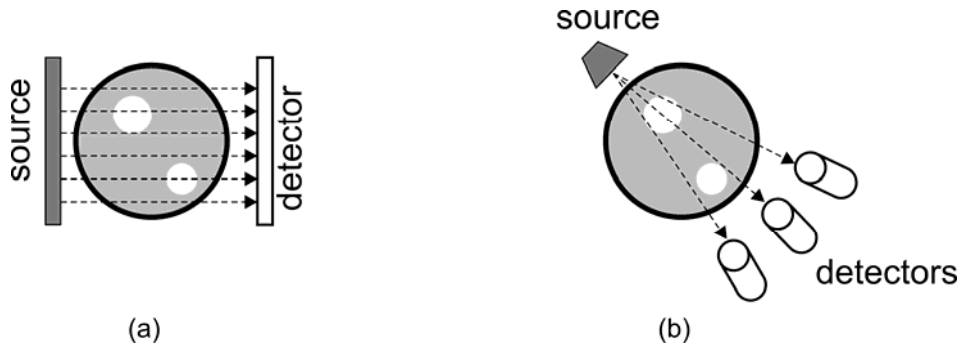


Figure 2.4: Two schemas for the measurement of cross-sectional void fraction by radiation attenuation techniques. (a) One-shot technique, (b) multibeam densitometer.

Usually setup of radiation attenuation techniques consist of a radioactive source (commonly γ -ray or x-ray but also neutrons) and a radiation detector, placed so that the beam passes through the flow and is monitored on the opposite side of the multiphase mixture (Figure 2.4). For a homogeneous medium the radiation attenuation of a collimated, mono-energetic beam follows the exponential law

$$I = I_0 \exp(-\mu d), \quad (2.5)$$

where I_0 is the intensity of incident radiation, I is the intensity of transmitted radiation, μ is the absorption coefficient of medium and d is the distance the beam travels through the medium. For the measurement of cross-sectional void fraction the narrow beam must be replaced by a linear source (a radiation sheet, Figure 2.4). This is called one-shot technique. However, for this configuration the simple relationship (2.5) does not hold, because absorption depends on both flow pattern and pipe geometry, so that calibration measurements with mockup setups that simulate the different flow regimes and void fractions are necessary. Another way to obtain α_{c-s} is to employ a multibeam densitometer. An exemplary setup with only three beams is shown in Figure 2.4. The beams are attenuated according to (2.5) and the measurement of the attenuation of each beam can be used to determine the cross-sectional void fraction by the numerical integration (Delhaye *et al.* 1981).

Typical commonly used radioactive sources of gamma radiation include isotopes of americium, cesium or cobalt. Radiation is generally detected by means of a scintillator coupled to a photodetector. The scintillator absorbs radiation and emits visible light by fluorescence (Johansen 2005).

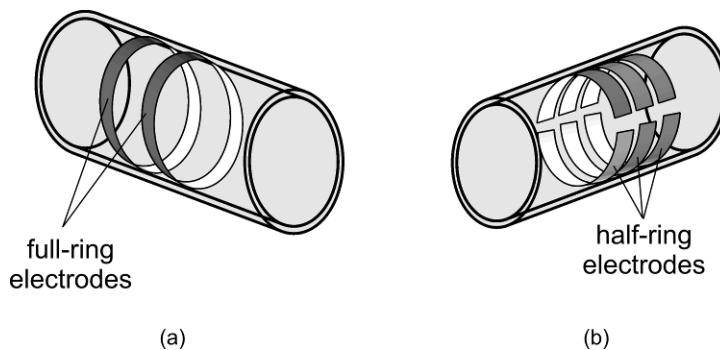


Figure 2.5: Configuration of electrodes for electrical conductivity probes: (a) two full rings, (b) half rings.

The electrical impedance technique, also known as impedance probe, is based on the fact that the liquid and gas phases have different electrical conductivities and/or

relative permittivities. Impedance probes offer high frequency response, low cost, and relative ease of construction.

By placing electrodes at the perimeter of a pipe and measuring the impedance across the electrodes, the void fraction of the pipe may be deduced. As shown by Ceccio and George (1996) in their extensive review analysis on impedance techniques, there are many different possibilities to arrange a system of electrodes for void fraction measurement purposes. Furthermore, the impedance technique has been almost exclusively implemented in two categories depending on the type of instrumentation used and liquid material to be investigated: electrical conductivity and capacitance probes.

With reference to the conductivity probes, flush-mounted ring electrodes were successfully employed first by Asali *et al.* (1985), and then by Andreussi *et al.* (1988), Tsochatzidis *et al.* (1992), Fossa (1998), among others. A typical arrangement is represented by two metallic rings annealed in the pipe inner wall, as shown in Figure 2.5a. Ma *et al.* (1991) and later Costigan and Whalley (1997) developed a probe with other electrode configuration which has been also successfully employed for the investigation of two-phase flows. It is constituted by a pair of measuring half-rings facing one another with two guard electrodes (again half-rings) maintained at the potential of the corresponding measuring electrodes (Figure 2.5b).

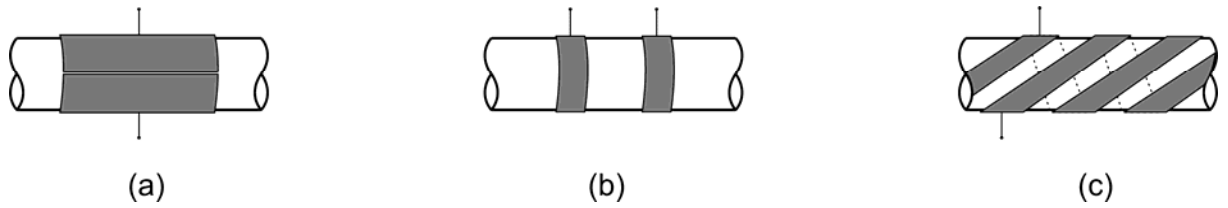


Figure 2.6: Configuration of electrodes for capacitance probes: (a) concave plates, (b) double ring, (c) helical.

Capacitance probes may be applied to two-phase flow problems where the liquid is a non-conducting material such as oil, for instance. Furthermore, such probes provide the possibility of a fully non-intrusive way to measure void fractions. In fact, unlike conductive probes, the electrodes do not need to be in contact with the fluids (Stott *et al.* 1985). As for conductivity probes, there are many possibilities for assembling the electrodes of a capacitance-based measurement system (Sami *et al.* 1980). The most common arrangements are: helical sensor (Geraets and Borst 1988), concave plate sensor (Elkow and Rezkallah 1996) and ring type sensor (Ahmed 2006). These

electrode configurations are depicted in Figure 2.6. It is common that the capacitance of those setups is in the range of 0.1 to 10 pF. Thus, proper shielding against stray capacitance and a good signal-to-noise ratio are extremely important for a correct void fraction measurement. Articles by Huang *et al.* (1988, 1989) have reviewed electrode guard methods and capacitance measurement techniques.

Combination of conductive and capacitive measurements has been also reported in the literature, but this practice is less common. The measurement of the complex value of impedance was described for three component fraction measurement (Dykesteen *et al.* 1985) and for water content measurement in oil-water emulsions (García-Golding *et al.* 1995).

c) Multiphase flow metering in the oil industry

Three-phase gas-oil-water flows are common in the oil industry. Most of the gas and oil reservoirs naturally contain water or due to the pressure decrease with production, the natural pressure of an oil reservoir is maintained by injecting water. Therefore, water is produced along with oil and gas which results in a three-phase gas-oil-water flow in wellbore and surface gathering systems. Three-phase flows thus occur in the wells, in the flow lines connecting the wells to the platform and in the risers conducting the fluid from the flow lines to the top of the platform (Hewitt 2005).

Under the multiphase flow circumstances, the following parameters are required to compute flow rates of each phase: (i) the cross-sectional phase fraction and (ii) the axial velocity of each phase. The volumetric flow rate Q_x of a given phase x is determined by the product of phase velocity U_x and area of the pipe occupied by the respective phase A_x

$$Q_x = A_x \cdot U_x \quad (2.6)$$

Since A_x may be calculated from the phase fraction $A_x = A \cdot \alpha_x$, where A is the pipe area, basically six variables must be estimated in the general multiphase measurement problem, i.e. three phase fractions and three phase velocities (Letton *et al.* 1997):

$$Q_T = Q_O + Q_G + Q_W = A(\alpha_O \cdot U_O + \alpha_G \cdot U_G + \alpha_W \cdot U_W), \quad (2.7)$$

where the subscripts O, G, and W denote oil, gas and water phases in a three-phase flow, respectively.

In this way, making measurements in such three-phase flows presents special difficulties. A distinction needs to be made between the gas and liquid phases, and also between the primary and secondary liquid components. Basically two strategies have been used in multiphase flow meters in the gas and oil industry: phase separation meters or in-line meters. For a review in that field, Corneliussen *et al.* (2005), and the review in Baker (2000, chapter 14) are indicated.

Phase separation meters, as the name already suggests, are characterized by the fact that the phases are separated before measurement. The three phases are then measured individually using some single-phase measuring technique. With the space on a production platform becoming more expensive, and the development of subsea production systems increasing, the use of conventional offshore separators is becoming less desirable. Therefore, the growth in research and development of in-line multiphase flow metering systems has been exponential since the early 1980s (Falcone *et al.* 2002).

Today there is a variety of in-line multiphase flow meters installed onshore and offshore and other being developed which use different sensing techniques and models to calculate multiphase flow rates via (2.7). For the measurement of phase fractions, current systems are based on dual energy gamma ray method or the combination of two of the following techniques: mono-energetic gamma ray absorption, resistance/capacitance measurements or microwave sensors (Babelli 2002, Falcone *et al.* 2002, Yeung 2007). Recently, a dual energy x-ray tomograph has been presented by Hu *et al.* (2005) for time-resolved phase fraction distribution measurement which has been used only for research purposes yet. Phase velocities are usually measured by cross-correlation techniques from signals of two axially spaced sensors. With an alternative approach, some other flow meters firstly homogenize the flow assuring all phases are well-mixed and the assumption that all three phases flow with equal velocity ($U_o = U_g = U_w = U$) may be applied. The mixture velocity is then determined by a conventional venturi meter or a positive displacement meter.

Varying level of accuracy requirements exists in multiphase flow measurement depending on how the information will be utilized, for instance, for fiscal or monitoring purposes. Although many alternative metering systems have been developed and tested, none can be referred to as universally accurate and/or applicable. The market potential is huge. Yeung (2007) estimates that only 0.2% of current oil wells are instrumented with multiphase flow meters. Thus, there are many

opportunities; and the search for new technologies and innovative solutions for this challenging field still persists.

2.2.2 Tomographic flow imaging

Tomographic multiphase flow imaging, more commonly called process tomography or industrial process tomography, finds many applications in the imaging and measurement of industrial processes. A tomographic image is a two-dimensional representation of a slice through an object. The use of various tomographic methods is widespread in diagnostic medicine (Kak and Slaney 1988) and several imaging modalities originally developed for medical imaging are now being adapted to industrial process imaging. The use of tomographic imaging for the investigation of multiphase flows has been reported in a few exhaustive review papers (Dyakowski 1996, Chaouki *et al.* 1997, Williams and Jia 2003, Prasser 2008) and books (Williams and Beck 1995, McCann and Scott 2005).

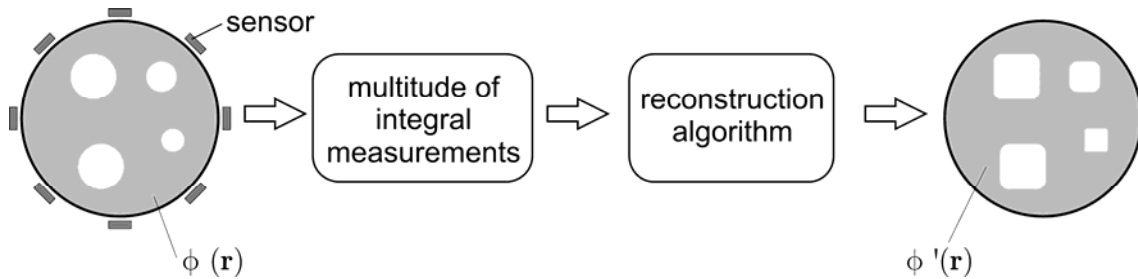


Figure 2.7: Principle of process tomography. Different types of measurement are described in text.

The general principle of computed tomography (CT) for multiphase flow consists of measuring a physical property through the pipe or vessel that can be related to the phase fraction (e.g. electrical impedance, attenuation coefficient). A number of integral, independent measurements are taken from sensors (or electrodes) placed on the periphery of the test object at different angular positions either by rotation of arrangements or electronic switching. After measurements have been completed, the local properties of the flow can be calculated by means of a so-called reconstruction algorithm. Evidently, the reconstructed image $\phi'(\mathbf{r})$ may not be always identical with the real distribution $\phi(\mathbf{r})$. Figure 2.7 illustrates schematically this process. The

image reconstruction in tomography implies solving an inverse problem, i.e. obtaining the spatial distribution of the imaged parameter from a plurality of measurements and the known geometry of the problem. A conventional computer is often used for off-line image reconstruction. However, for real-time reconstruction parallel computing systems may be applied. There are many types of tomography systems based on different sensing techniques such as electrical, ultrasound, radiation. A short description of current most common tomographic technique for multiphase flow measurement is given in the following.

a) X-ray, γ -ray and neutron tomography

X-ray, γ -ray and neutron tomography can be seen as an evolution of the densitometry method for cross-sectional void fraction measurement as described in section 2.2.1b). These modalities are based on the attenuation of radiation by matter. Since gas and liquid present different attenuation characteristics for the radiation, images of void fraction distributions may be obtained. The set of projections needed for the reconstruction of the images are generated either by rotating source and detectors around the pipe or by the use of multiple source and detectors (Johansen 2005). The use of x-ray tomography for void fraction measurements was described, for instance, by Hervieu *et al.* 2002 and Heindel *et al.* (2008), while use of gamma ray tomography was reported by Kumar *et al.* (1995), Hampel *et al.* (2007), among others. All the above-mentioned techniques yield time-averaged rather than instantaneous phase distribution images due to the use of mechanically rotating parts. The time resolution of such systems is limited to a few images per second. Attempts to increase time resolution have been reported by Johansen *et al.* (1996) who describe a γ -ray tomography system operated by five gamma sources in parallel capable to generate 100 fps, by Hori *et al.* (1998) who introduced a multitube x-ray scanner which achieve 2 000 fps and recently by Bieberle *et al.* (2007) who used an electron beam to generate a fast moving x-ray spot and reached 10 000 fps. These approaches allow the study of dynamically changing phase distributions. However, such solutions are still comparatively complex and cost-intensive.

Neutrons have some advantages in terms of their attenuation in matter in comparison to photons. For example, organic materials or water are clearly visible in neutron radiographs because of their high hydrogen content, while many structural materials such as aluminium or steel are nearly transparent. Nevertheless, neutron

tomography requires complex, expensive and heavy equipment for the generation of neutrons, and therefore its use for the investigation of multiphase flows has been limited in the past (Hussein *et al.* 1986).

b) Magnetic resonant imaging

Magnetic resonant imaging (MRI) is widely used in medical diagnostics, which is based on the paramagnetic properties of the nuclei. MRI scanners use the phenomenon of nuclear magnetic resonance of hydrogen nuclei in conjunction with radio frequency (rf) and magnetic gradient pulses to map the object under investigation (Mantle and Sederman 2003). Basically, MRI detects the concentration of hydrogen atoms, thus liquid water presents excellent contrast. MRI is able not only to determine the density of nuclei but also the velocity in case of moving objects. Mantle and Sederman (2003) and Hall (2005) reported some flow applications of MRI in their reviews. Some limitations of MRI are the necessity of non-magnetic, non-conducting pipes to allow the measurements, the rather low imaging frequency and the relatively high hardware cost. A special MRI technique called Echo-planar Imaging can achieve up to 140 frame per second and it was used to investigate slug flow (Reyes Jr. *et al.* 1998). However, this technique needs even more costly hardware than conventional MRI to achieve such a frame rate.

c) Positron emission tomography

Positron emission tomography (PET) is based on the use of a γ -ray emitting radioisotope as a flow tracer. External detectors are used to measure the number of rays emerging from the system which provides the information needed to reconstruct the tracer distribution by the standard tomographic approach. In a multiphase flow, one of the phases can be labeled and its behavior analyzed (Parker and McNeil 1996). However, the acquisition time of a PET system lies in the order of minutes and is thus too slow for rapidly evolving flows. An alternative method is the positron emission particle tracking (PEPT) which involves introducing a single labeled tracer particle in the process which has its trajectory tracked by using advanced algorithms (Parker *et al.* 1993). The overall system time response is in the range of milliseconds and a particle moving at speeds about 1 m/s was reliably followed.

d) Optical tomography

Optical tomography uses low energy electromagnetic radiation, either of the infrared, visible or ultraviolet wavelength range, to measure extinction profiles from an object and subsequently reconstruct the data by means of CT algorithms. A few researchers have reported on optical tomography for the investigation of single phase and multiphase flows (Rzasa and Plaskowski 2003, Ruzairi and Chan 2004, Schleicher *et al.* 2008b). The common characteristic of these systems is the use of low-cost light emitters and detectors. Another example of optical tomography applied to process investigation is described by Carey *et al.* (2000) and Hindle *et al.* (2001), who performed chemical species imaging by exploiting specific substance absorption at near-infrared band. Optical tomographs may reach very high temporal resolution of a few thousand frames/s. Nevertheless, regarding gas-liquid flows, optical systems can only be successfully employed to flows with low void fraction (typically up to 10%) due to the fact that the flow becomes opaque for light at high voidage. Optical systems also need transparent walls and transparent liquids to be able to investigate the flow.

e) Ultrasound tomography

Tomography based on ultrasonic waves has also been applied to investigate multiphase flows (Hoyle 1996). An ultrasonic system detects changes in the acoustic impedance properties between objects. Gas-liquid flow exhibits a marked acoustic impedance difference between gas and liquid interfaces. In ultrasound tomography multiple ultrasonic transducers are mounted around the pipe. Basically, reflection mode (Yang M. *et al.* 1999) and transmission mode (Rahiman *et al.* 2006, Supardan *et al.* 2007) measurements can be applied, in which the reflected or transmitted ultrasonic waves are evaluated, respectively, along with suitable reconstruction procedure. Frame rates obtained are in the range of a few hundred images per second. One advantage of ultrasound tomography is the possibility to image flows inside opaque objects. However, the limitation regarding low void fractions is similar as for optical systems.

f) Electrical tomography

An important field in process tomography is the one concerned with electrical impedance tomography (EIT) which exploits the interaction of electrical fields with matter. The main task of EIT is to determine conductivity or permittivity

distributions which are linked to phase distributions in a multiphase flow. Thus, EIT is also referred to electrical resistance tomography (ERT) or electrical capacitance tomography (ECT) depending on the modality. Some researchers have erroneously used the term EIT as synonym to ERT. However EIT should be used only when both resistance and capacitance are measured (called dual-modality), as described by Marashdeh *et al.* (2007) and Cao *et al.* (2007).

In EIT a number of electrodes are arranged equally spaced around a pipe or vessel to be interrogated. For ECT systems, the electrodes are normally non-invasive, lying outside the wall, as well as non-intrusive, touching but not penetrating the wall. For resistance and impedance measurements the electrodes are usually invasive but not intrusive. Figure 2.8 shows typical configurations. An image is obtained by applying electrical fields and measuring the resulting sensor responses. The full set of data is obtained by successive activation of every electrode while the responses of all remaining electrodes are measured. In ECT the excitation signals are generated by applying voltages and also voltages are measured, while in ERT currents are injected and voltages are measured. The choice for one or other modality mainly depends on the target of interest. ERT has been used to image concentration distributions in saline, gas-liquid mixtures, and slurries, among others applications. Since ECT is suitable for the investigation of non-conducting materials, it has been applied to oil-gas two-phase flow, bubble columns, fluidized bed, etc. For more extensive reviews of the electrical modalities, see Xie *et al.* (1995), Dyakowski *et al.* (2000), York (2001), Tapp *et al.* (2003) and Yang and Peng (2003).

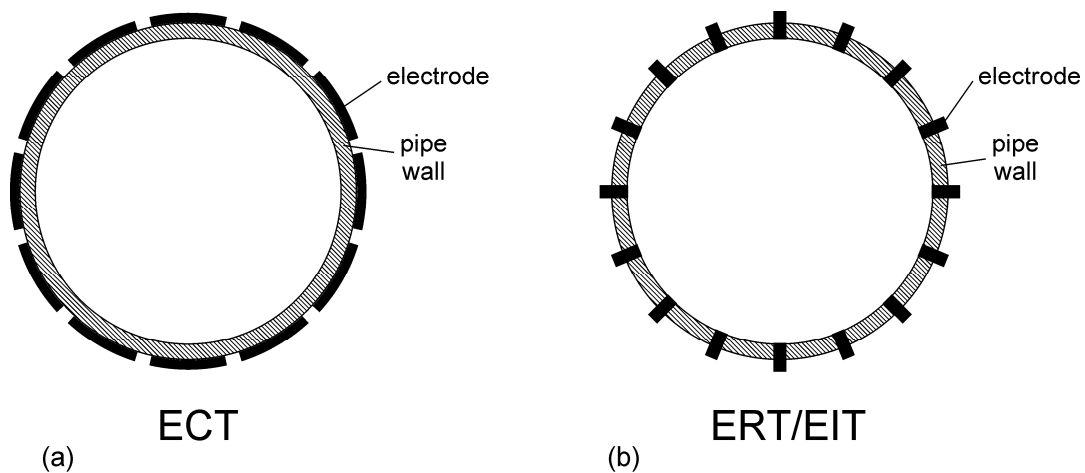


Figure 2.8: Typical electrodes arrangement in electrical tomography systems: (a) 12 electrodes ECT system and (b) 16 electrodes ERT/EIT system.

EIT systems are relatively fast (up to 1 000 images per second), low cost and simple to operate. The main disadvantage of EIT is its moderate spatial resolution of the resultant image. The measured electrical signals are a non-linear function of phase fractions and flow configuration and unlike x-ray or γ -rays, electrical fields cannot be confined to a narrow path between a transmitter and receiver. This is called the soft-field property of electrical tomography.

A third electrical modality, electromagnetic tomography (EMT) or magnetic inductance tomography has been reported which is based on mutual inductance measurements. EMT is suitable for imaging highly conducting or magnetic materials, such as metals and minerals (Peyton *et al.* 1996).

2.2.3 Wire-mesh sensor

Wire-mesh sensors are flow imaging devices and allow the investigation of multiphase flows with high spatial and temporal resolution. Although they could not be considered belonging to classical tomographic technique, because their working principle is based on intrusive electrodes to generate the images, it has been accepted as an alternative technique to the tomography systems previously described. This type of sensor was introduced about ten years ago by Prasser *et al.* (1998) at FZD and since then it has been successfully employed by a number of researchers to investigate different single phase and two-phase flow phenomena. An overview over the capabilities of wire-mesh sensors was recently summarized by Prasser (2008).

The sensor is a hybrid solution in between intrusive local measurement of phase fraction and tomographic cross-sectional imaging. The sensor comprises of two sets of wires stretched over the cross-section of a vessel or pipe with a small axial separation between them. Each plane of parallel wires is positioned perpendicular to each other, thus forming a grid of electrodes (Figure 2.9). The associated electronics measures the local conductivity in the gaps of all crossing points at high repetition rate. Considering a two-phase flow consisted of an electrically conducting phase and another one non-conducting, for instance air and water, the obtained conductivity measurements are an indication of the phase present at each crossing point. Hence, the sensor is able to determine instantaneous void fraction distributions over the pipe cross section.

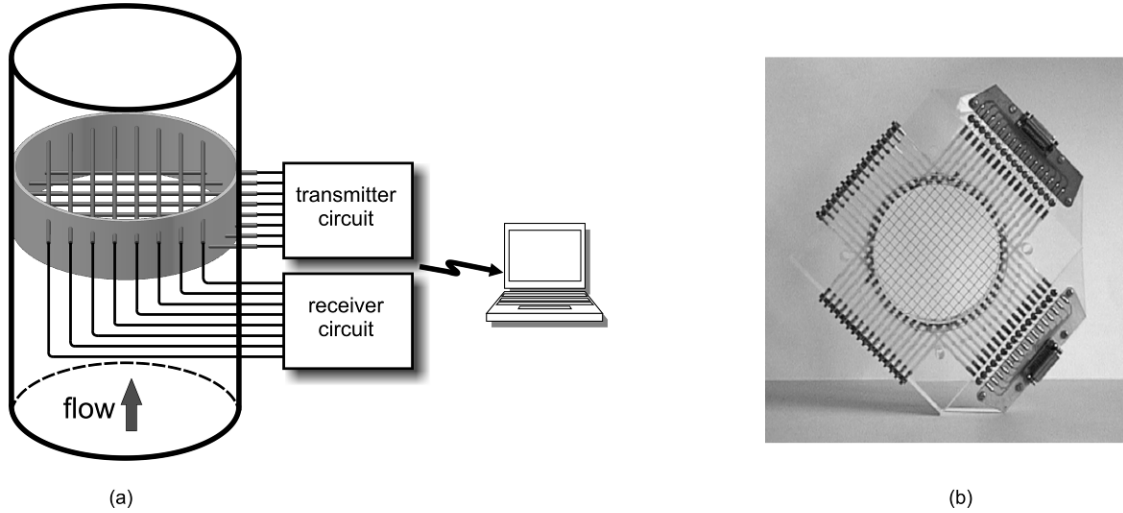


Figure 2.9: (a) schematic representation of a wire-mesh sensor; (b) photograph of a typical sensor developed at FZD.

Regarding the measuring principle, a multiplexed excitation-measuring scheme is applied, as described below. The wires of the one plane are used as transmitters and the wires of the other plane as receivers. Figure 2.10 shows the block diagram of the electronics of a conductivity wire-mesh sensor for an exemplary 4×4 sensor configuration. The transmitter wires are activated by supplying them with bipolar voltage pulses in a successive order by switches the S1–S4. The non-activated electrodes are connected to ground potential. The current at a receiver wire resulting from the activation of a given transmitter wire is a measure of the conductivity of the fluid in the corresponding control volume close to the crossing point of the two wires. The currents from all receiver wires are sampled simultaneously. This procedure is repeated for all transmitter electrodes. After activating the last transmitter wire, a complete set of measurements for the whole cross-section has been acquired. The measurements are in fact voltages which are proportional to the conductivity of the medium around each crossing point of the wire grid at the very moment of data sampling. In this manner, the wire mesh subdivides the flow channel cross section into a number of independent sub-regions, where each crossing point represents one sub-region. Each of the measured signals reflects the constitution of the flow within its associated sub-region, i.e. each crossing point acts as local phase indicator. Hence, the set of data obtained from the sensor directly represents the phase distribution over the cross-section and no reconstruction procedure, e.g. by solving an inverse problem, is needed in order to determine cross-sectional phase distributions.

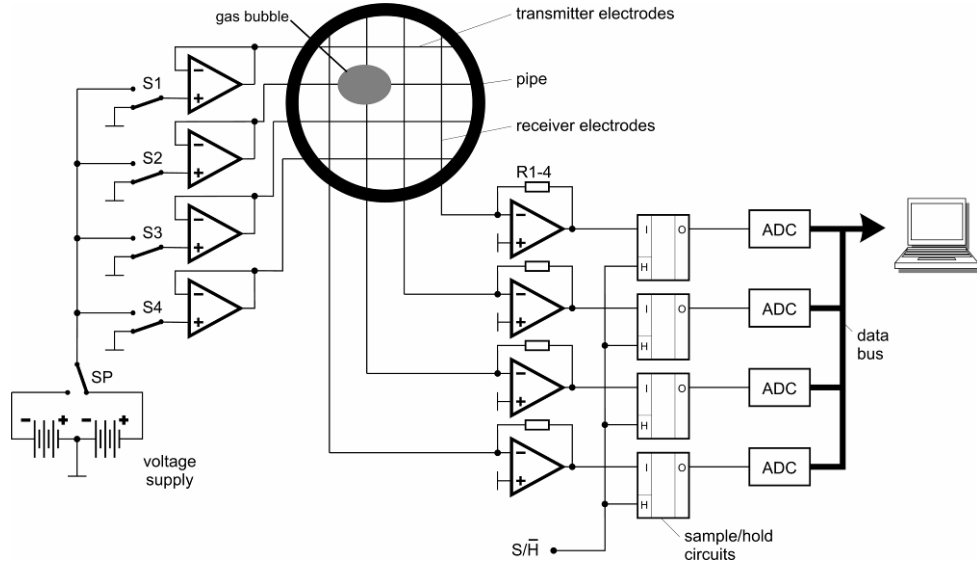


Figure 2.10: Wire-mesh sensor electronics with a 4×4 sensor configuration (Prasser *et al.* 1998).

From the first publication (Prasser *et al.* 1998) the technology of wire-mesh sensors has steadily been developed towards increasing frame rate (Prasser *et al.* 2002b), bubble size measurement (Prasser *et al.* 2001), gas phase velocity measurement (Manera *et al.* 2006), measurement at elevated pressures (Pietruske and Prasser 2007). In the scope of research work wire mesh sensors have extensively been used in the following fields: steam-water pipe flow (Prasser *et al.* 2007), mixing scenarios in pressurized water reactor models (Prasser *et al.* 2003), water hammers in pipes (Dudlik *et al.* 2002), and transient boiling (Manera *et al.* 2006). Today sensors can be devised with up to 64×64 wires, wire diameters down to 0.05 mm, in diversity of different cross-section geometries and operating parameters. High-pressure wire-mesh sensors can be employed for temperatures and pressures up to 286 °C and 7 MPa, respectively (Pietruske and Prasser 2007). Associated electronics for signal generation and data acquisition achieves a maximum temporal resolution of 10 000 frames per second (Prasser *et al.* 2002b).

The intrusiveness effect of wire-mesh sensors has been investigated by high-speed camera measurements (Prasser *et al.* 2001, Wangjiraniran *et al.* 2003) and by comparison with a fast x-ray tomography system (Prasser *et al.* 2005b). The results have shown that the sensor yields images of an undisturbed flow. Influences of the mesh are found only downstream from the sensor. In this way, wire-mesh sensors offer a compromise. The disadvantage of being intrusive is in part compensated by high temporal resolution, low cost, and simplicity when compared with other imaging systems.

Another wire-mesh device was also introduced by Reinecke *et al.* (1996, 1998). However, this device employs three set of wires forming an angle of 120° whereby the conductance of each parallel wire pair is measured. In this way, three independent projections of the flow cross section are obtained. The conductivity distribution is interpreted as the void fraction distribution. The transformation from the measured conductance data into the image has to be performed by applying a tomographic image reconstruction algorithm. This is the main difference to the above described sensor (which performs direct flow imaging) and also is the main disadvantage of this solution. The system of equations to be solved for the image reconstruction is highly underdetermined and must be iteratively resolved which cannot be assumed free of artifacts and is very time consuming.

2.2.4 Other techniques

Gas-liquid flows have been also investigated by a variety of other measuring techniques different to those discussed above. Some examples are optical and velocimetry methods.

Optical visualization is probably the first diagnostic tool chosen when multiphase flows are investigated. High-speed cameras are easy to operate and typically reach frame rates of tens of kilohertz. Thus, by proper image processing algorithms, optical visualization techniques are useful to investigate the form and behavior of bubbles (e.g. shape, size, velocity), as well as phase boundaries in gas-liquid flows. It has been very frequently reported in the literature (e.g. Lage and Esposito 1999, Zaruba *et al.* 2005). The limitations of optical techniques are obvious: only the vicinity of the wall can be observed at high void fraction and transparent walls as well as a transparent liquid are required.

Another classical optical technique for flow studies is the particle image velocimetry (PIV). It is used for measuring the instantaneous flow velocity. Images of small tracers freely flowing in the fluid under study are acquired at two or more times by pulsing some light source (Adrian 1991). The motion of these tracers is then a measure of the motion of the fluid, and, consequently, a whole flow field can be estimated. Recently, PIV technique has been further developed and successfully applied to study gas-liquid multiphase flows (Hassan 2002, Bröder and Sommerfeld 2002).

Other optical velocimetry techniques that have been applied in gas-liquid flows are the laser Doppler anemometry (LDA) and derived techniques (Chaouki *et al.* 1997, Bauckhage 1996) which yield well-localized values of liquid velocity. The measurements are usually very fast, allowing to determine velocity fluctuations.

Hot wire (or hot film) anemometry probes have been applied to two-phase flows for the measurement of fluid velocities since the 1960s (Jones and Delhay 1976). This technique is based on the cooling effect a fluid flow causes in an electrically heated metal wire (or film). The wire's resistance is proportional to its temperature and based on heat transfer principles, the heat flux to the surrounding fluid can be inferred and thereby the fluid velocity. More recently two- and three-film probes were introduced for the determination of other velocities components (Bruuns 1995).

There is a recent trend to combine modalities (called multimodality approach) in order to enhance the applicability of unique modality techniques, thus offering the potential for greater detail and better accuracy in the flow measurement. A few examples of multimodality systems have been reported so far, for instance: resistance, capacitance and ultrasonic tomography (Hoyle *et al.* 2001), γ -ray and capacitance tomography (Hjertaker *et al.* 2005), combined electrical and ultrasound measurements (Dyakowski *et al.* 2005), and ECT/ERT system (Marashdeh *et al.* 2007).

2.2.5 Overview

As discussed throughout the section 2.2, each one of the above techniques has its advantages, disadvantages and limitations. An overview over the different measuring techniques is given in Table 2.1 along with some parameters for comparison. The choice of a particular technique is dependent on many, sometimes competing, aspects which include:

- physical properties of the constituents of a multiphase flow,
- parameter of interest (e.g. phase distribution, velocity),
- temporal resolution,
- local, integral or spatially resolved measurements,
- issues regarding flow confinement (e.g. pipe/vessel material and geometry),
- temperature and pressure in pipe or vessel,
- cost of equipment/installation,

- physical dimensions of devices (transportability), and
- potential hazards to personnel involved (e.g. radiation protection).

Table 2.1: Comparison of gas-liquid two-phase flow measuring techniques. Spatial resolution: (A) ≈ 1 mm, (B) 2-5 mm, (C) > 5 mm. Temporal resolution: (I) minute, (II) second, (III) millisecond, (IV) microsecond. Cost: (\$) low, (\$\$) medium, (\$\$\$) high.

Technique	Spatial resolution	Temporal resolution	Cost	Comments
Needle probe	B ¹	IV	\$	intrusive
Cross-sectional measurement	No	IV	\$	no imaging
x-ray and γ -ray CT	A	I,III ²	\$\$\$	ionizing radiation, safety issues
Neutron CT	A	I	\$\$\$	bulky and complex apparatus
MRI	A	I	\$\$\$	not suitable for magnetic and electrically conducting walls
PET	B	I,III ³	\$\$\$	need of radioisotope labeling
Optical CT	B	IV	\$	only suitable for low void fractions and transparent walls and fluids
Ultrasound CT	B	III	\$\$	only suitable for low void fractions
Electrical CT	C	III	\$	soft-field problems
PIV, high speed camera	A	III, IV	\$\$	only suitable for low void fractions and transparent walls and fluids
Wire-mesh sensor	B	IV	\$	intrusive, only for conducting fluids

1) achieved by mechanical movement of probe, 2) recent developments, 3) PEPT

2.3 Conclusions

The study of multiphase flow phenomena is a challenging field involving multidisciplinary knowledge disciplines. Experiments and reliable experimental techniques are essential tools to improve the understanding about multiphase flows. Two-phase gas-liquid flow are among the most import types of multiphase flow and occurs extensively throughout industries, for instance, in boilers, gas and oil transport pipelines, chemical processes.

In this chapter some essentials of gas-liquid flows were presented. Furthermore, the principles of the major measuring techniques for the investigation of such flows were revised and discussed. Although much progress has been made in the last years in the development and application of flow measurement techniques, none of the proposed techniques can claim a universal applicability or absolute accuracy for multiphase flow measurement. Notably is need for high-speed flow measurement and imaging required to investigate highly transient flows, which has mostly motivated the work of this thesis. In this fashion, there is a need of innovative measuring techniques which may fulfill the gap left open by current techniques. In this thesis, three novel sensors based on impedance measurements are introduced. Thus, following the current trend for multimodality techniques, a novel dual-modality conductivity/permittivity needle probe is presented in chapter 4. A further development of current wire-mesh sensor is described in chapter 5, where capacitance (permittivity) measurements are used allowing the sensor to be employed in the investigation of non-conducting fluids too. Finally, a novel non-intrusive sensor modality for imaging fluid distributions and near-wall flows is introduced in chapter 6.

3 Electrical impedance measurements in fluids

Impedance measurement is commonly used for circuits, components, material or solution characterization. In this chapter the theory of impedance and its measurement is reviewed with focus on the impedance measurement in fluids. This chapter starts with some basic definitions. Further it describes the electrical properties of fluids and reviews the different impedance measuring techniques. The auto-balancing bridge method is discussed in detail. Finally, first impedance measurements results with a simple probe are presented.

3.1 *Electrical properties of fluids*

Fluids as well as matter in general may be classified according to their electromagnetic properties. Although some fluids such as ferrofluids have appreciable magnetic properties, most of them are non-magnetic. On the other hand, all fluids present electrical properties, which is the focus of this section. The following description is mainly based on the books from Dorf (2000) and Macdonald (1987).

3.1.1 Definitions: impedance and complex permittivity

In electrodynamics the impedance describes the relationship between voltage and current for non-steady-state behavior. Mostly a sinusoidal alternating current (ac) is considered. A voltage $v(t) = V \cos(\omega t + \theta_v)$ at angular frequency $\omega = 2\pi f$ is applied to a material or circuit and the resulting electrical current $i(t) = I \cos(\omega t + \theta_i)$ is measured. The resulting impedance \mathbf{Z} is calculated by Ohm's law in complex notation

$$\mathbf{Z} = \frac{\mathbf{V}}{\mathbf{I}}, \quad (3.1)$$

where $\mathbf{V} = V \exp(j\theta_V)$ is the complex voltage, $\mathbf{I} = I \exp(j\theta_I)$ the complex current, and $j = \sqrt{-1}$ the imaginary unit. Hence the impedance is a complex value

$$\mathbf{Z} = \frac{V}{I} \exp(j(\theta_V - \theta_I)) = Z \exp(j\theta_Z) \quad (3.2)$$

having a magnitude or modulus Z and a phase angle θ_Z . Note that in this thesis the bold-faced variables such as \mathbf{Z} represent a complex quantity or in other cases vectors.

The concept of impedance assumes that electrical properties of the material/circuit are time-invariant. Impedance is a more general concept than resistance because it takes phase differences between voltage and current into account, and it has become a fundamental and essential concept in electrical engineering. The impedance has frequently been designated as the ac impedance or the complex impedance. Both these modifiers are redundant and should be omitted. Sometimes it is more convenient to use the inverse of \mathbf{Z} , the admittance

$$\mathbf{Y} = \frac{\mathbf{I}}{\mathbf{V}} = \frac{1}{\mathbf{Z}} = Y \exp(j\theta_Y) = \frac{1}{Z} \exp(-j\theta_Z). \quad (3.3)$$

The word "imittance" was proposed by Bode (1959) and is a combination of the words "impedance" and the reverse quantity "admittance". These terms do not only occur in electrodynamics but wherever wave propagation takes place - in acoustics as well as in elasticity. Figure 3.1 shows their representation in the complex plane. Equations (3.2) and (3.3) give the definition in polar coordinates. Using Euler's identity $\exp(j\theta) = \cos(\theta) + j\sin(\theta)$, one obtains in rectangular coordinates

$$\mathbf{Z} = Z \cos(\theta_Z) + jZ \sin(\theta_Z) = R + jX, \quad (3.4)$$

$$\mathbf{Y} = Y \cos(\theta_Y) + jY \sin(\theta_Y) = G + jB. \quad (3.5)$$

From Figure 3.1 it is easy to demonstrate that

$$Z = \sqrt{R^2 + X^2}, \quad Y = \sqrt{G^2 + B^2}, \quad (3.6)$$

$$\theta_Z = \tan^{-1}\left(\frac{X}{R}\right), \quad \theta_Y = \tan^{-1}\left(\frac{B}{G}\right). \quad (3.7)$$

The real parts are the resistance R and the conductance G . They indicate the losses within the circuit. The imaginary parts, which are termed reactance X and

susceptance B , respectively, are a measure of the reactive energy stored in the circuit during one period. In general, all these quantities are frequency-dependent.

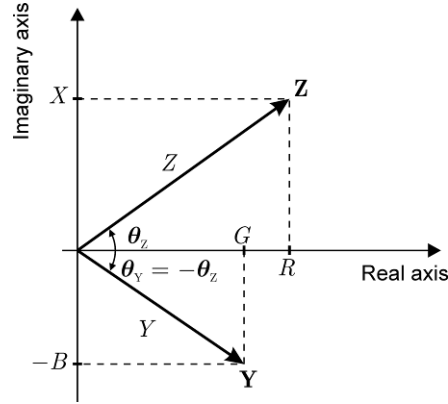


Figure 3.1: Representation of impedance and admittance in the complex plane showing the relations between rectangular and polar coordinates. Note that the units are different for each vector.

Impedance is by definition a complex quantity and is only real when $\theta = 0$ and thus $\mathbf{Z} = R$, that is, for purely resistive behavior. The impedance of ideal inductors and capacitors is purely imaginary with different signs according to the phase shift of $\pm 90^\circ$ between voltage and current. A general element or network is therefore called inductive or capacitive at a given frequency corresponding to the sign of the imaginary part of its impedance.

The above definitions apply very well in circuit and network theory. However, a much more common parameter used to characterize materials is the complex relative permittivity ϵ . This quantity is related to the complex absolute permittivity $\epsilon_a = \epsilon_0 \cdot \epsilon$, where $\epsilon_0 = 8.85 \text{ pF/m}$ is the permittivity of free space. The relative permittivity ϵ is a dimensionless quantity. In this thesis the complex relative permittivity will be referred to as complex permittivity, denoted by ϵ , only. As its name indicates it is a complex quantity

$$\epsilon = \epsilon' - j \cdot \epsilon'' \quad (3.8)$$

comprising a real part ϵ' (commonly called the permittivity) and imaginary part ϵ'' or the loss factor. According to

$$\mathbf{D} = \epsilon_0 \epsilon \mathbf{E} \quad (3.9)$$

the complex permittivity ϵ relates the dielectric displacement \mathbf{D} to the electric field strength \mathbf{E} . A more detailed and general description of the complex permittivity concept based on Maxwell's equations is given in Appendix B. Basically, the real part of the complex permittivity describes the ability of a material to support an electrical field, i.e. a measure of energy storage, and the imaginary represents the losses in the material. These losses include dielectric loss due to relaxation or resonant effects in the materials as well as loss by ionic conduction. More details of these phenomena are described in section 3.1.2. Under complex phasor notation (see Appendix B.1), the fields are assumed to present sinusoidal alternating variations with time. Thus, the losses in the material are manifested as phase angle difference between \mathbf{D} and \mathbf{E} fields. Therefore, it is customary to assess the magnitude of loss of a given material in terms of the value of its dissipation factor or loss tangent

$$\tan \theta = \frac{\epsilon''}{\epsilon'} \quad (3.10)$$

where θ denotes the phase angle between \mathbf{D} and \mathbf{E} fields. This value is high for lossy (or conductive) materials.

Impedance measurements to investigate solid, liquid or gaseous substances are carried out with the help of a measuring cell or probe. The simplest cell is composed by two identical parallel plane electrodes as shown in Figure 3.2. The relationship connecting the electrical properties of the substance between the plates with the measured cell admittance is

$$\mathbf{Y} = j\omega k_g \epsilon_0 \epsilon. \quad (3.11)$$

The geometry factor k_g reflects the ratio of the cross-sectional area of the sampled fluid volume and the length or distance between the electrodes. For the simple cell of Figure 3.2 it may be approximate to

$$k_g = \frac{l^2}{d} = \frac{A}{d}, \quad (3.12)$$

where A is the area of the square plates of side l , and d the distance separating them. Here the fringing effects are neglected. For more complex geometries, k_g can be theoretically estimated based on analytical solutions or simulations as well as experimentally determined with the help of reference measurements.

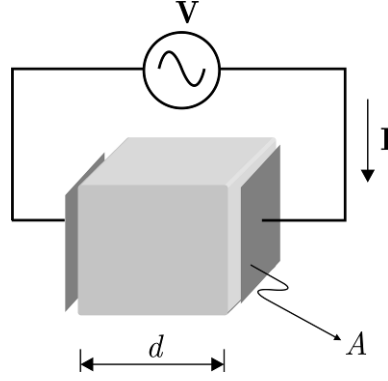


Figure 3.2: Example of a simple measuring cell.

Each one of the particular representations of impedance-related functions can be easily converted into any other. Table 3.1 shows the conversion between the most important parameters described in this section. While the complex permittivity ϵ is only dependent of the material properties, admittance \mathbf{Y} and impedance \mathbf{Z} do also depend on the experimental setup via the geometry factor k_g .

Table 3.1: Relations between some impedance-related functions. $C_c = k_g \epsilon_0$ represents the capacitance of the empty measuring cell.

	\mathbf{Z}	\mathbf{Y}	ϵ
$\mathbf{Z} =$	-	\mathbf{Y}^{-1}	$(j\omega C_c)^{-1} \epsilon^{-1}$
$\mathbf{Y} =$	\mathbf{Z}^{-1}	-	$j\omega C_c \epsilon$
$\epsilon =$	$(j\omega C_c)^{-1} \mathbf{Z}^{-1}$	$(j\omega C_c)^{-1} \mathbf{Y}$	-

Some other impedance-related functions have been used to characterize materials in the literature, though having lesser importance for the present work. One of these functions is the modulus function $\mathbf{M} = \epsilon^{-1}$. Furthermore, some researchers investigating ionic liquids have used a parameter called complex conductivity σ or admittivity κ which is related to the complex permittivity by $\sigma = \kappa = j\omega \epsilon_0 \epsilon$. Though all parameter are equivalent, for clarity only the parameters of Table 3.1 will be employed.

Yet, the term impedance (immitance) spectroscopy or dielectric spectrometry are often used to indicate the measurement of electrical properties of materials over a spectrum of frequencies. Impedance spectroscopy plays an important role in fundamental and applied electrochemistry and materials science (Macdonald 1987).

3.1.2 Dielectric relaxation

The complex permittivity ϵ of fluids, though not always, shows dielectric relaxation in which ϵ' decreases with increasing frequency. A fluid may have several dielectric mechanisms or polarization effects that contribute to its overall permittivity. Figure 3.3 depicts schematically the different dielectric mechanics. Dipole orientation and ionic conduction interact strongly at radio waves and microwave frequencies. Atomic and electronic mechanisms occur predominately in the optical frequencies. Each dielectric mechanism has a characteristic frequency. As frequency increases, the slow mechanisms drop out in turn, leaving the faster ones to contribute to the permittivity. The nonrelaxation-type ionic conduction losses are readily perceptible over the low-frequency spectrum and decrease monotonically with frequency.

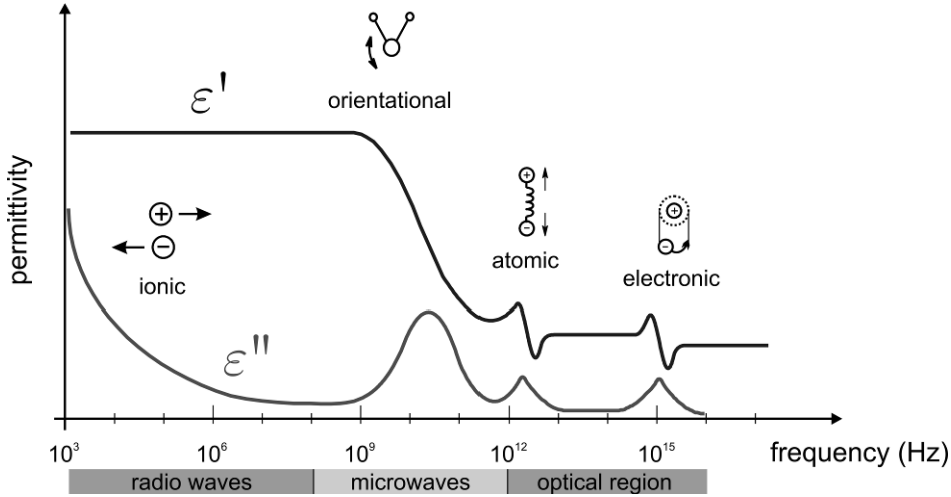


Figure 3.3: Schematic representation of different dielectric mechanism. Slightly modified from Agilent (2006a).

The dielectric mechanism behavior for many fluids in the microwave frequency region is characterized by a single relaxation process. This behavior is mathematically described by the Debye equation, which relates the complex permittivity ϵ to the relaxation time τ of the relaxation process, the low-frequency or static value of the real permittivity ϵ_s , and the high- or optical-frequency value of the real permittivity ϵ_∞ . Thus, for a single relaxation process (Macdonald 1987)

$$\epsilon = \epsilon_\infty + \frac{\epsilon_s - \epsilon_\infty}{1 + j\omega\tau}. \quad (3.13)$$

The frequency at which the ϵ'' peak appears is obtained from time constant τ

$$f_c = \frac{1}{2\pi\tau}. \quad (3.14)$$

The relationship given by (3.13) omits the effects of conduction. Many liquids contain a conductivity contribution due to the motion of ion pairs with the electrical conductivity itself being independent on frequency. Thus, the model is expanded to include a static conductivity term σ (see Appendix B.3) and (3.13) is rewritten as

$$\epsilon = \epsilon_\infty + \frac{\epsilon_s - \epsilon_\infty}{1 + j\omega\tau} - j \frac{\sigma}{\omega\epsilon_0}. \quad (3.15)$$

Even if σ is relatively small as is the case of insulators it may dominate ϵ at sufficiently low frequencies. The real and imaginary parts of (3.15) are given by

$$\epsilon' = \text{Re}\{\epsilon\} = \epsilon_\infty + \frac{\epsilon_s - \epsilon_\infty}{1 + (\omega\tau)^2} \quad (3.16)$$

and

$$\epsilon'' = \text{Im}\{\epsilon\} = \frac{\sigma}{\omega\epsilon_0} + \frac{\omega\tau(\epsilon_s - \epsilon_\infty)}{1 + (\omega\tau)^2}. \quad (3.17)$$

In Figure 3.4, ϵ' and ϵ'' are exemplary plotted according to (3.16) and (3.17) for water at 25°C for two different conductivity values.

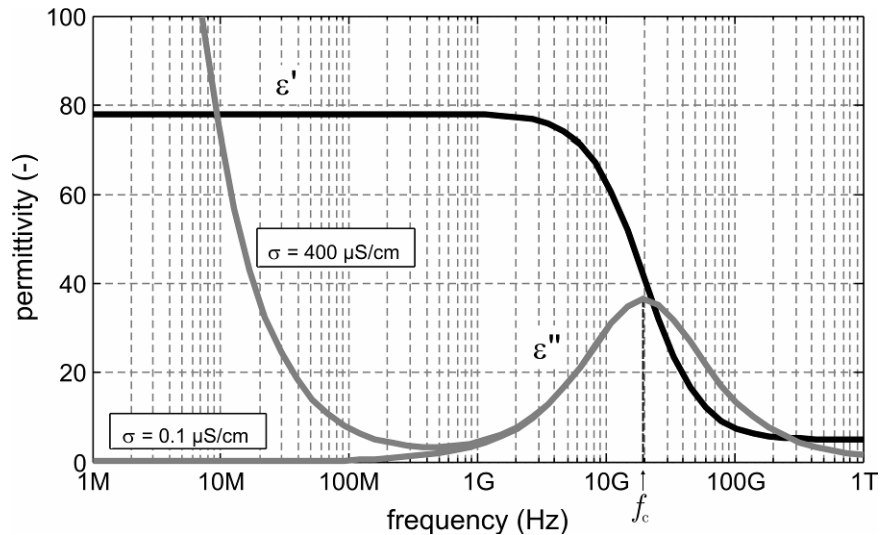


Figure 3.4: Real and imaginary parts of the complex permittivity for water at 25°C according to the Debye relaxation function. Permittivity and time constant values were taken from Table 3.2. Conductivity values σ were arbitrarily chosen; 0.1 $\mu\text{S}/\text{cm}$ corresponds to deionized water and 400 $\mu\text{S}/\text{cm}$ to tap water.

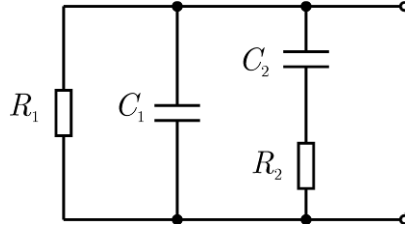


Figure 3.5: Equivalent circuit representing Debye equation (3.15).

Debye equation (3.15) can also be expressed as an equivalent circuit shown in Figure 3.5 with the identities:

$$\begin{aligned}
 R_1 &= \frac{1}{k_g \sigma} \\
 C_1 &= k_g \varepsilon_0 \varepsilon_\infty \\
 C_2 &= k_g \varepsilon_0 (\varepsilon_s - \varepsilon_\infty) \\
 R_2 &= \frac{\tau}{C_2}
 \end{aligned} \tag{3.18}$$

where k_g represents the geometry factor of the measuring cell.

In practice not all fluids obey the simple Debye equation. A number of other empirical Debye-type functions have been proposed to describe the behavior of materials (Macdonald 1987). Those relations assume not only one single relaxation time τ but multiple relaxation times. One of the most widely used functions is the so-called Cole-Cole equation

$$\varepsilon = \varepsilon_\infty + \frac{\varepsilon_s - \varepsilon_\infty}{1 + (j\omega\tau)^{1-\beta}}, \tag{3.19}$$

where β is a parameter which gives a measure of the broadening in the peak of ε'' , indicating a distribution of relaxation times (Macdonald 1987). For $\beta = 0$, (3.19) becomes the Debye equation (3.15). Cole-Cole equation (3.19) was used for the characterization of a wide variety of liquids. The parameters for a few exemplary liquids are given in Table 3.2.

From the values for τ of Table 3.2 and (3.14) it is easy to show that all relaxation processes occur in the GHz-range. In this thesis the frequency range of measurements is limited to a few tens of MHz. As a result, the relaxation mechanisms can be disregarded and from now on the complex permittivity of a fluid will be treated as its low-frequency equivalent, which is given by

$$\epsilon = \epsilon - j \frac{\sigma}{\omega \epsilon_0}, \quad (3.20)$$

where ϵ will be used to represent the static relative permittivity ϵ_s (sometimes called the dielectric constant). Furthermore, the equivalent low-frequency circuit of a liquid is given by the parallel connection of a capacitor and a resistor, whose admittance is obtained by putting (3.20) in (3.11), yielding

$$\mathbf{Y} = k_g (\sigma + j\omega \epsilon_0 \epsilon). \quad (3.21)$$

Separating (3.21) in real and imaginary parts and remembering that $\mathbf{Y} = G + j\omega C$, the conductance G and the capacitance C are obtained as follows.

$$\begin{aligned} G &= k_g \sigma \\ C &= k_g \epsilon_0 \epsilon \end{aligned} \quad (3.22)$$

Table 3.2: Dielectric relaxation parameters for selected liquids at 25°C. All values except that one for crude oil were taken from Buckley and Maryott (1958). Crude oil values according to Folgerø (1998).

Substance	ϵ_∞	ϵ_s	β	τ (ps)
2-Propanol	3.2	20	0	291.78
Air	1	-	-	-
Crude oil	2.32	2.19	0.52	11.30
Diethyl Ether	1.82	4.24	0	2.17
Ethanol	4.2	24	0	127.85
Ethylene Glycol	3	37	0.23	79.57
Water (deionized)	5	78	0	8.08

3.2 Impedance measuring techniques

3.2.1 Overview

Since impedance is a complex quantity, one must determine two parameters: magnitude and phase or real and imaginary part of voltages or currents, commonly denominated as vector measurements. The general approach to measure impedance is

to apply an electrical stimulus (a known voltage or current) to the electrodes and observe the response (the resulting current or voltage).

Basically, there are three different types of electrical stimuli which are used for impedance measurements.

- 1) The most common and standard one, is to measure impedance by applying a single-frequency (pure sine wave) voltage and measuring the phase shift and amplitude, or real and imaginary parts, of the resulting current at that frequency using either analog circuit or analog-to-digital conversion and signal processing algorithm to analyze the response.
- 2) The second approach is to apply a transient voltage, e.g. a pulse or a step function, and to measure the resulting time-varying current. Both input and output signals are Fourier-transformed into the frequency domain, yielding frequency-dependent impedance.
- 3) A third technique is to apply a voltage signal composed of random (white) noise and measure the resulting current. The frequency-dependent impedance can be calculated from the power density spectra of input and output signals.

The latter two approaches measure the impedance over a range of frequency and are therefore classified as broadband measurements. Both need rather complex signal generation and processing, making it difficult for high-speed measurements. Therefore, the first approach is more appropriate for the work of this thesis.

Independent of the type of stimulus, there also exist several techniques for impedance measurement depending on frequency range, required accuracy, measurement range, and system complexity. For more details of the current measuring techniques the recent review by Kaatzé and Feldman (2006), and the works Agilent (2006b) and Macdonald (1987) are indicated.

Measurement of voltages and currents at microwave frequencies (> 100 MHz) are difficult and often not directly applicable to high-frequency devices. For that reason, the determination of impedances is derived from measurements of reflection and transmission of waves in conjunction with the concept of distributed circuits. Commercial network analyzers and time domain reflectometers are widely used for this purpose (Agilent 2006b, Gregory and Clarke 2006).

At lower frequencies (up to MHz range) impedance is determined using lumped circuits, which are measured by current–voltage (or I-V), bridge or resonant methods

(Agilent 2006b). Since in this thesis the low-frequency range is of particular interest, these methods are briefly described below.

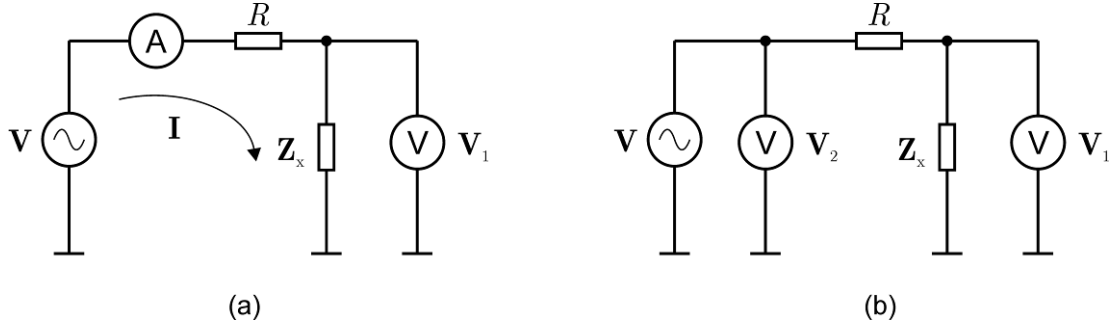


Figure 3.6: The I-V measuring method for determining the impedance. (a) Principle of measurement. (b) More practical circuit using voltage measurements only.

3.2.2 Low-frequency methods

a) Direct measurement

A simple way to measure impedances follows directly from its defining equation (3.1). Applying a known sinusoidal voltage to the terminal and measuring magnitude and phase of the current, or vice-versa, gives the desired quantity (Figure 3.6a). The phase angle information is obtained by comparing the relative phase between voltage and current by means of a phase detector. A variant on this method using only the better practicable voltage measurements is shown in Figure 3.6b. One finds that

$$\mathbf{Z}_x = \left(\frac{\mathbf{V}_1}{\mathbf{V}_2 - \mathbf{V}_1} \right) R. \quad (3.23)$$

In both cases, the resistor R must be accurately known and small compared to the modulus of impedance $Z_x = |\mathbf{Z}_x|$ to achieve reliable measurements.

b) Bridge circuits

A second approach is the bridge circuit which has been widely used for the measurement of impedances. Alternating current bridges are low-cost standard laboratory devices to measure impedances over a wide frequency range from dc up to 300 MHz with very high precision. The general configuration is shown in Figure 3.7.

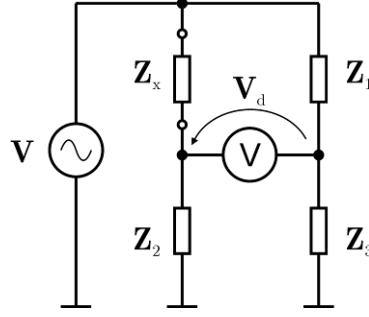


Figure 3.7: Basic bridge circuit for impedance measurement.

Their working principle is based on the fact that if the bridge is balanced, i.e. the voltage V_d is zero, the following condition holds

$$\frac{Z_x}{Z_2} = \frac{Z_1}{Z_3}. \quad (3.24)$$

Thus by adjusting one or other arm of the bridge, the balancing condition is reached and the unknown impedance can be calculated with (3.24). Since the quantities are complex, (3.24) involves the adjustment of two parameters to achieve balance: magnitude and phase or real and imaginary part of V_d . In this way, if the impedances Z_1 , Z_2 and Z_3 are known, it yields

$$Z_x = \frac{Z_1}{Z_3} Z_2 \quad \text{and} \quad \theta_x = \theta_1 - \theta_3 + \theta_2. \quad (3.25)$$

In practice, the impedances Z_1 , Z_2 and Z_3 are connections of resistors and capacitors. Inductors are usually avoided because they always have a resistive component and it is difficult and expensive to manufacture inductors with exactly defined and reproducible electrical properties. There exist various types of bridges depending on how the elements are designed and interconnected. To choose the correct configuration, it must be known whether the unknown impedance is capacitive or inductive. Otherwise, a zero adjustment is not always possible since the balancing condition may not be fulfilled. In the case that only changes in the impedance are to be measured, the bridge may be operated out of balance. This type of operation is known as deflection-type bridge. For this condition, the complex voltage V_d is proportional to the unknown impedance Z_x

$$\frac{V_d}{V} = \frac{Z_2}{Z_x + Z_2} - \frac{Z_3}{Z_1 + Z_3}. \quad (3.26)$$

Frequently used bridge circuits are the Wheatstone, Hay, Maxwell and Schering Bridge (Oliver and Cage 1971, Morris 2001, Bera and Chattopadhyay 2003).

c) Resonant methods

The third method is called resonant method. As its name already indicates, it makes use of the resonance effect of LC circuits to determine the impedance. Typical circuit configurations are shown in Figure 3.8. The resonant frequency is given by

$$f_r = \frac{1}{2\pi\sqrt{LC}}. \quad (3.27)$$

This method also requires a previous knowledge of if the impedance under test is capacitive or inductive in order to compose an appropriate resonant circuit. That means, at least one component L or C must be previously known. Basically, two strategies have been used for determining the reactance (L or C) of a resonant circuit. The excitation frequency may be varied searching for the resonance condition, where the measured voltage at R achieves a maximum, or the RLC network is connected being part of an oscillator circuit, in which the output frequency is accurately measured. Both strategies are equivalent and the unknown reactance can be obtained using (3.27).

The fact that at resonance condition the imaginary part of circuit impedance vanishes can be used to determine the resistive part of impedance. Hence,

$$R_x = \frac{V_r}{I_r}, \quad (3.28)$$

where V_r and I_r are the voltage and current values measured at resonance.

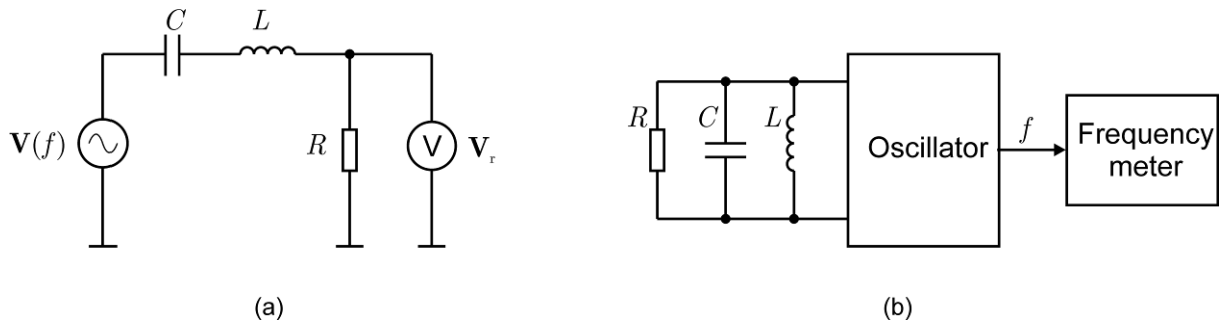


Figure 3.8: Typical resonant circuits for the measurement of impedance. (a) General principle of measurement. (b) Variant of (a) where the oscillator output frequency f is a measure of the unknown quantity (L or C).

d) Comparison

Although, in principle, all three measuring methods are equivalent and might be employed for the impedance measurements of fluids, they are not always appropriate. The I-V method though being very simple has a low accuracy. The bridge method exhibits high accuracy, but due to the need of balancing this method is considered not suitable for fast, repeated and continuous measurements. The resonant method achieves good accuracy but there also is a need for resonance tuning, thus resulting to the same problem like for bridge circuits. Deflection bridges do not need any balancing. However the high number of components constituting a bridge circuit is undesired in multichannel systems. Furthermore, all above methods are sensitive to stray capacitances to ground which are usually present in measuring probes due to, for instance, connecting cables or other grounded metallic parts of a probe. Such stray capacitances may falsify the impedance measurements and must be compensated leading to more complex circuits.

As a result of these limitations of the standard methods, the chosen method for measuring impedance in this work is an improved variant of the I-V method previously discussed, called auto-balancing bridge. It will be described in detail in the next section. The auto-balancing bridge is a simple, accurate, fast response and stray-capacitance immune circuit, thus being well suited for high-speed impedance measurements in multiphase flows. Furthermore, due to the small component count the circuit is optimal for the use in multichannel systems.

3.3 The auto-balancing bridge

3.3.1 Circuit analysis

The I-V method is the simplest way to measure impedance. However its use is limited to only few applications. The measurement can be enhanced using an operational amplifier (opamp) with high input and low output resistance (Figure 3.9). This circuit configuration is synonymously known as auto-balancing bridge, transimpedance amplifier or current-voltage converter. This type of circuit is typical for many types of impedance measuring circuits and has also been successfully used in ECT systems (Yang and York 1999) where is denominated ac-based measuring method. It presents high signal-to-noise ratio and stray-capacitance immunity, i.e. it is able to measure small inter-electrode impedances in the presence of large stray

capacitances to ground. Furthermore, it has a fast response time and is thus suitable for high-speed measurements.

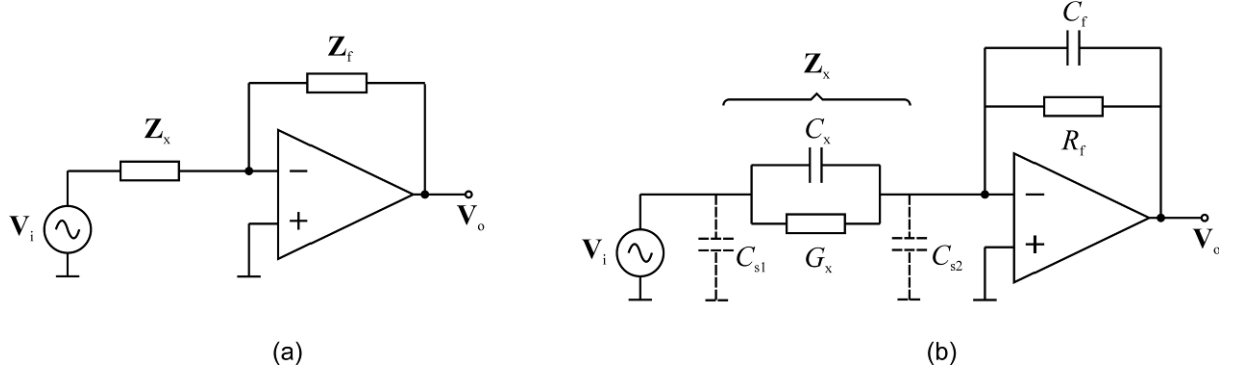


Figure 3.9: (a) Basic circuit configuration of the auto-balancing bridge impedance measuring method. (b) Practical circuit for measuring capacitive impedances formed as parallel circuit of a capacitor and a resistor.

The basic circuit diagram is given in Figure 3.9a, where V_i is the excitation voltage, Z_x represents the unknown impedance and Z_f the feedback network. The potential at the operational amplifier inverting pin is maintained at zero thus called virtual ground. In this way, the current through Z_f balances with the Z_x current by the action of the opamp which increases its output voltage to compensate the current through Z_f .

The impedance is calculated using voltage measurement at the opamp output. Assuming that the opamp is ideal the output voltage V_o is determined by

$$\frac{V_o}{V_i} = -\frac{Z_f}{Z_x} = -\frac{Y_x}{Y_f}. \quad (3.29)$$

A practical circuit for the measurement of capacitive impedances, which are in scope of this thesis, is shown in Figure 3.9b. The impedances Z_x and Z_f are formed by the parallel circuit of a resistor and a capacitor. Further, C_{s1} and C_{s2} represent the stray capacitances to ground which are caused, for instance, by cables used to connect the circuit with a sensor. In principle, these stray capacitances have no influence in the circuit since C_{s1} is directly driven by the source voltage and C_{s2} is virtually grounded by the opamp. From (3.29) and (3.5) one obtains

$$\frac{V_o}{V_i} = -\left(\frac{G_x + j\omega C_x}{G_f + j\omega C_f}\right), \quad (3.30)$$

where $\omega = 2\pi f$ and f is the frequency of the excitation signal.

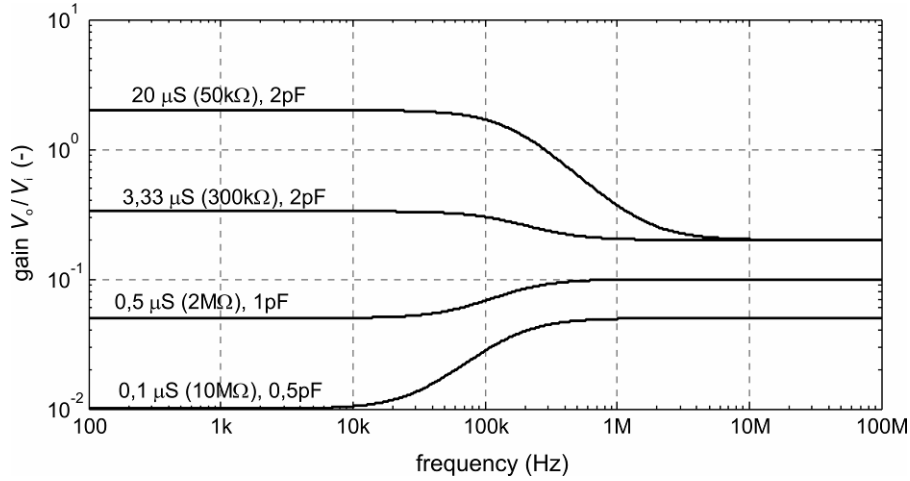


Figure 3.10: Frequency response of the auto-balancing bridge circuit of Figure 3.9b for typical expected component values. $C_f = 10$ pF, $G_f = 10$ μ S (100 k Ω), C_x and G_x (R_x) are indicated in the plots.

The determination of the two unknown in (3.30), i.e. C_x and G_x , involves the measurement of two quantities which might be:

- (a) amplitude and phase at a single frequency,
- (b) real and imaginary parts of \mathbf{V}_o at a single frequency (for instance with an IQ-demodulator) or
- (c) two amplitudes at different frequencies.

Mathematically speaking, all these approaches are equivalent but from the metrological point of view they basically differ in the circuit complexity, implementation and uncertainties in the measured values. In the past all three approaches have been successfully employed. A discussion on this issue is given by Georgakopoulos *et al.* (2003). The former two measuring strategies (a) and (b) are a direct consequence of the complex quantity nature of impedance and will not be further discussed here. For a better understanding of the third approach, the circuit frequency response will be closer analyzed. Taking the modulus of (3.30) one obtains

$$\left| \frac{\mathbf{V}_o}{\mathbf{V}_i} \right| = \left| \frac{\mathbf{Y}_x}{\mathbf{Y}_f} \right| = \frac{\sqrt{G_x^2 + (2\pi f)^2 C_x^2}}{\sqrt{G_f^2 + (2\pi f)^2 C_f^2}}. \quad (3.31)$$

The theoretical frequency responses of the circuit from Figure 3.9b for typical values expected in the investigation of fluids are plotted in Figure 3.10. Two plateaus can be easily identified. The magnitude of each plateau is given by the quotient of

G_x/G_f and C_x/C_f which are obtained taking the limit for $f \rightarrow 0$ and $f \rightarrow \infty$ of (3.31). In principle, any two frequencies may be chosen for determining the unknown components. The simplest choice is to select two frequencies located exactly in each plateau (Da Silva *et al.* 2005).

The analysis presented previously considered an ideal opamp with infinite frequency response. Nevertheless, the frequency response of the opamp also influences the overall circuit response and was not included in (3.31). Practical and theoretical analysis of non-ideal opamp characteristic is given by Gamio *et al.* (2001). One of the conclusions from that work is that the opamp includes a second pole to the overall response located at the higher frequencies caused by the finite bandwidth of an opamp. Although the authors had focused on capacitance measurement only, the conclusions there can be used for the general impedance case here. A simplified (asymptotic) frequency response of the auto-balancing bridge circuit is illustrated in Figure 3.11.

The proper dimensioning of the feedback network, i.e. C_f and G_f , plays an important role for the correct operation of the auto-balancing bridge. Here the operation frequency and the characteristics of the opamp used must be taken into account. Furthermore, in many practical situations only one parameter C_x or G_x are of interest or are present as physical quantity. In this way, the circuit may then be dimensioned as capacitance or resistance dominant, respectively.

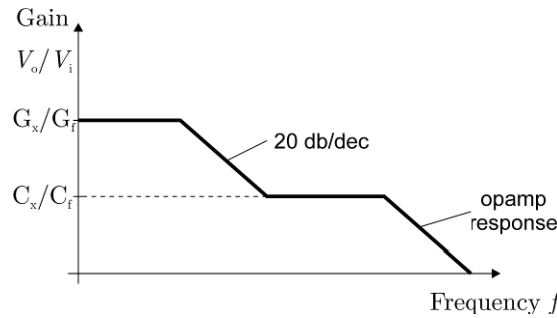


Figure 3.11: Schematic and simplified frequency response of a practical auto-balancing bridge taking into account the opamp non-ideal frequency response.

3.3.2 Simple measuring cell

To confirm the theoretical analysis, a preliminary investigation of the auto-balancing bridge circuit in the measurement of the electrical properties of selected liquids and air was carried out and is described in this section. For this purpose the experimental setup depicted in Figure 3.12 was used.

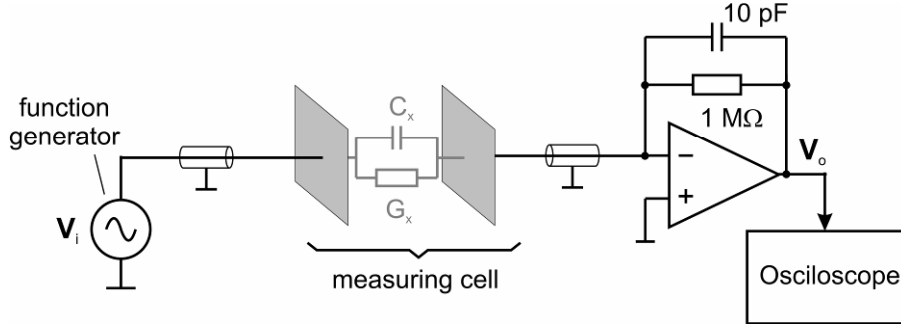


Figure 3.12: Experimental setup for the measurement of electrical properties of selected substances.

The function generator (Agilent 33250A) was configured to sweep a sine voltage with constant amplitude of $10 V_{pp}$ from 1 kHz to the maximum frequency achievable of 80 MHz in a time span of 500 ms. The output voltage of the opamp was monitored with an oscilloscope (Tektronix TDS2014) and the data transferred to a computer via a serial cable. The raw data for each measurement was peak-detected and low-pass filtered using signal processing algorithms so that only the envelope of the sine wave voltage was detected. The opamp employed was the OPA656 (Texas Instruments) which has a FET input and gain-bandwidth product of 230 MHz hence being suitable for high-impedance and high-frequency measurements. The measuring cell was built with simple rectangular parallel-plate geometry. Five substances having different conductivity and static permittivity values in a broad range were poured in a recipient where the cell was located while the voltage spectrum response was measured as described above. Also the empty cell (air) was measured.

The measured spectra are depicted in Figure 3.13, where the two plateaus as anticipated from (3.31) can be clearly seen. The peak occurring at the frequency of about 60 MHz is caused by the decreasing phase margin due to the OPA656 frequency response which possesses a further non-dominant pole at about 400 MHz.

Each substance can be easily distinguished from each other either in the low-frequency (resistive) plateau other in the high-frequency (capacitive) one. As previously described the conductance and capacitance of the measuring cell are linked respectively to the electrical conductivity and permittivity of the substance under test. A quantitative analysis is presented in Figure 3.14, where the measured gain at the low-frequency and high-frequency plateaus was plotted against the reference electrical properties of the investigated fluids, i.e. electrical conductivity and permittivity. Further, the measured data were fitted to a line and the resulting parameters are shown in the respective plots. The very good agreement between the

expected linear dependence and the obtained regression lines is confirmed by the good correlation coefficients of about 0.99; thus confirming that the circuit is well suited for the investigation of the electrical properties of fluids.

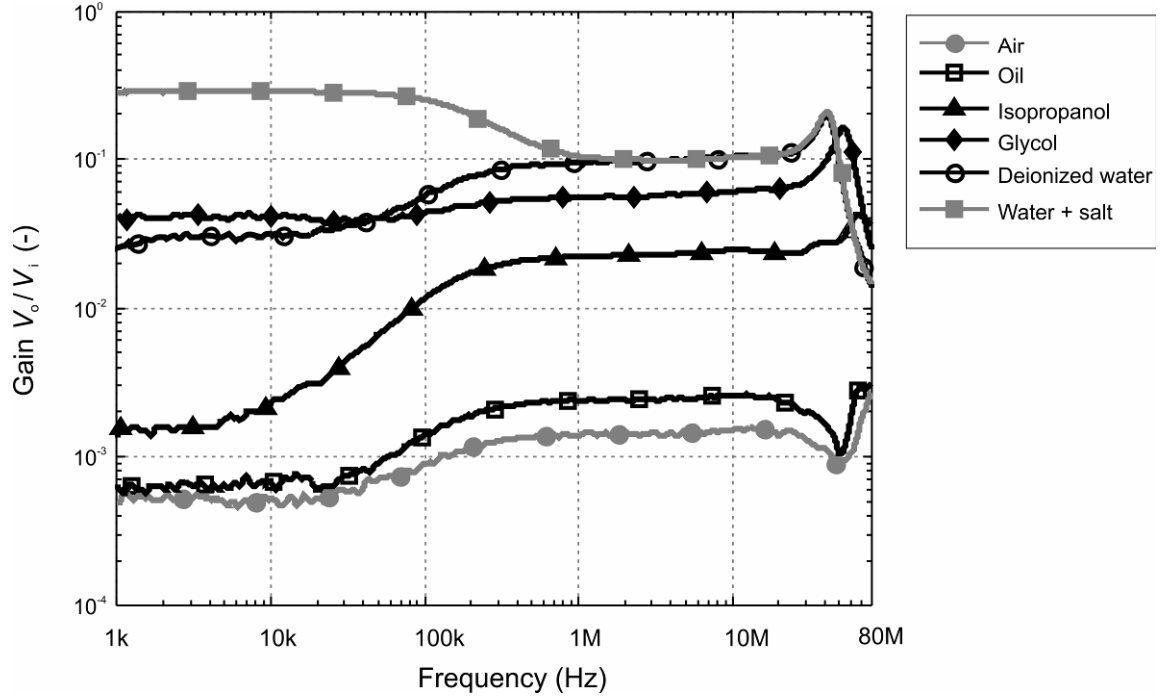


Figure 3.13: Frequency response curves for selected substances measured with setup from Figure 3.12. Air $\varepsilon = 1$, $\sigma = 0$. Oil $\varepsilon = 2$, $\sigma = 0$. Isopropanol $\varepsilon = 19$, $\sigma = 0.06 \mu\text{S/cm}$. Glycol $\varepsilon = 37$, $\sigma = 3 \mu\text{S/cm}$. Deionized Water $\varepsilon = 79$, $\sigma = 2 \mu\text{S/cm}$. Water + salt $\varepsilon = 79$, $\sigma = 26 \mu\text{S/cm}$.

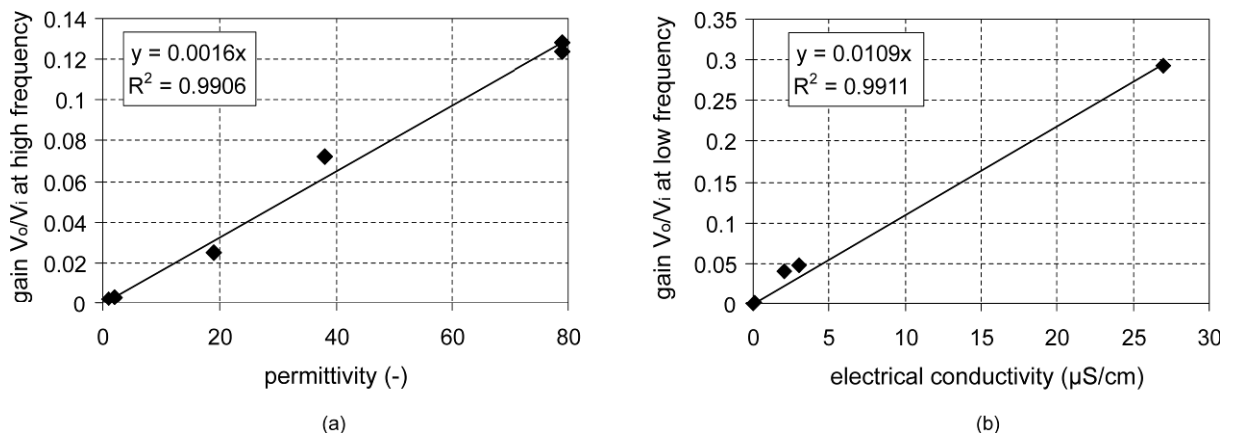


Figure 3.14: Correlations of the measured gains at low- and high-frequency plateaus with (a) electrical conductivity and (b) permittivity of tested substances, respectively. (\blacklozenge) measuring points, (—) least-squares linear fit.

3.4 Conclusions

This chapter was dedicated to review the basic electrical properties of fluids and the current-in-use techniques to measure impedances in general. The chosen technique for the investigation of fluids, the auto-balancing bridge was described in detail and its frequency response analyzed. The theoretical predictions were then confirmed by first fluid measurements with a simple measuring cell. The auto-balancing bridge is a simple and valuable technique to measure the impedance of fluids.

In this way, a solid theoretical and practical basis was established, which is applied in the development of innovative sensor systems to the investigation of multiphase flows. In this thesis three operation modes for the auto-balancing bridge were exploited in conjunction with different sensors which will be described in more detail in the following chapters along with the metrological characterization of each developed sensor system:

- in chapter 4 as impedance measuring circuit,
- in chapter 5 as capacitance measuring circuit, and
- in chapter 6 as resistance as well as capacitance measuring circuit.

4 Complex permittivity needle probe

This chapter presents a novel needle probe measuring system based on high-speed complex permittivity measurements. The measuring circuit is a direct application of the auto-balancing bridge circuit discussed in the previous chapter in conjunction with a specially designed needle probe. Such probes are able to distinguish the different phases or components of a flow by measuring the complex value of the electrical impedance at a high data rate.

4.1 Introduction

Measurement with local needle probes is a well-established method for the investigation of two-phase flows (section 2.2.1a). Needle probes can identify the phase, which is momentarily present at the location of the needle tip. Based on this local phase information, different flow parameters can be derived. A number of measuring principles have been employed for the needle probes in the past. Most sensors employ conductivity, capacitance, optical and temperature measurement techniques (Cartellier and Achard 1990). However, each one of these techniques has limitations regarding the range of substances it is able to measure. Conductivity or resistivity probes can only differentiate an electrically conducting phase from a non-conducting one. Capacitance probes encounter problems when permittivities of the two phases are similar. The same difficulty occurs with optical probes and low refractive index differences. Temperature probes require sufficient temperature differences in the substances, which are to be discriminated. Therefore, these probes have been utilized almost exclusively in two-phase flow measurements.

In recent years some efforts have been made by applying dual modality measuring techniques for enhancing the range of substances in the investigation of multiphase flows, in which two different sensing techniques are used to distinguish the different

flow constituents. Schleicher *et al.* (2008a) have developed a conductivity probe with integrated micro-thermocouple, which is able to synchronously measure temperature and conductivity and which has been applied to measure a steam-gas-water flow. An optical needle probe combining reflectance and fluorescence measurements has been reported by Ramos *et al.* (2001) for the investigation of oil-water-gas flows. A dual fiber optical needle probe was described in Fordham *et al.* (1999) also for the investigation of oil-water-gas flows, where reflectance signals of a cleaved fiber were used for gas/liquid discrimination and reflectance signals of an oblique probe for oil/not-oil discrimination.

Combination of conductivity with dielectric constant measurements could enhance the applicability of needle probe systems. Some application fields which may benefit of dual-modality conductivity/permittivity sensors are the investigation of three-phase gas-liquid-liquid flows (oil extraction and processing) as well as the monitoring of mixing processes in chemical reactors such as blending of gasoline fractions or soft drinks production.

Commercial measuring instruments like RLC meters or impedance analyzers can only achieve a few measurements per second and are thus not suitable for high-speed measurements which are required in the investigation of transient fluid flow. For this reason, a high-speed complex permittivity needle probe was developed and tested (Da Silva *et al.* 2007a). In the next sections, the system is first briefly described; followed by the characterization of the probe system and finally some applications of the new developed needle probe are presented and discussed.

4.2 System description

4.2.1 Needle probe

The developed system consists of a needle probe and a dedicated electronics responsible to generate and measure the sine wave signals required to determine the complex permittivity. The probe itself is built in a double coaxial geometry (Figure 4.1). Two stainless steel electrodes (excitation and measuring electrode) are isolated from the common ground electrode. Both coaxial structures are soldered together or placed inside a third stainless steel tube. Two needle probes with different sizes were manufactured. Figure 4.1 shows both probes and their physical dimensions. The electrical capacitance of the free pair of electrodes (sensitive area) is approximately 0.06 pF and 0.1 pF in air for the probes named "one" and "two", respectively.

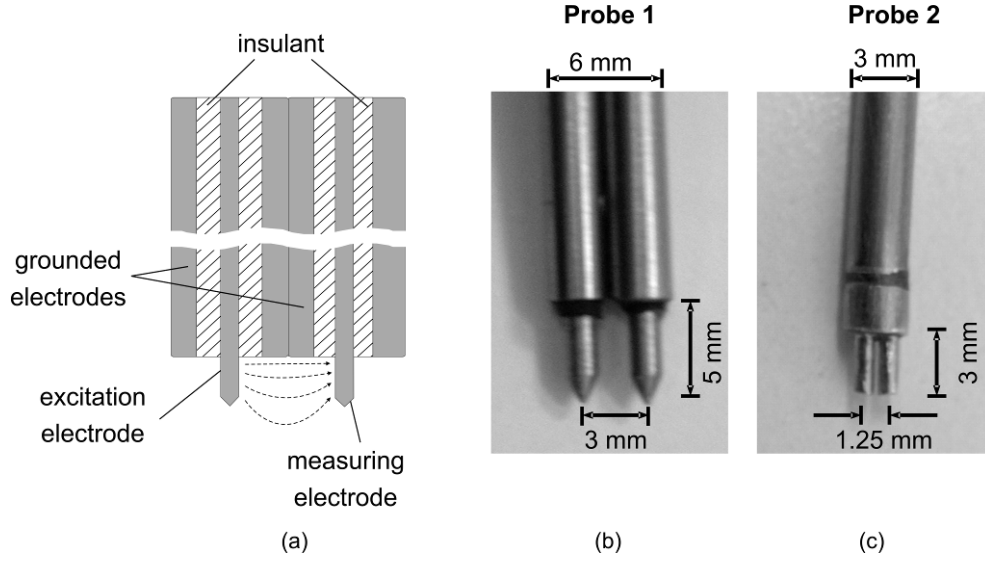


Figure 4.1: (a) Schematic diagram of a needle probe and (b,c) photographs of both manufactured probes. The electrodes are of 1 mm and 0.9 mm diameter for probe "one" and "two", respectively.

The principle of operation of the needle probe system is given as follows. The electronics applies a sinusoidally alternating voltage to the excitation electrode and determines the complex value of current (amplitude and phase) flowing from the excitation electrode towards the measuring electrode. The admittance \mathbf{Y} is calculated by Ohm's law, i.e. the ratio between current \mathbf{I} and voltage \mathbf{V} . The measured admittance is related to the electrical conductivity σ and relative permittivity ε of the fluids at the probe tip by $\mathbf{Y} = k_g (\sigma + j\omega\varepsilon_0\varepsilon)$ (3.21). The geometry factor k_g reflects the ratio of the cross-sectional area of the sampled fluid volume and the length or distance between the electrodes. In this way, the introduction of different fluids at the probe tip will produce different measured admittance values allowing these substances to be distinguished. Note that a large area/length ratio is desired to produce large admittance values which are easier to detect by the electronics. There exist hence two possibilities to optimize the geometry. The probe tip can either be designed with a large area or the distance between the electrodes can be decreased. Nevertheless, there are limits for these arrangements. A larger probe tip (free electrodes) and thus a larger area would produce a higher disturbance in the flow which is undesired. Furthermore, a smaller distance between the electrodes can make the probe insensitive to given flow conditions, for instance air bubbles might not be detected due to dewetting problems at the probe tip. Therefore two probes were constructed. Probe "one" is more appropriate for a bubbly flow due to its arrow-type tip which can better pierce bubbles and its larger electrode distance. The probe "two"

was optimized for the investigation of a mixing process in a stirred tank which is better described in section 4.4.2. Evidently, other scaled up or down variations of the probe can be designed in order to adapt to other applications or constraints.

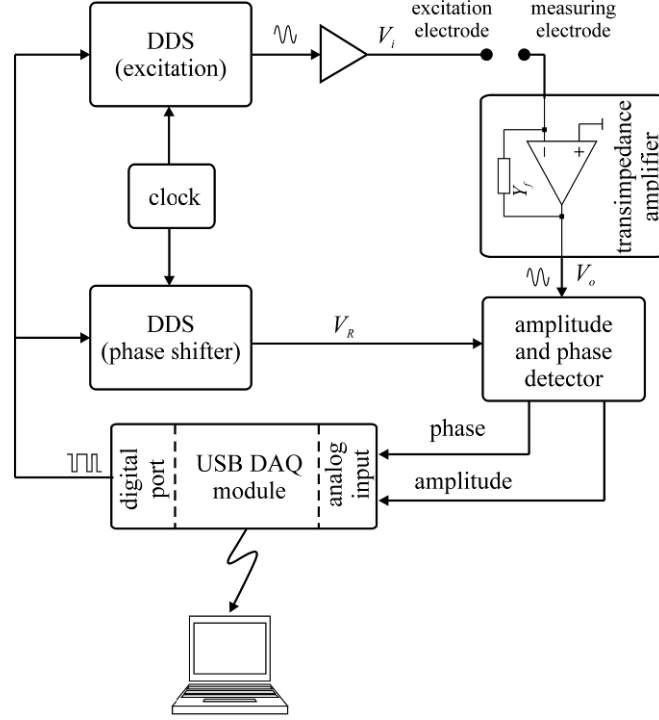


Figure 4.2: Block diagram of the electronic circuitry to measure the complex permittivity of a needle probe system.

4.2.2 Measuring electronics

A block diagram of the electronic circuitry can be seen in Figure 4.2. A direct digital synthesizer (DDS) generates the excitation sine wave voltage. Frequencies from 100 kHz up to 1 MHz can be generated and are user-selectable. The alternating excitation voltage V_i is supplied to the excitation electrode by means of a coaxial cable. The measuring electrode is connected to a transimpedance amplifier also by means of a coaxial cable. From section 3.3.1 it is known that the output voltage of the auto-balancing bridge is a measure of the admittance under test, here denominated Y_m , hence

$$V_o = V_i \cdot Y_m \cdot \frac{1}{Y_f}, \quad (4.1)$$

where \mathbf{Y}_f is the feedback admittance. The output voltage \mathbf{V}_o is then input to the amplitude and phase detector block. The integrated circuit (IC) AD8302 realizes the function of measuring amplitude and phase. This IC determines the amplitude ratio and the phase difference from \mathbf{V}_o and a reference signal \mathbf{V}_R . The AD8302 measures phase differences in two quadrants (e.g. from 0° to 180°) and achieves the best accuracy in the phase measurement only between phase differences of 20° and 160° (nominal accuracy 0.5°). Since the phase difference caused by the needle probe was expected to be as small as a few degrees for non-conducting substances, a phase shifter was required to allow the AD8302 to work with highest accuracy. The phase shifter was easily implemented by means of a second DDS, which generates a reference voltage \mathbf{V}_R with known amplitude and digitally programmable phase. Usually, a 90° phase delay was generated, thus placing the operation point of the AD8302 in the center of its measuring range. For this reason, both DDS generators are phase-synchronized by sharing the same clock source. A big advantage of a DDS-based phase shifter is the fact that the phase shift is independent of frequency. The two dc output signals of the AD8302, which carry the information on amplitude and phase difference, are fed into the analog-to-digital converter (ADC), 12 bit, 20 000 samples/s per channel, of the data acquisition (DAQ) module PMD-1208FS (Measurement and Computing Inc.). The DAQ module is connected to a PC through a USB port. The digital port of the DAQ module is used to program the DDS sine generators. Furthermore, a control and measurement software in the PC determines the frequency and phase lag of each DDS, controls the analog-to-digital conversion sequence and realizes the calculation of the admittance from the measured amplitude and phase values. A detailed description of the design and implementation of the system can be found in the diploma thesis Brückner (2005).

4.2.3 Complex permittivity measurement

The measuring admittance \mathbf{Y}_m represents the sum of the fluid admittance \mathbf{Y}_x and a residual admittance \mathbf{Y}_R (e.g. stray capacitance, resistance and inductance of cables, etc.) though being small, this residual admittance falsifies the measurement and a calibration routine is thus necessary. Equation (4.1) is modified to

$$\mathbf{V}_o = -\frac{\mathbf{Y}_x + \mathbf{Y}_R}{\mathbf{Y}_f} \mathbf{V}_i . \quad (4.2)$$

From (4.2), it can be shown that the fluid admittance \mathbf{Y}_x is linearly dependent on the measured output voltage \mathbf{V}_o in the form

$$\mathbf{Y}_x = \mathbf{A} + \mathbf{B} \cdot \mathbf{V}_o, \quad (4.3)$$

where \mathbf{A} and \mathbf{B} are proportionality factors. As mentioned in section 3.1.1, fluids are better characterized by their complex permittivity rather than their impedance or admittance. According to theory described there, the admittance of the probe and the complex permittivity of the fluid at probe's tip are directly proportional. In this way, from (4.3) and (3.11) one obtains

$$\epsilon_x = \mathbf{C} + \mathbf{D} \cdot \mathbf{V}_o. \quad (4.4)$$

Therefore, a two-point calibration is sufficient to determine the system variables \mathbf{C} and \mathbf{D} . For that, two known reference substances with known complex permittivity (ϵ_1 and ϵ_2) may be connected to the probe and \mathbf{V}_o measured for both conditions obtaining \mathbf{V}_{o1} and \mathbf{V}_{o2} . The values for system variables are then determined from

$$\mathbf{C} = \frac{\epsilon_2 \cdot \mathbf{V}_{o1} - \epsilon_1 \cdot \mathbf{V}_{o1}}{\mathbf{V}_{o1} - \mathbf{V}_{o2}}, \quad (4.5)$$

$$\mathbf{D} = \frac{\epsilon_2 - \epsilon_1}{\mathbf{V}_{o1} - \mathbf{V}_{o2}}. \quad (4.6)$$

With the help of the above formulae, it is now possible to calibrate a complex permittivity needle probe at two materials with known electrical properties, e.g. air and water. In the case, one is interested only to differentiate the phases or components of a fluid flow, e.g. gas phase detection in a bubbly flow, the calibration procedure is not anymore necessary, since the measured voltage \mathbf{V}_o already carries this information in its complex value. Each component or phase is associated to a point in the complex plane. Thus, this value can be evaluated directly to determine the phase/component indicator function (2.1) and derived parameters.

4.3 Measurement uncertainty

System outputs, i.e. amplitude and phase measurements, were evaluated for drift and random noise. A 100 k Ω resistor was connected to the needle probe electrodes and the outputs were monitored for one hour at maximum sampling rate of 20 kS/s. A one-

minute moving-average filter was used to reduce random noise for determination of the drift. System drift was defined as maximum deviation of the outputs over the period. The measured drift was 34.13 mV and 0.637° . Random noise was estimated as the standard deviation of the signals over a time equal to one minute. Measured random noise was 14.42 mV and 0.272° . Applying the uncertainty propagation rules (ISO 1995) in (4.4), one can estimate both the drift and random noise for the complex permittivity parameter:

$$U(\epsilon) = \mathbf{D} \cdot U(\mathbf{V}_o), \quad (4.7)$$

where $U(\epsilon)$ represents the uncertainty in the complex permittivity, $U(\mathbf{V}_o)$ the uncertainty in the measured output voltage and \mathbf{D} is defined in (4.4). Drift and random noise were then calculated from (4.7) by using typical calibration values for \mathbf{D} . Drift values were 0.4272 and 0.0023 $\mu\text{S}/\text{cm}$ for permittivity and conductivity, respectively. Furthermore, random noise value was 0.1810 for permittivity and 0.0009 $\mu\text{S}/\text{cm}$ for conductivity.

The system was also tested in measuring different liquids and air. The liquids were put in a metal cylinder of 10 cm in height, 10 cm in diameter and the probe was located in the center. First, the system was calibrated by measuring air (empty probe) and deionized water. The excitation frequency was 200 kHz and sampling frequency 20 kS/s. The measurements were carried out with both needle probe designs.

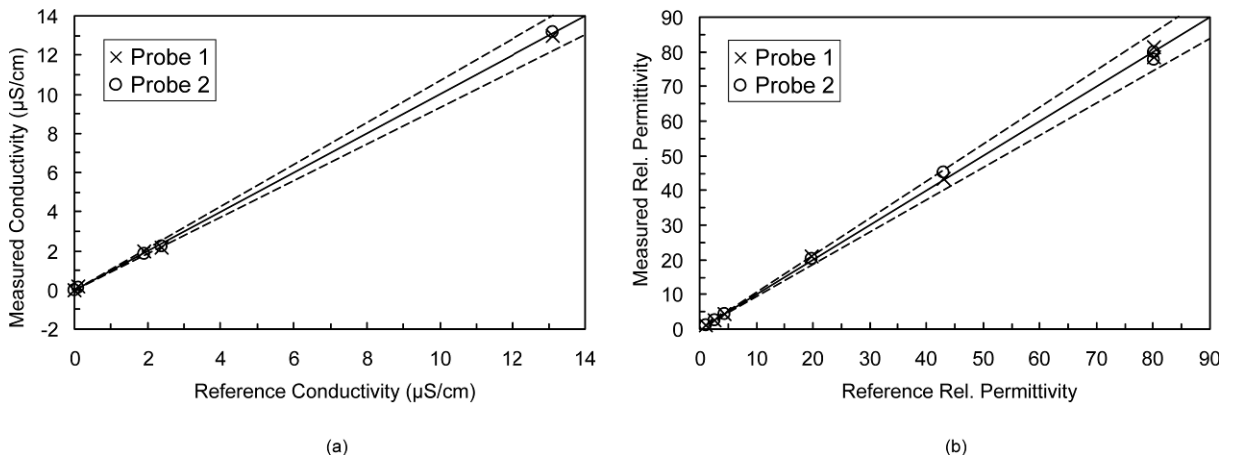


Figure 4.3: Results of conductivity (a) and permittivity (b) measurement by the needle probe compared with reference values. The dashed lines represent a deviation of 7% from the ideal line (—).

Table 4.1: Relative permittivity ε and electrical conductivity σ of different liquids and air used in the uncertainty evaluation of the needle probe system.

Substance	ε	σ ($\mu\text{S}/\text{cm}$)
Air	1.00	0.0
Silicone Oil	2.78	0.0
Diethyl Ether	4.27	0.0
Isopropanol	19.74	0.1
Glycol	40.56	1.5
Deionized Water	79.86	2.5
Water + Salt	79.86	13.1

Figure 4.3 show the results of measured properties (mean value of 10 measurements) compared with reference data. These figures show also a 7% deviation line (dashed). The relative permittivity reference was taken from Lide (2005) and calculated for the ambient temperature of the samples. Conductivity and temperature references of the samples were measured by the conductivity meter Cond 330i (WTW GmbH, Germany, 0.5% measurement uncertainty). The reference values are shown in Table 4.1.

The maximum relative deviation compared with the reference values was 7.0% for permittivity and 4.9% for conductivity, respectively. Both needle probe designs present similar results showing that the calibration routine fully compensates the different geometry factors (due to the different dimensions) of each probe.

4.4 Application to flow measurement

4.4.1 Three-phase flow

In order to examine the capability of the present system to be applied in the investigation of three-phase flows, it was employed to measure air and water bubbles flowing in gasoline. The system was calibrated by measuring air and deionized water. The excitation frequency was 200 kHz and sampling frequency was 20 kHz. The probe "one" (Figure 4.1b) was then located inside an acrylic glass column (rectangular cross-section, 20 mm \times 10 mm) filled with gasoline ($\varepsilon \approx 2$). The flow of bubbles was synchronously recorded with a high-speed video camera (MotionPro HS Series,

Redlake) operated at 1 000 fps with image size of 640×640 pixels, in order to evaluate the needle probe data.

First, air bubbles were generated at the bottom of the column. Figure 4.4a shows the temporal evolution of relative permittivity and conductivity registered by the needle probe for the measurement of a single air bubble (approximately 200 mm^3) as well as three single shot images of the ascending bubble. The relative permittivity value is lowered by the passage of the bubble, but the conductivity signal remains constant at a value near zero, as expected, since gasoline and air are non-conducting.

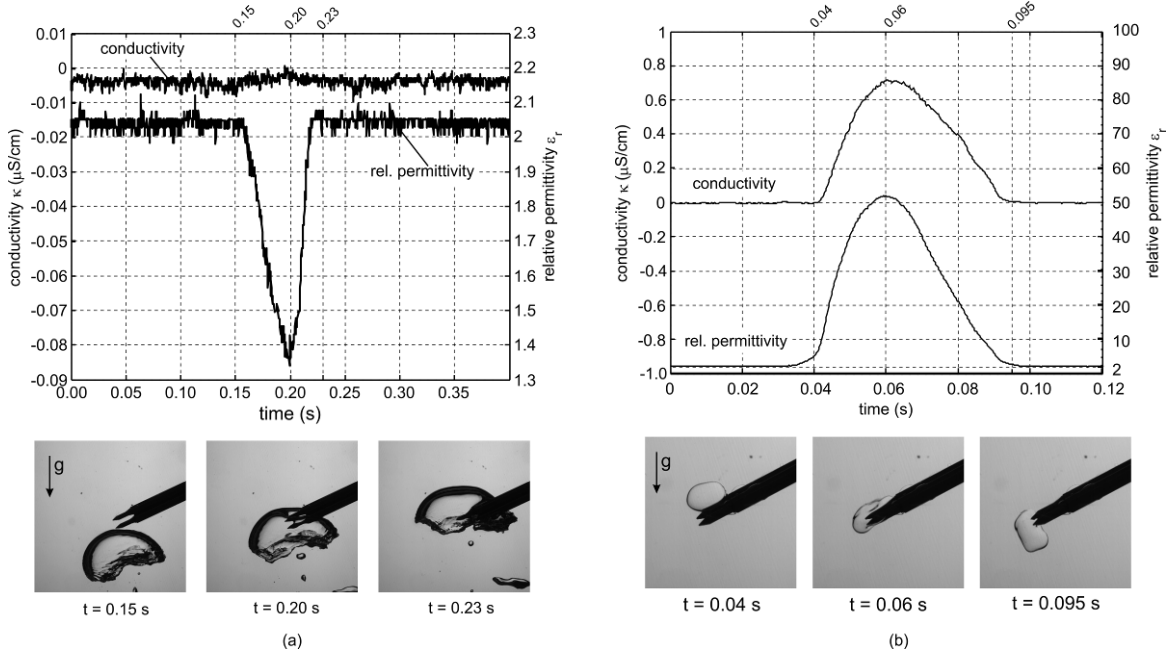


Figure 4.4: Temporal evolution of relative permittivity and conductivity signals for (a) an air bubble ascending in gasoline and (b) a water bubble descending in gasoline and their respectively video images; t indicates the time of the image and \mathbf{g} the gravity acceleration vector.

As a second experiment, water bubbles with conductivity of $2 \mu\text{S/cm}$ were dropped into the column filled with gasoline. Figure 4.4b shows the results. Again, three single shot images show the water bubble (approximately 100 mm^3) descending in gasoline and the diagram shows the temporal evolution of relative permittivity and conductivity. In this experiment both signals increase, since water is conductive and has a larger relative permittivity ($\epsilon \approx 80$) than gasoline ($\epsilon \approx 2$).

In a further experiment, a few air bubbles and then a few water bubbles ($\sigma = 2 \mu\text{S/cm}$) were sequentially generated in the vessel filled with gasoline. The detected signals are depicted in Figure 4.5. By the passage of the bubbles through the

needle probe tip, some spikes in the signals are produced depending on the fluid phase. In order to automatically distinguish which phase is momentarily in contact with the probe tip, the following procedure is proposed.

- A threshold in the conductivity signal σ_t can be used to decide between a conducting and a non-conducting phase. In Figure 4.5 a threshold value of $0.4 \mu\text{S}/\text{cm}$ was used, which represents 20% of the water conductivity. This way, the water phase can be recognized.
- If the conductivity is below σ_t , i.e. the phase is non-conducting, a second threshold in the relative permittivity signal ε_t can then discriminate between a non-conducting liquid and gas phase. In this example a threshold with the value of 1.8 was used corresponding to a level of 80% in between of the gasoline and air levels, as indicated in the figure.
- In this fashion, if $\varepsilon > \varepsilon_t$, the phase is identified as gasoline; otherwise if $\varepsilon < \varepsilon_t$, the phase at the probe tip is detected as air.

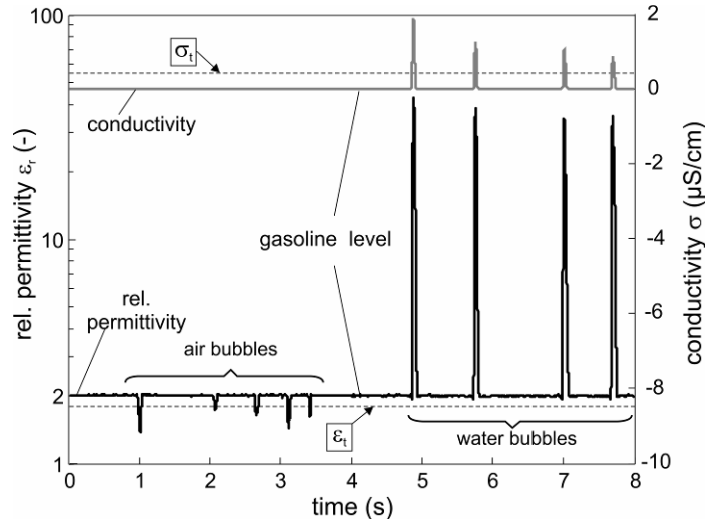


Figure 4.5: An example of the complex permittivity signals of a gasoline-water-air flow measured with the complex permittivity needle probe.

4.4.2 Two substances mixing experiment

A further application area of the impedance needle probe is the investigation of substance mixing in chemical reactors. Mixing of different density liquids occur in a variety of industrial applications, e.g. in blending of gasoline fractions, mixing of polymers and soft drinks production. A key experiment was conducted to investigate

the performance of the new probe, whereby the mixing process of water and isopropanol was measured with the probe "two" (Figure 4.1c).

First, a static calibration curve with defined concentrations was taken by mixing known volumes of isopropanol in water. The outputs were measured at 20 kfps and 10 values were averaged. Figure 4.6 depicts the results. The relative permittivity shows almost a linear dependence to the isopropanol concentration. In other hand the conductivity is strongly non-linear. Therefore, in the following analysis only the permittivity signals will be analyzed.

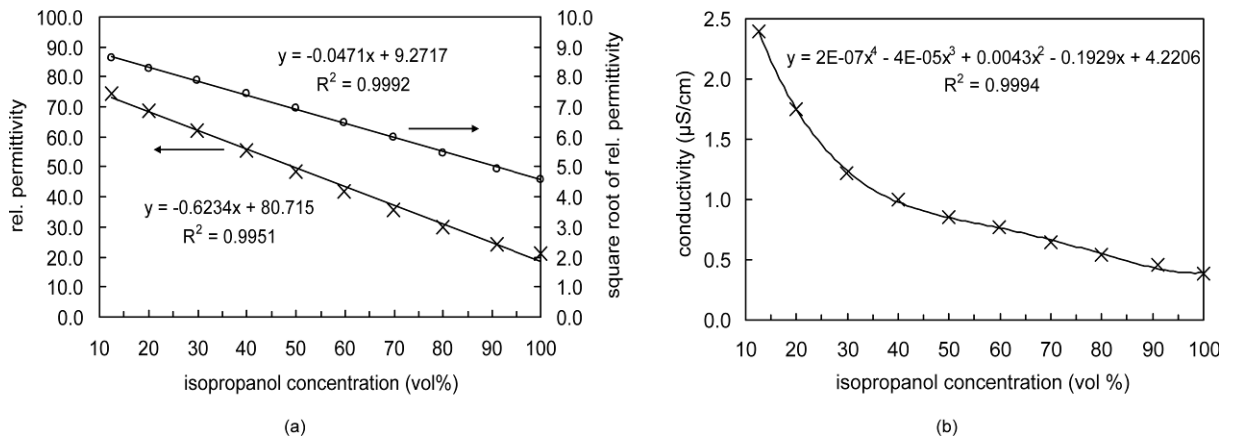


Figure 4.6: (a) Permittivity of isopropanol-water mixture for different isopropanol concentrations. Relative permittivity measurements (\times), square root of relative permittivity (\circ) and linear fit for both curves (lines). (b) Conductivity of isopropanol-water mixture for different isopropanol concentrations, (\times) denotes measurement points and line the polynomial fit.

There exist many theories to explain the permittivity behavior of a two substances mixture (Nelson *et al.* 1991). The Birchak formula (Birchak *et al.* 1974) can be well applied to describe the effective permittivity ε_m of an isopropanol-water mixture. It has the form

$$\sqrt{\varepsilon_m} = c_i \cdot \sqrt{\varepsilon_i} + (1 - c_i) \sqrt{\varepsilon_w}, \quad (4.8)$$

where c_i is the isopropanol concentration, ε_i and ε_w are the relative permittivities of isopropanol and water, respectively. Resolving (4.8) for c_i yields

$$c_i = \frac{\sqrt{\varepsilon_m} - \sqrt{\varepsilon_w}}{\sqrt{\varepsilon_i} - \sqrt{\varepsilon_w}}. \quad (4.9)$$

Since ε_i and ε_w are constants, the isopropanol concentration is directly proportional to the square root of the mixture permittivity. This was also experimentally verified, as can be seen in Figure 4.6. As a result, the isopropanol concentration can be determined by measuring the relative permittivity of the mixture and solving (4.9).

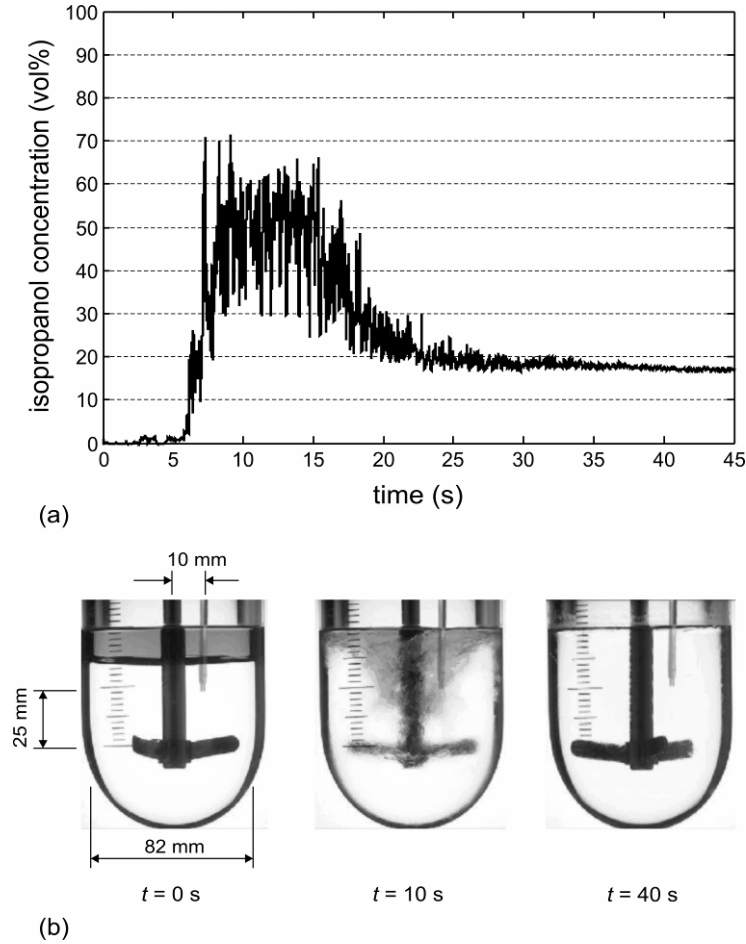


Figure 4.7: (a) Isopropanol concentration measured with the needle probe, and (b) single shot images of mixing experiment from the camcorder.

The mixing experiment was carried out in a laboratory scale Büchi Ecoclave 1.6 liter tank. The reactor inner diameter was $d = 82$ mm. The reactor was mechanically agitated by the Pfaudler impeller, which was connected to a dc motor. The needle probe "two" was placed 25 mm above the impeller and in a radial position 10 mm from tank's center. The excitation frequency was set to 200 kHz and the sampling frequency to 20 kHz. The needle probe was firstly calibrated by measuring air and water. The mixing experiment was also monitored by a digital camcorder Panasonic NV-GS 400 at 50 fps. The used liquids were mutually miscible with densities of

998 kg/m³ for the water and 780 kg/m³ for the isopropanol. Since both substances are transparent, the isopropanol was colored by a blue ink, in order to provide contrast for the video visualization. The total liquid level was $h = 82$ mm, chosen to be close to the commonly found in the mixing practice ratio of $d/h = 1$. A two layer initial condition was obtained by first pouring 345 ml water and then 75 ml isopropanol into the tank. The mixing process was started by rotating the impeller at 187 rpm. The temporal evaluation of the isopropanol concentration determined by the needle probe, which is based on permittivity measurements and calculated via (4.9), are shown in Figure 4.7, as well as three single shot images from the camcorder.

At $t = 0$ the impeller started rotating. After five seconds the isopropanol component surface reached the needle probe thus rapidly increasing the measured concentration. A maximum concentration of about 70% is obtained between $t = 5$ s and $t = 15$ s. From $t = 15$ s the isopropanol concentration started decreasing. Complete mixing was reached 40 seconds after the impeller rotation started. The final isopropanol concentration was measured to be 16.5% (mean value of last five seconds), very close to the theoretical value 17.8% calculated from the initial component volume ratio (i.e. $c_{\text{final}} = 75 \text{ ml} / 420 \text{ ml}$). The camcorder images of Figure 4.7 also illustrate the mixing process: $t = 0$ s initial stratified condition; $t = 10$ s the two components were brought into motion by the rotating impeller, the interfacial area of both components can be well identified; and $t = 40$ s both substances are completely mixed.

The time-resolved local concentration measurement by the needle probe can reveal some details about the mixing behavior of two miscible liquids with different densities. For example, the fluctuations in the concentration values suggest that the interfacial area of both components was oscillating over the measurement point.

4.5 Conclusions

The evaluation of the sensor shows good linearity, reproducibility and adequate accuracy when compared with reference values. For the first time the local complex permittivity measurements of a three-phase bubbly flow have been presented. The sensor is able to differentiate each phase by evaluating both relative permittivity and conductivity signals.

Furthermore, the good accuracy in complex permittivity measurements enables the sensor not only to be employed as phase discriminator but also to measure concentration of a two-component mixing.

The probe was also evaluated to measure local concentration of a mixing process on a laboratory scale stirred tank. The detailed analysis of such measurements can reveal more details about the mixing process and should be further investigated.

Finally, all these characteristics combined with the high-speed measurement system feature make the needle probe system a suitable new tool to investigate dynamic phenomena in multiphase flow.

5 Capacitance wire-mesh sensor

Wire-mesh sensors are able to image multiphase flows with high spatial and temporal resolution. A novel wire-mesh sensor based on capacitance (permittivity) measurements is presented in this chapter. The developed sensor can be used to measure transient phase fraction distributions in a flow cross section, such as in a pipe or another vessel by discriminating fluids with different permittivity values.

5.1 Introduction

Several measuring techniques for the investigation of flow phenomena have been proposed and investigated in the past (see section 2.2). Especially the use of tomography visualization techniques are of great interest since these are non-invasive and enable the visualization of phase fractions distributions in multiphase flows. However, currently all of the existing technical solutions have considerable drawbacks. Thus, x-ray, γ -ray, PET and MRI scanners yet do not have sufficient time resolution either due to the requirement for rotating parts in the scanners or limits in radiation power. Electrical tomography techniques (e.g. ERT, ECT) achieve high time resolution but have intrinsically low spatial resolution due to the applied soft fields. Optical and ultrasound tomography are only suited for flows with low void fraction.

The conductivity wire-mesh sensor, which was first proposed for high-speed liquid flow measurements by Prasser *et al.* (1998), is a hybrid solution in between intrusive probe and tomographic cross-sectional imaging (section 2.2.3). Void fraction and bubble size measurements with temporal resolution of up to 10 000 frames per second (fps) and spatial resolution of up to 2 mm have been achieved (Prasser *et al.* 2002b). Nevertheless, current wire-mesh systems are only suitable to investigate flows where one phase is a conductive medium, typically with electrical conductivity of at least

0.5 $\mu\text{S}/\text{cm}$. Therefore, wire-mesh sensors have almost exclusively been used for the investigation of air-water or steam-water systems.

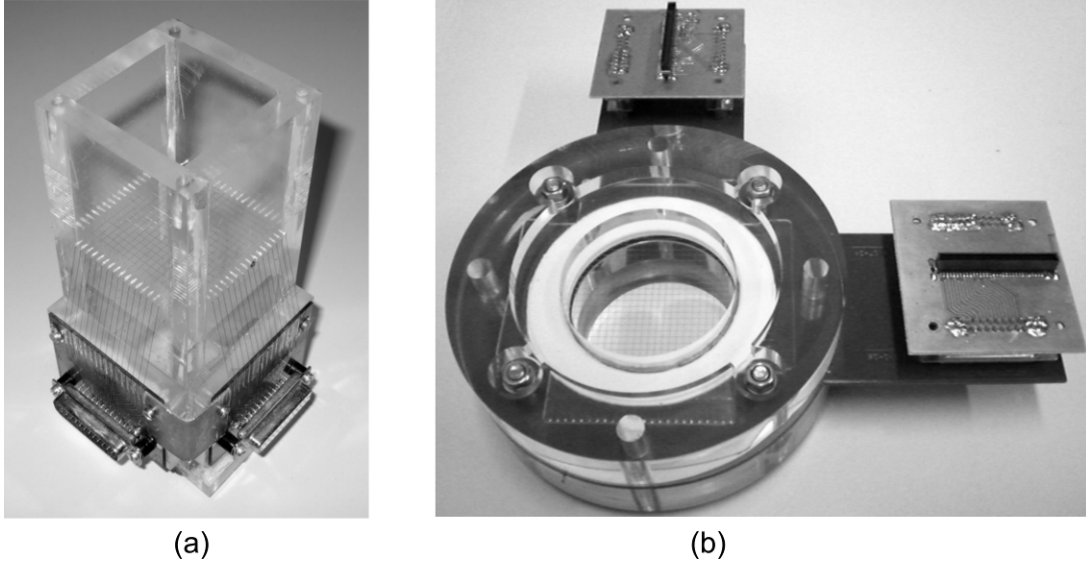


Figure 5.1: Photo of the experimental wire-mesh sensors used in this work. (a) Laboratory sensor with 16×16 configuration and (b) 24×24 wire-mesh sensor for pipe flow investigation.

In the chemical processing industry the occurrence of non-conducting fluids such as oil or organic liquids are common, for instance in distillation columns or in pipelines. In those applications the measurements with current wire-mesh sensor would fail. However, this limitation can be overcome by performing permittivity (or capacitance) measurements instead of conductivity measurements (Da Silva *et al.* 2007b). In this way, a great number of new application fields of wire-mesh sensors can be explored.

This chapter presents design, evaluation and application of a novel wire-mesh sensor system based on permittivity (capacitance) measurements which has been applied to investigate multiphase flows involving non-conducting fluids. The evaluation of sensor includes simulation analysis of electrical field distribution (section 5.3) and experimental tests regarding metrological quantities (section 5.4). Some flow applications of the sensor are described in section 5.5.

5.2 System description

5.2.1 Sensor and measuring electronics

The prototype sensor used for experimental verification of the capacitance measurement technique has the same design as a conductivity wire-mesh sensor

(Figure 5.1a). It consists of two planes of 16 stainless steel wires of 0.12 mm diameter, 3.12 mm separation for wires of same plane, and 1.5 mm axial plane distance. The wires are mounted in a rectangular acrylic frame that itself is part of a rectangular flow channel. A 24×24 wire-mesh sensor was built up and applied for the investigation of a pipe flow (see section 5.5.1). It consists of two planes of 24 stainless steel wires of 0.12 mm diameter evenly distributed over the 67 mm diameter (Figure 5.1b), and 1.5 mm axial plane separation. The sensor was constructed using printed-circuit board (PCB) as described in Schleicher *et al.* (2007). The sensor is framed in an acrylic flange, which allows it to be mounted in a flow loop.

The operating principle of the electronics is similar to the conductivity wire-mesh sensor (Prasser *et al.* 1998). However, while the conductivity wire-mesh sensor is excited by bipolar voltage pulses and currents are measured with a dc measuring scheme, the capacitance wire-mesh sensor utilizes an appropriate ac excitation and measuring scheme. Hence, a sinusoidally alternating voltage is applied for excitation and the receiver circuit must encompass a demodulation scheme. Figure 5.2 depicts the block diagram of the electronic design for a simplified 4×4 sensor configuration.

The excitation voltage is generated by means of a direct digital synthesizer (DDS) circuit with selectable frequency in the range from 0.1 to 10 MHz. This signal is then time-multiplexed to each of the excitation electrodes by means of a set of analog switches. In order to create a low impedance path, the outputs of the switches are buffered by opamps. A set of auto-balancing bridge circuits (OPA656 based) converts the currents flowing from transmitter towards receiver electrodes into proportional voltages. Furthermore, these sine wave voltages are demodulated using logarithmic detectors (AD8307), in order to convert them into dc proportional voltages, which are in turn digitized by the ADCs. A microcontroller controls the multiplexer, programs the DDS and controls the analog-to-digital conversion timing. Digitized data are sent to a computer, where they are processed and visualized.

To realize an independent local phase fraction measurement in each crossing point, i.e. to suppress the crosstalk between the individual sub-regions, the following excitation scheme is employed (Figure 5.3). The transmitter electrodes are activated consecutively, while keeping all other transmitter electrodes at ground potential. All currents flowing from transmitter to receiver electrodes at the other wire plane are measured in parallel as described above. Since the receiver electrodes are also at ground potential by the opamp's virtual ground, the electrical field is concentrated along the active transmitter wire and the current measured at one receiver wire is

only proportional to the capacitance (permittivity) of the surrounding flow phase at the crossing point. This fact was detailed analyzed and confirmed by electrical field simulations (see section 5.3).

Two different electronics have been designed, implemented and tested (Wollrab 2006, Thiele 2007). The recent electronics can operate sensors of up to 64×64 wire configuration and achieves up to 7 000 fps for a 32×32 sensor.

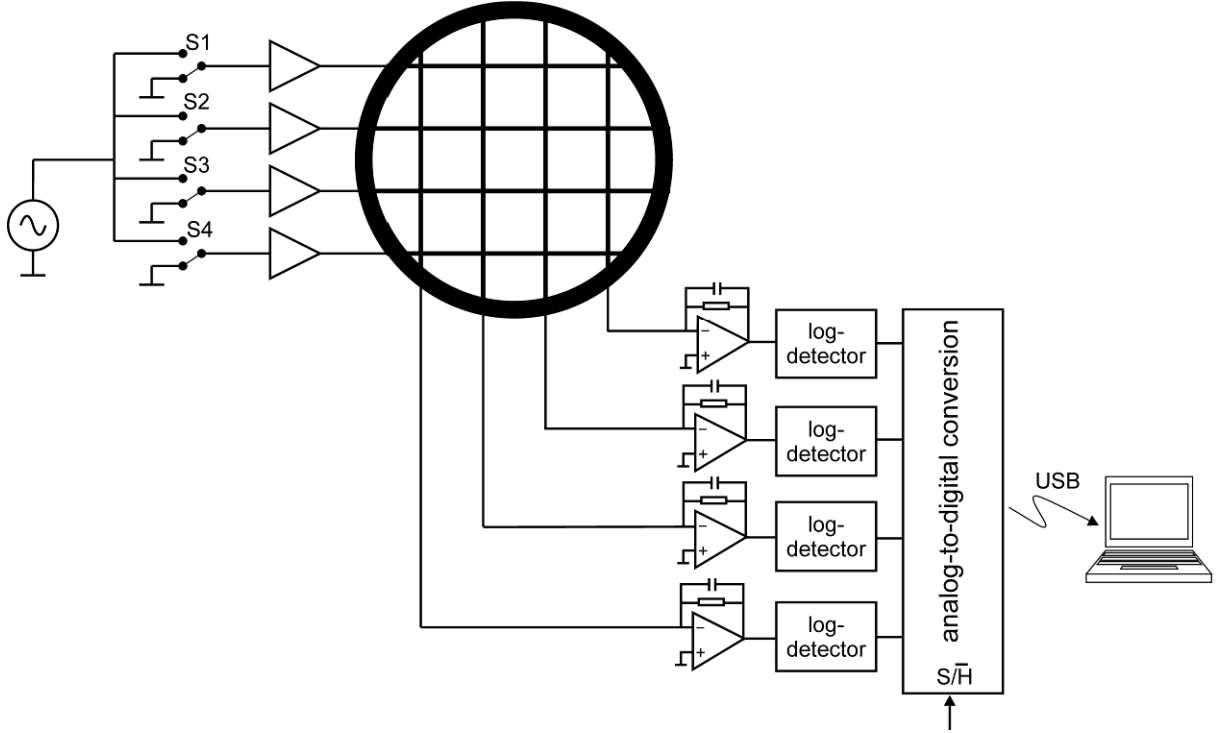


Figure 5.2: Schematic diagram of a simplified 4×4 wire-mesh sensor electronics.

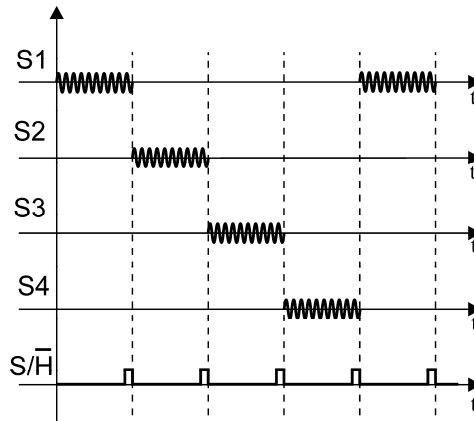


Figure 5.3: Excitation scheme of the wire-mesh sensor electronics.

5.2.2 Permittivity measurement

Since the input quantity for each crossing point in the capacitance wire-mesh sensor is expected to be composed by a single unknown capacitor, the auto-balancing bridge method was optimized for capacitance measurement only. Figure 5.4 shows an equivalent circuit for one crossing point, where V_i is the sine wave excitation voltage, C_x represents the crossing point capacitance to be measured, and C_f and R_f represent the feedback network. C_{s1} and C_{s2} are also shown in the figure and they represent the stray capacitances to ground generated for instance by the cables or other grounded electrodes. However, they have no influence in the circuit as already discussed in section 3.3.1.

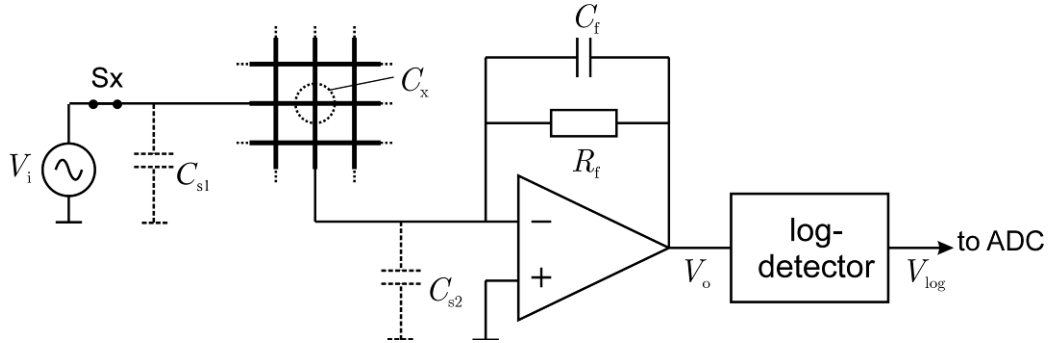


Figure 5.4: Capacitance measuring equivalent circuit for one crossing point.

Assuming that the opamp is ideal and that the internal resistance of the analog switch is zero, the output voltage V_o is determined by

$$V_o = -V_i \left(\frac{j\omega C_x R_f}{1 + j\omega C_f R_f} \right), \quad (5.1)$$

where $\omega = 2\pi f$ is the angular frequency of the excitation voltage, which is a simplified version of (3.30). In fact, the analog switch has an on-resistance of a few ohms which only marginally influences the circuit. If the operating frequency is chosen so that $\omega R_f C_f \gg 1$, (5.1) is simplified to

$$V_o = -V_i \cdot \frac{C_x}{C_f}, \quad (5.2)$$

meaning that the circuit is capacitance-dominant. In this situation the phase lag between input and output voltages is exactly 180° which is given by the minus signal in (5.2) since the circuit is in an inverting configuration. Hence, it can be stated that by measuring only the amplitude of the complex quantity V_o , i.e. V_o , it is possible to

determine the capacitance value of the fluid phase at the crossing point. For the feedback network $R_f = 1 \text{ M}\Omega$ and $C_f = 1 \text{ pF}$ were employed, and a typical excitation frequency of 5 MHz was chosen. In this way, $\omega R_f C_f = 31$ and (5.2) is a good approximation. Nevertheless, (5.1) may also be used if more accurate values are needed.

The sinusoidal alternating voltage V_o has to be demodulated so that it can be digitized, i.e. the ac signal has to be converted into a proportional dc one. Since a high signal dynamics from measurements on different substances are expected, a logarithmic detector scheme for the demodulation of the ac signal was chosen. Even very small changes in the capacitance C_x (and consequently in V_o) can be measured by maintaining a fast response time. The log-detector AD8307 output is in the form

$$V_{\log} = V_a \cdot \ln\left(\frac{V_o}{V_b}\right), \quad (5.3)$$

where V_a and V_b are constants of the integrated circuit. Taking (5.2) into (5.3) and remembering (3.22) that C_x is directly proportional to permittivity ε_x of the substance in the crossing point, it results in

$$V_{\log} = a \cdot \ln(\varepsilon_x) + b, \quad (5.4)$$

where a and b are constants that encompass the geometry factor k_g of a crossing point, R_f and C_f , the log-detector constants, f the measuring frequency and V_i the input voltage.

The acquired voltages V_{\log} for all crossing points are saved in an $N_x \times N_y \times N_t$ data matrix in computer memory, where N_x and N_y denote the number of sender and receiver electrodes and N_t the number of acquired time steps. The data are related to the permittivity distribution over the cross section via (5.4), but evidently this raw data need further processing to discriminate phases or determine absolute capacitance values. Due to differences in the electrical characteristics of the individual components, for instance resistor tolerances, opamp gains etc, there is a considerable intrinsic variance in the measured values of each crossing point. In order to compensate this variance, a calibration routine is required, which is described as follows.

First, the sensor is measured with a substance of low permittivity ε_L covering the whole sensor giving a reference data matrix

$$V^L(i, j) = \frac{1}{N_t} \sum_{k=0}^{N_t-1} V_{\log}(i, j, k), \quad (5.5)$$

which is an average of the raw data over a sufficient temporal range. Here, i and j denote the wire indices and k the temporal sampling point index.

The procedure is then repeated with the entire cross section of the sensor covered with another substance having a higher permittivity ε_H , which gives another reference data matrix denoted by V^H . In this fashion, applying equation (5.4) for both calibration data matrixes V^H and V^L it is possible to calculate the constants of (5.4) for every crossing point as

$$a(i, j) = \frac{V^H(i, j) - V^L(i, j)}{\ln(\varepsilon_H) - \ln(\varepsilon_L)} \quad (5.6)$$

$$b(i, j) = \frac{V^L(i, j) \ln(\varepsilon_H) - V^H(i, j) \ln(\varepsilon_L)}{\ln(\varepsilon_H) - \ln(\varepsilon_L)}. \quad (5.7)$$

Finally, the permittivity distribution over the cross-section can be determined by inverting (5.4) and applying it for every crossing point, thus

$$\varepsilon(i, j, k) = \exp\left(\frac{V_{\log}(i, j, k) - b(i, j)}{a(i, j)}\right). \quad (5.8)$$

In the case that the lower permittivity reference substance is air which has $\varepsilon = 1$, (5.8) is simplified to

$$\varepsilon(i, j, k) = \exp\left(\frac{V_{\log}(i, j, k) - V^L}{V^H - V^L} \ln(\varepsilon_H)\right). \quad (5.9)$$

For the determination of the local phase fraction distribution $\alpha(i, j, k)$, a linear relationship between the measured permittivity and the phase fraction is assumed

$$\alpha(i, j, k) = \frac{\varepsilon_H(i, j) - \varepsilon(i, j, k)}{\varepsilon_H(i, j) - \varepsilon_L(i, j)}. \quad (5.10)$$

The assumption of a linear dependence between the local phase fraction level and the crossing point permittivity is obviously a simplification. It basically models the crossing points as a parallel plate capacitor with a homogenous phase distribution between capacitor's plates. An analogous assumption has been successfully employed for conductivity wire-mesh sensors (Prasser *et al.* 1998) and for ECT systems

(McKeen and Pugsley 2002). In the case of complex multiphase flows, more elaborated calibration relationships may be necessary, for instance encompassing models for the effective permittivity of mixtures. This way, (5.10) can be understood as first-order approximation.

Further data processing on the cross-sectional phase fraction distributions $\alpha(i, j, k)$ may then be performed to identify single bubbles or determine characteristic bubble or phase boundary parameters. Such algorithms have been successfully used for the conductivity wire-mesh sensor and are described in Manera *et al.* (2006), Prasser *et al.* (2001) and Richter *et al.* (2002).

5.3 Numerical field simulation

5.3.1 Model description and voltage distribution

The commercial software Comsol Multiphysics version 3.2 (Comsol 2008) was used to numerically predict the electrical field distribution within a wire-mesh sensor. This software package is based on finite element method (FEM) to solve partial differential equation (PDE) problems.

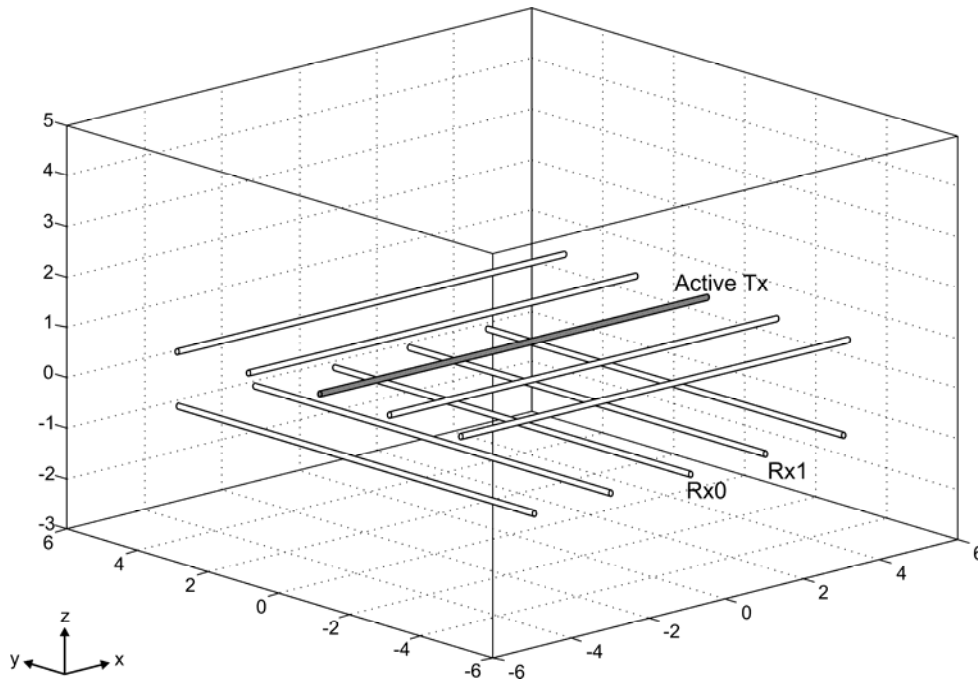


Figure 5.5: Geometry model of the simulated setup. The wire diameter is 0.1 mm, the distance between parallel wires 2 mm, and the axial separation between the wire planes 1.5 mm. The simulation domain was defined by a cuboid with volume of $6 \times 6 \times 8 \text{ mm}^3$.

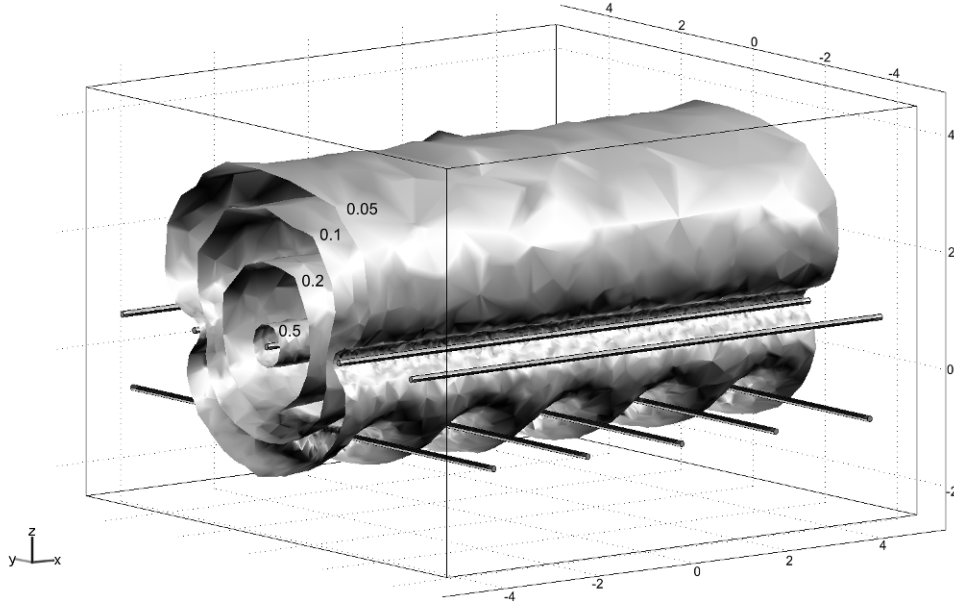


Figure 5.6: Voltage distribution for the simulated sensor as described in Figure 5.5. The value of each isosurface (in volts) is indicated in the figure.

A simplified 5×5 wire-mesh sensor geometry was modeled in three-dimensions, as depicted in Figure 5.5. Since the sensor dimensions are much smaller than the wavelength of the electrical fields employed, the wire-mesh sensor can be considered as an electrostatic field problem. Thus, the voltage V within the sensor can be calculated by solving the Poisson's equation in the form (see Appendix B.1, compare with (B.17))

$$\nabla(\varepsilon_0 \varepsilon(\mathbf{r}) \nabla V(\mathbf{r})) = 0, \quad (5.11)$$

assuming the free charge density ρ in the material is zero, where \mathbf{r} is position vector, ε_0 and ε are permittivity of vacuum and relative permittivity, respectively. To complete the model, the following boundary conditions were used. The voltage of the active transmitter wire, denoted by Tx, is set to +1 V while all other wires are on ground potential. Concerning the simulation domain (cuboid), the four lateral faces are set to a symmetry interface, satisfying $\mathbf{n} \cdot \mathbf{D} = 0$ (the normal component of the electric displacement equals zero); top and bottom faces are set to ground potential.

A grid composed of approximately 200 000 tetrahedral elements was generated and the PDE problem was solved using an algebraic-multigrid solver. The simulation took about 60 s to converge (normalized residual error less than 10^{-7}) in a Pentium III 1.7 GHz, 1 GB RAM computer. Figure 5.6 shows the obtained voltage distribution.

The isosurfaces are concentric cylinders close to the emitter wire, as for a conventional line charge, whereas approaching the other grounded emitter wires they get distorted.

5.3.2 Crossing point capacitance

To qualitatively evaluate the field distribution of a wire-mesh sensor, a perturbation approach was employed. A perturbation is placed within the simulation volume and its impact on the capacitance of a crossing point is analyzed. The simulated capacitance of a crossing point C_{sim} between the active transmitter wire and a given receiver wire is calculated by integrating the induced surface charge density ρ over the wire boundaries Γ

$$C_{\text{sim}} = \frac{1}{V} \int_{\Gamma} \rho(\Gamma) \cdot d\Gamma . \quad (5.12)$$

This integral is implemented as post-processing option in the Comsol software.

The crossing point capacitance for perturbations with different sizes was evaluated. For this purpose, a rectangular block of 1.4 mm height (touching the wires) and with sizes of 0.5, 1, 2 and 4 mm was placed at the origin of simulation domain and consequently at the middle of the central crossing point (Figure 5.7a). The perturbation permittivity was varied in the range $\varepsilon_p = 1$ to 80, while the simulation domain permittivity was kept constant with value $\varepsilon_d = 80$. Figure 5.7b displays the obtained capacitance values. The size of the block was normalized by the wire distance d_w (2 mm). The unperturbed crossing point capacitance ($\varepsilon_d = 80$) was found to be 0.9573 pF while the empty sensor was 11.97 fF ($\varepsilon_d = 1$), i.e. exactly 80 times smaller, as expected.

From Figure 5.7, it is evident that the capacitance values show linear dependence on the perturbation permittivity ε_p . In this test, a crossing point may be described as a capacitor having two dielectrics in parallel between its electrodes. The resulting capacitance is given by the parallel circuit of the individual capacitances of each dielectric, i.e. by the addition of each component. Thus, the resulting capacitance is linearly dependent on each individual capacitance and consequently on each permittivity value. Of course, the smaller the size of a perturbation, the smaller is the induced change in the capacitance. For the perturbation of size $2 \cdot d_w$, the crossing point capacitance lowers to the level of an empty sensor capacitance value. Hence,

this suggests that the measurement volume of a crossing point may be larger than a cube with size d_w centered at the crossing point, as accepted for the conductivity wire-mesh sensor (Richter *et al.* 2002).

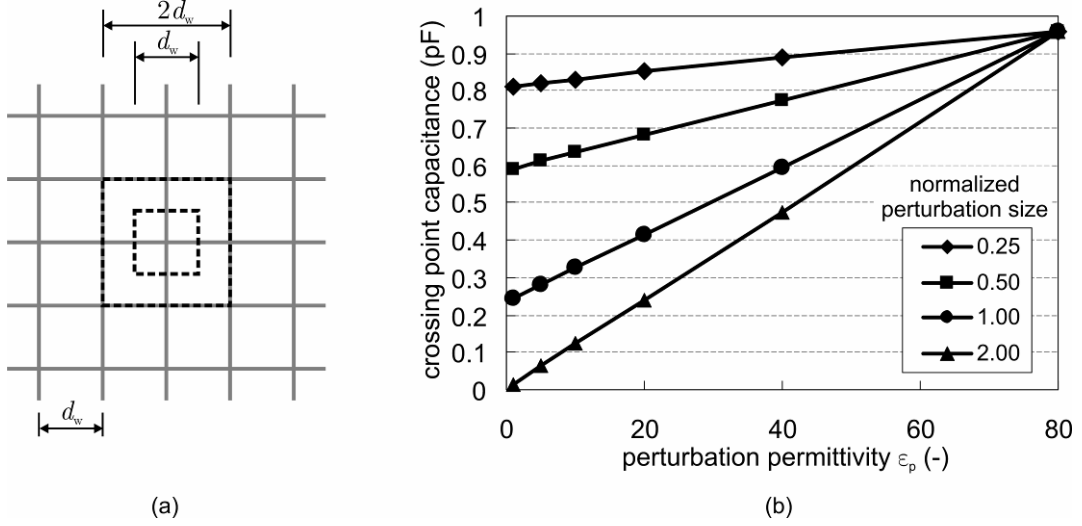


Figure 5.7: (a) Simulation arrangement for the investigation of the perturbation influence on the capacitance values. Two blocks are exemplary shown in the figure. (b) Capacitance values for four different perturbations sizes in a medium with $\epsilon_d = 80$. The block sizes were normalized by the wire distance d_w .

5.3.3 Spatial sensitivity

For a closer examination of the measurement volume of a crossing point, the following test was carried out. A small block perturbation of side $0.25 \cdot d_w$ and 1.4 mm height (again touching the wires) was moved from the origin of simulation domain along the x- and y-axis. To quantify the sensitivity, a similar approach proposed by Lucas *et al.* (1999) was applied. The change in the capacitance ΔC due to the presence of the perturbation was used to define the spatial sensitivity ψ as

$$\psi = \frac{\Delta C}{(\Delta C)_{\max}}, \quad (5.13)$$

where $(\Delta C)_{\max}$ is the maximum ΔC , which occurred for the perturbation located at the origin. The spatial sensitivity for the central receiver wire, Rx0, and a neighboring one, Rx1, were computed for 10 perturbation positions in the x-direction. Furthermore, the spatial sensitivity for Rx0 in the y-direction was determined for seven perturbation positions.

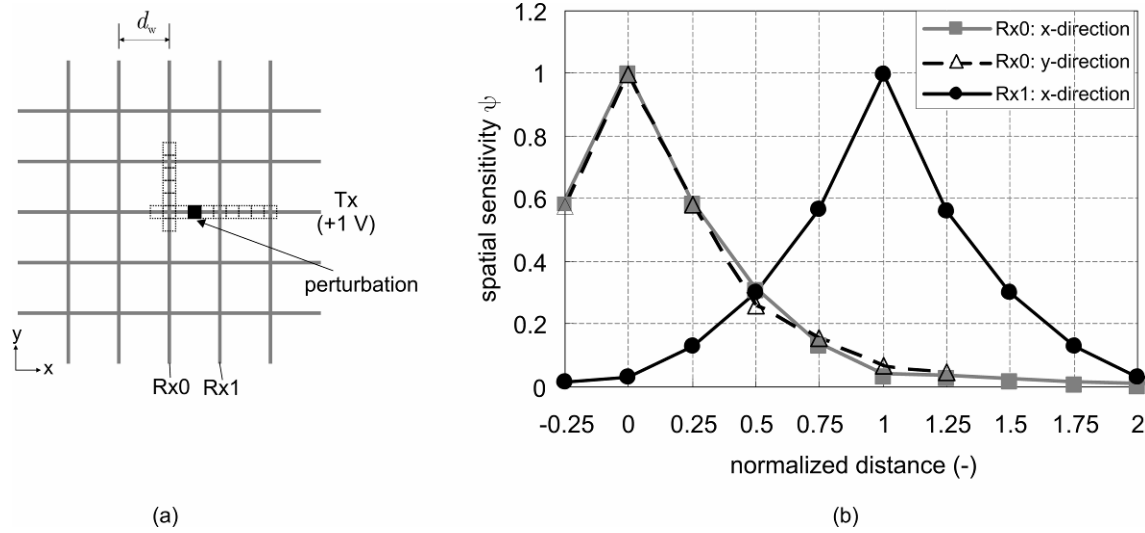


Figure 5.8: (a) Simulation setup for the determination of the measurement volume of a crossing point. (b) Spatial sensitivity distribution of the wire-mesh sensor in x- and y-directions. Symbols represent simulated conditions.

Figure 5.8 illustrates the simulation setup and shows the obtained spatial sensitivities. All three responses show similar behavior in which the sensitivity starts at a maximum and decays to zero with an exponential shape. The sensitivities determined for Rx0 in x- and y-axis are almost identical. From this, it can be concluded that the measurement volume of crossing point is axial-symmetric in relation to the z-axis. Comparing the sensitivity responses for the wires Rx0 and Rx1, it can be seen that the both spatial sensitivities have also an almost identical response but are spatially displaced by the value $1 \cdot d_w$. Although the spatial sensitivity reaches values near zero only at distances of approximately $1 \cdot d_w$ far apart of the wire, the assumption that the measurement volume has a cubic shape with side of $0.5 \cdot d_w$ (Richter *et al.* 2002) is still a good approximation and will be used in the next sections of this chapter.

A similar analysis as described above was performed to determine the sensitivity in the axial direction. A block perturbation of side $1 \cdot d_w$ and high of 0.5 mm was moved in the z-direction in 10 positions and the spatial sensitivity calculated. Figure 5.9 depicts the setup as well as the resulting spatial sensitivity. The sensitivity presents a flat response in between the wires, while it abruptly lowers to values near null for positions outside the volume between the wires. The response is symmetrical to the x-y-plane. It follows that the measurement volume is confined to the space between the wire planes.

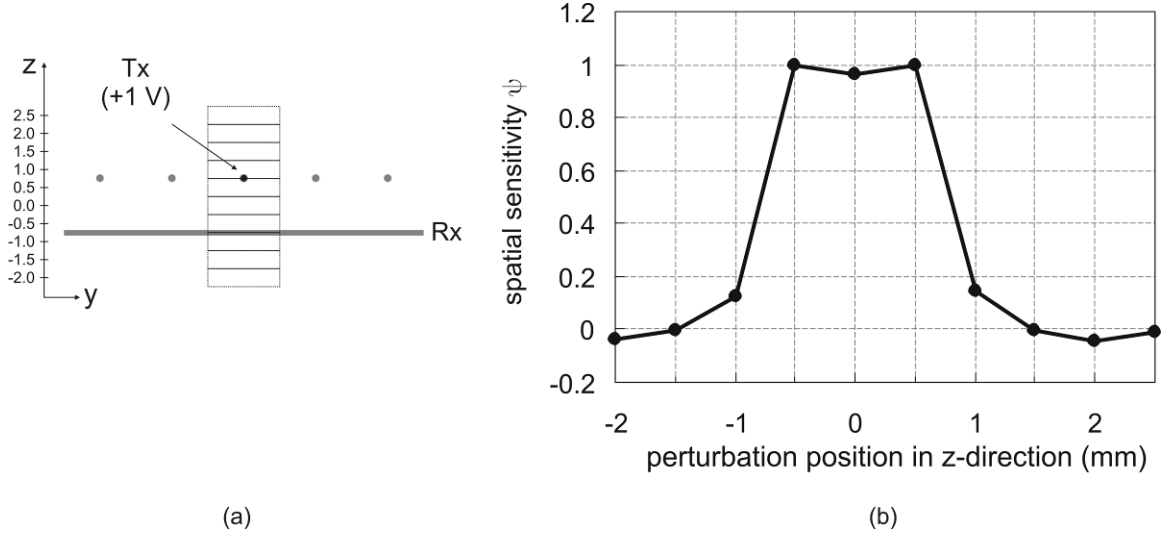


Figure 5.9: (a) Simulation arrangement for the determination of the sensitivity in z-direction. (b) Spatial sensitivity distribution of the wire-mesh sensor in z-direction. Symbols represent simulated conditions.

The simulations presented were repeated for slightly modified wire-mesh sensor dimensions, showing similar results for the voltage distribution and sensitivity analysis when compared with normalized dimensions. The capacitances of the empty sensor for all simulated cases are shown in Table 5.1.

Table 5.1: Crossing point capacitances (in Femtofarad) for a few simulated wire-mesh sensor geometries and empty sensor ($\varepsilon = 1$), where d_w is the distance between wires in a plane and d_z is the axial distance of the two wire planes.

d_w (mm) \ d_z (mm)	2.0	2.5	3.0
1.5	11.97	16.11	20.12
2.0	9.43	13.44	16.83
2.5	7.87	11.32	14.42

5.4 System evaluation

In this section, the experimental system performance evaluation is described. The two different measuring systems developed to operate wire-mesh sensors differed only in the analog-to-digital conversion scheme and consequently in the maximal achievable frame rate as well as in the number of transmitter-receiver pairs. In the following evaluation, a 16×16 prototype sensor was used. The results obtained are similar to the 64×64 prototype.

5.4.1 Measurement uncertainty

The novel wire-mesh sensor was firstly investigated regarding its accuracy and ability of distinguishing different substances. For this purpose, the wire-mesh sensor was entirely covered by some selected substances and 10 frames at the maximum sampling frequency were recorded and averaged in order to suppress random noise. The excitation frequency was set to 5 MHz and the input voltage amplitude to 3 V_{pp}. The calibration routine as described in section 5.2.2 was slightly modified. Instead of using a two-point calibration, a linear least-square regression of (5.4) for every crossing point was performed. That means, that (5.6) and (5.7) were replaced for their least-squares versions. Table 5.2 shows the selected substances and their reference permittivity, as well as the mean value of all crossing points

$$\bar{\varepsilon} = \frac{1}{256} \sum_{i=1}^{16} \sum_{j=1}^{16} \varepsilon(i, j), \quad (5.14)$$

the relative deviation from the mean value for each substance

$$\delta = \frac{\bar{\varepsilon} - \varepsilon^{\text{ref}}}{\varepsilon^{\text{ref}}}, \quad (5.15)$$

and the maximal deviation from the mean value

$$\Delta\varepsilon = \text{MAX}_{\forall i, \forall j} \left(\left| \frac{\bar{\varepsilon} - \varepsilon(i, j)}{\bar{\varepsilon}} \right| \right), \quad (5.16)$$

where $\varepsilon(i, j)$ represents the measured permittivity distribution for each substance. Mean and maximal deviations between the measured and expected values were found to be less than 10%.

In order to investigate the individual crossing points, the measured voltage for all crossing points $V_{\log}(i, j)$ were plotted in dependence on the permittivity for the measured substances (Figure 5.10a). From that, the linear dependence of V_{\log} over the logarithm of ε becomes evident, as predicted by (5.4). The individual lines have different linear and angular coefficients, i.e. parameters a and b in (5.4), thus indicating the need for a calibration routine. There is a group of lines which are dislocated from the most lines. These outlier lines come all from the same receiver channels and may be attributed to a larger component tolerance deviation. The values determined by (5.8) after the calibration routine are compared with the reference values in Figure 5.10b. All results fall within a 10% deviation (dashed

lines). Even the few outlier lines in Figure 5.10a were correctly calibrated producing results within the 10% deviation bands.

Table 5.2: Results for the permittivity measurement with different substances. The reference permittivity values were taken from Lide (2005). Table also presents the mean value of measured permittivity $\bar{\varepsilon}$ according to (5.14), the relative deviation δ to the reference permittivity according to (5.15), and the maximal deviation from the mean value over the 256 measuring points $\Delta\varepsilon$ according to (5.16).

Substance	ε^{ref} (-)	$\bar{\varepsilon}$ (-)	δ (%)	$\Delta\varepsilon$ (%)
Air	1.0	1.02	1.68	8.18
Silicone Oil	2.0	1.92	-3.91	5.64
2-propanol	20.1	20.27	0.85	9.10
Glycol	41.1	45.18	9.92	0.86
Deionized Water	80.1	73.98	-7.64	7.67

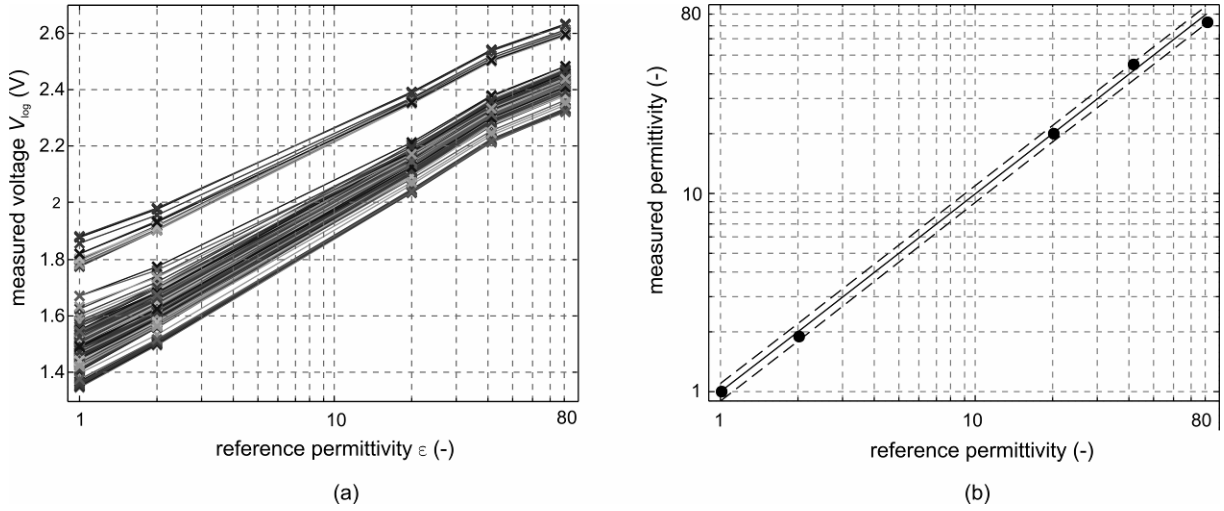


Figure 5.10: (a) Measured logarithmic voltage V_{\log} in dependence on the relative permittivity. (b) Comparison of measured (5.8) and the reference permittivity values. The dashed lines represent the 10% deviation from the ideal line; error bars representing the maximal signal deviation from mean value (•) are smaller in size than the symbols and therefore are not visible.

The system was then investigated regarding instrumental noise. The wire-mesh sensor was covered with silicone oil and 1 000 frames were recorded at 625 fps. Again a voltage amplitude of 3 V_{pp} and excitation frequency of 5 MHz were used. The standard deviation of the measured voltages V_{\log} for each crossing point over the 1 000 frames was used to estimate the instrumental noise. Figure 5.11 illustrates the

distribution of the standard deviation of the measured voltages for the 256 crossing points. A maximal value of the standard deviation of 0.58 mV was obtained.

Using the uncertainty propagation rules (ISO 1995) in (5.8), the noise in the permittivity measurement caused by the noise in the voltage measurement can be estimated. Hence,

$$\frac{U(\varepsilon)}{\varepsilon} = \frac{U(V_{\log})}{a}, \quad (5.17)$$

where $U(x)$ denotes the uncertainty in the quantity x . Applying a typical value for the system parameter $a = 0.2154$ and taking the maximal value of 0.58 mV from Figure 5.11, a maximal relative noise level of 0.27% in the permittivity measurement is found. This noise level is much smaller than the maximal deviation of the individual crossing point measurements as showed in Table 5.2 and can therefore be neglected.

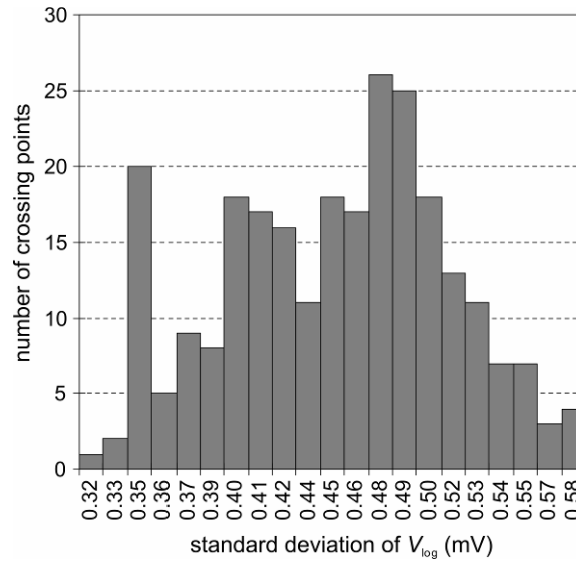


Figure 5.11: Distribution of the standard deviations for all 256 crossing points determined from 1 000 acquired frames for the wire-mesh sensor covered with silicone oil.

5.4.2 Time response

To assess the system time response, the step response of one crossing point was evaluated. The excitation frequency of 5 MHz was switched on and off at a 50 kHz repetition rate by means of the analog switch (Sx in Figure 5.4). The analog switch control voltage V_{ctr} , the excitation voltage at the crossing point V_{cp} , and the log-detector output voltage V_{\log} were measured with an oscilloscope. Figure 5.12 presents

the results showing normalized voltages. It is clear that the time response of the circuit is determined by the receiver circuit response. While the voltage V_{cp} responds within a few nanoseconds, V_{log} presents typical exponential first-order system response. The measured settling times for 1% error in V_{log} were $4.13\ \mu\text{s}$ and $4.40\ \mu\text{s}$ for turn on and turn off, respectively. These values are slightly larger than the ones specified in the log-detector data sheet, which is explained by the fact that a larger capacitor value ($68\ \text{pF}$ instead of $2\ \text{pF}$ recommended in the data sheet) was used at the log-detector output to reduce the output signal ripple. If required, the time response might thus still be improved by lowering the capacitor value, but on cost of increasing the noise level and thus the uncertainty in the measurements. The measured time response corresponds to a maximal sampling frequency of $225\ \text{kHz}$ for the analogue-digital conversion and thus gives a maximal frame rate of $14\ 063\ \text{fps}$ for the actual 16×16 sensor configuration.

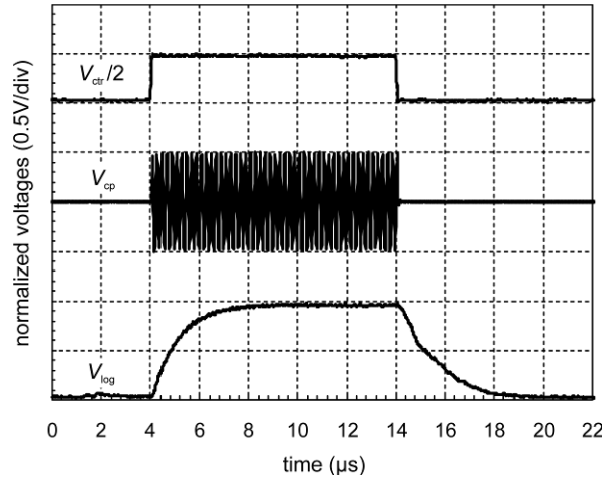


Figure 5.12: Step response of the receiver circuit showing the normalized analogue switch control voltage V_{ctr} , the excitation voltage V_{cp} , and the log-detector output voltage V_{log} .

5.4.3 Comparison with conductivity wire-mesh sensor

In order to compare the image produced by the novel capacitance wire-mesh with a standard conductivity wire-mesh sensor, the following experiment was carried out. Since water is a conducting substance it can be measured by both conductivity and capacitance wire-mesh sensors and was therefore chosen.

The flow channel with integrated sensor was filled with water (electrical conductivity $\sigma = 2\ \mu\text{S}/\text{cm}$), placed in the horizontal position and rotated 45° . In this

way, a well-defined planar phase boundary imitating a stratified two-phase flow is realized. Figure 5.13a presents the cross-sectional images generated by both systems, where 10 frames were acquired at 625 fps and averaged. In Figure 5.13b the lines of equal void fraction α are shown, which were calculated by interpolating the measured values at the crossing points. These lines represent the interface between the two phases. The agreement between the images obtained with both systems as well the lines of equal void fraction are very good. The figures also illustrate the suppression of crosstalk between the individual crossing points. The presence of crosstalk would have caused a blurring effect in the image and hence a distortion in the line of equal void fraction. The water-air interface would not have been correctly represented. In fact, the accuracy of the detection of the interfacial area corresponds to the size of one mesh of wires, i.e. 3.12 mm for this sensor. In this way, the image produced by the capacitance wire-mesh sensor (as well as the conductivity sensor) is free of crosstalk artifacts.

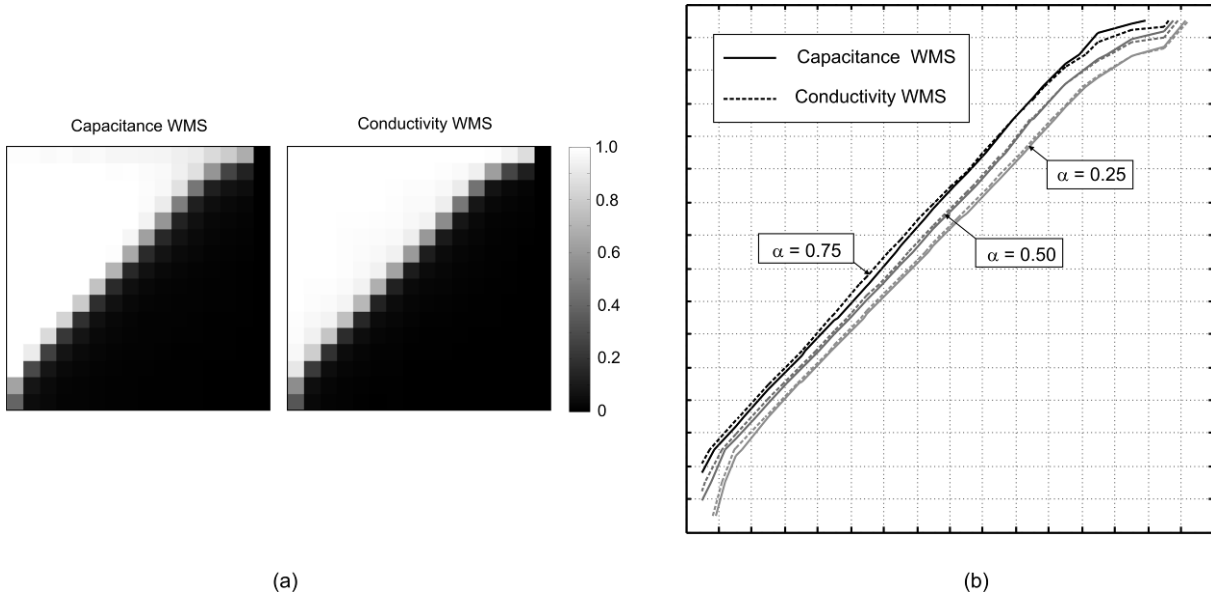


Figure 5.13: (a) Cross-sectional images obtained with the capacitance and conductivity wire-mesh sensors when measuring a planar phase boundary. The gray scale represents the void fraction α . (b) Comparison of the lines of equal void fraction for three selected values ($\alpha = 0.25, 0.50$, and 0.75). The lines were calculated by interpolating the measured values at the crossing points.

5.4.4 Influence of liquid conductivity

Although the circuit of the capacitance wire-mesh sensor was conceived and implemented to measure capacitances, the influence of liquid conductivity, i.e. the resistive part of impedance, on the auto-balancing circuit was investigated. In this way, as described in section 3.1.2, the unknown impedance of a crossing point for a lossy dielectric is formed by a capacitor (linked with fluid permittivity) and a resistor (linked with fluid conductivity).

The rectangular cross-section wire-mesh sensor (Figure 5.1a) was filled with water of increasing conductivity values which was obtained by the controlled addition of sodium chloride. The reference conductivity was monitored with a conductivity meter Cond 330i (WTW GmbH, Germany, 0.5% measurement uncertainty). For each reference conductivity value, 10 frames were acquired at 625 fps and averaged. Figure 5.14a shows the measured V_{\log} voltages for the conductivity values varying from 1 to $10^4 \mu\text{S}/\text{cm}$ (or 10^{-4} to 1 S/m). The lowest investigated value of $1 \mu\text{S}/\text{cm}$ represents deionized water. Tap water has a conductivity of about $400 \mu\text{S}/\text{cm}$. The highest value measured ($10^4 \mu\text{S}/\text{cm}$) corresponds approximately to sea water with a salinity of 5.6 g/l at 25 °C and 10^5 Pa (Perkins and Lewis 1980).

Figure 5.14 shows the measured voltage for different conductivity values of water for one exemplary crossing point. Similar behavior was found for the other crossing points. Basically, two regions can be identified. For conductivity values of up to $100 \mu\text{S}/\text{cm}$, the measured voltages V_{\log} are constant; meaning that the conductivity does not play any role, i.e the circuit is capacitance-dominant. For conductivity values higher than $100 \mu\text{S}/\text{cm}$, the measured voltage increases with increasing conductivity. In this second region the resistive part of the impedance starts influencing the measurement. It is predicted that at a certain point the circuit becomes resistance dominant and the response of V_{\log} turns linearly dependent on the conductivity.

To demonstrate the above described behavior a closer analysis was performed. Since the measured quantity is now complex, the relationship governing the circuit output voltage must be revised. In the circuit of Figure 5.4, the logarithmic detector measures the amplitude of the sine wave voltage V_o disregarding its phase value, thus (5.4) may be written considering the modulus of the complex permittivity of a crossing point

$$V_{\log} = a \cdot \ln \left(\left| \varepsilon - j \frac{\sigma}{\omega \varepsilon_0} \right| \right) + b. \quad (5.18)$$

Using the identity of complex numbers $|x + jy| = \sqrt{x^2 + y^2}$ and rearranging (5.18), one obtains

$$V_{\log} = a' \cdot \ln \left((c')^2 + \sigma^2 \right) + b', \quad (5.19)$$

where a' , b' and c' are constants. A non-linear least-squares fit was performed using (5.19). Figure 5.14 also depicts the obtained regression curve to the measured data. Additionally, two asymptotic lines (dotted) are also shown, indicating the two regions previously mentioned. The horizontal line represents the capacitive region and the inclined line the resistive one. Furthermore, the excellent regression coefficient $R^2 = 0.999$ confirms the proposed model. With this experiment the possibility of investigation of conductive liquids by means of a capacitance wire-mesh sensor is demonstrated. Further work should emphasize the investigation of flowing two-phase mixtures.

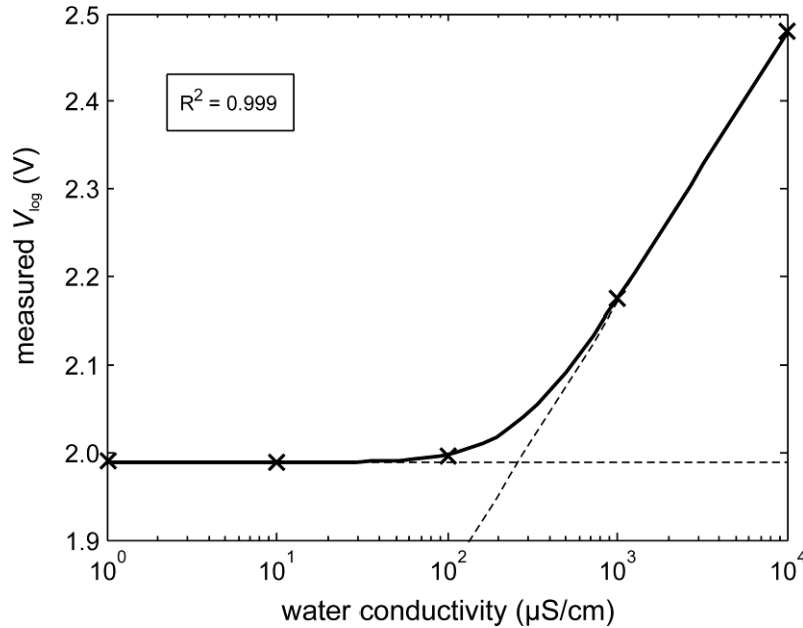


Figure 5.14: Measured voltage (×) in dependence of water conductivity for an exemplary crossing point. Non-linear least-squares regression (full line), where the capacitive and resistive dominant regions are clearly shown by the help of the two asymptotic lines (dotted).

5.5 Application to flow measurement

In order to demonstrate the applicability of the newly developed sensor in investigation of flow problems, a few selected flow experiments have been carried out which are presented and discussed in this section. It is not the aim here to completely investigate the flow phenomena, but rather present the sensor as new experimental tool.

5.5.1 Oil-air stagnant two-phase flow

As a first application, the capacitance wire-mesh sensor was employed to measure silicone oil/air stagnant two-phase flow. The vertical flow channel with the integrated wire-mesh sensor (Figure 5.1a) was filled with silicone oil ($\varepsilon = 2.7$) and air was injected at the bottom of the column through a hole located in the very center of the channel. Hence, the flow channel was operated as a very simple bubble column. The wire-mesh sensor controlled by the first generation electronics was set up to acquire data at maximum frame rate of 625 fps. Two reference images for the calibration routine with 100% gas and 100% liquid were acquired at the beginning of the experiments.

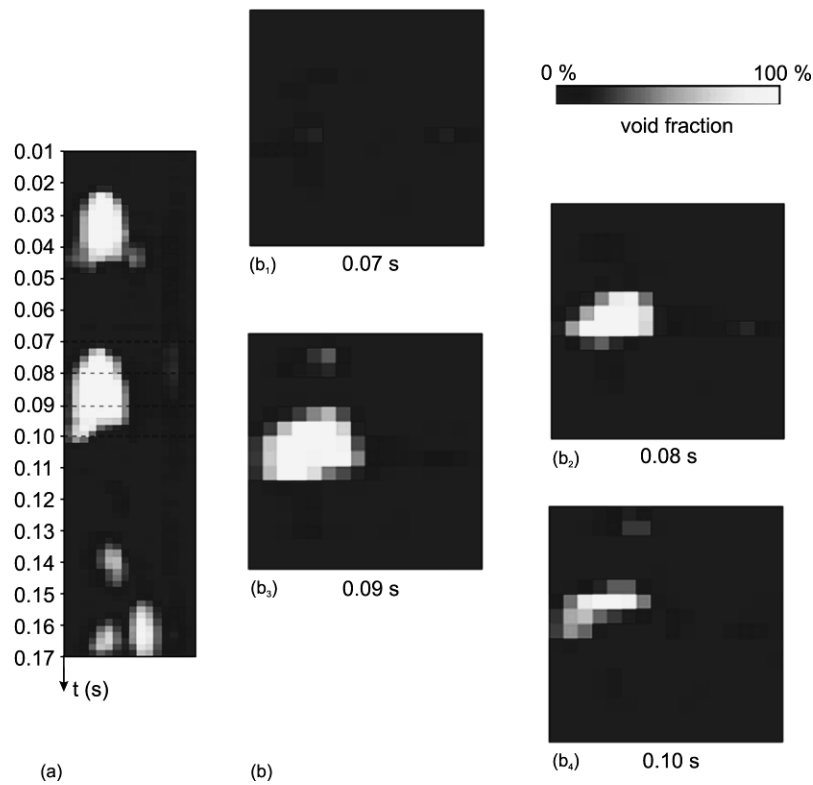


Figure 5.15: (a) Axial and (b) cross-sectional slice images of an oil/air bubbly two-phase flow acquired with the capacitance wire-mesh sensor.

Figure 5.15 shows images obtained with the sensor and application of the calibration routine. The four cross-section images show details of one single bubble for selected time frames. The image on the left (Figure 5.15a) is an axial slice image which is produced by taking the values from electrode number eight, i.e. along a central chord of the channel. Two larger bubbles can be observed. Note that the vertical axis has the dimension of time and not space. Although the permittivity values of the two substances are rather close to each other, they are precisely distinguished by the capacitance wire-mesh sensor.

5.5.2 Oil-air vertical pipe flow

The capacitance wire-mesh sensor was also tested to measure pipe flow under industrial conditions. The 24×24 wire-mesh sensor (Figure 5.1b) was used to investigate an oil-gas vertical flow in a 67 mm diameter pipe in different flow regimes. The experiments were carried out on an inclinable rig facility of the Chemical Engineering Laboratory of the School of Chemical and Environmental Engineering, University of Nottingham, UK. It had been employed for earlier studies with a 38 mm diameter pipe (Geraci *et al.* 2007). It had more recently been modified and used for flow measurements with the present 67 mm diameter pipe (Hernandez Perez *et al.* 2007).

Table 5.3: Some physical properties of the silicone oil used in the experiments.

Parameter	Value
relative permittivity	2.7
density	900 kg/m ³
viscosity	5.25 mPa·s
surface tension	0.02 N/m

a) Experimental setup and data analysis

The facility consists of an inclinable 6 m long rigid steel frame which can be rotated between vertical to horizontal (Figure 5.16). The 67 mm test pipe made of transparent acrylic glass is mounted on the frame and was instrumented with the wire-mesh sensor and a high-speed camera (Photron, Fastcam-APX 120K). The fluids

used were silicone oil and air. Some physical characteristics of the silicone oil are listed in Table 5.3.

Oil was taken from a storage tank and pumped through a set of rotameters to monitor the flow rate and into the mixer. Air from the main laboratory 6 bar-compressed-air system was mixed with the oil in the pipe inlet. The air flow rate was also monitored by a set of calibrated rotameters. The oil-air mixer was mounted at the bottom of the test pipe. The wire-mesh was located 5 m from inlet (i.e. one meter from the outlet) so that the flow monitored was well-developed. The pipe outlet is connected to a gravity separator, where the air is released to atmosphere and the liquid is returned to the storage tank. The high-speed video system was located 0.5 m below the wire-mesh sensor.

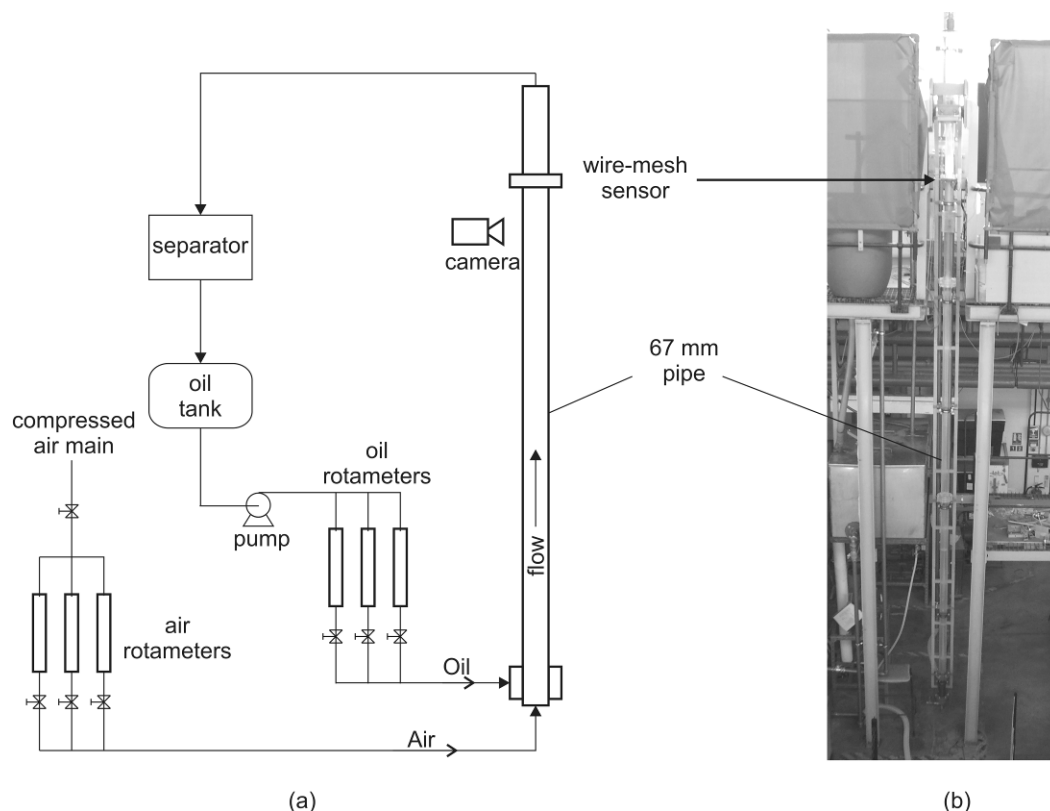


Figure 5.16: Experimental setup of inclinable rig facility at University of Nottingham, UK; (a) schematic diagram and (b) photo.

In the work presented here, the pipe was mounted vertically and measurements were carried out under different conditions determined by the superficial gas velocity U_G , in order to investigate flow regimes. For the preset value of the superficial liquid velocity $U_L = 0.2$ m/s different values of the superficial gas velocity were chosen in a range between 0.05 and 4.7 m/s. After adjustment of U_G the flow was measured with

the wire-mesh sensor at a frame rate of 5 000 fps and in parallel with the high-speed video system at 1 000 fps.

Two visualization techniques were used to display the measured wire-mesh data: (i) axial slice images and (ii) side projections. In the former one the temporal evolution of phase fraction values along the central electrode is displayed. Thus, such an image obtains the character of a side view of the flow structure on a vertical cut through the pipe along the axial direction. With the second technique, side projections are processed using a simplified ray-tracing algorithm as described in detail by Prasser *et al.* (2005a). In this visualization technique, an illumination of the three-dimensional phase fraction distribution by parallel white light is assumed and the light intensity departing in the direction of a virtual observer is calculated. For this purpose, virtual absorption and dispersion coefficients for the three light components (red, green and blue) are assigned to the liquid and gaseous phase, respectively. This method supplies instructive pseudo-3D imaging.

b) Flow patterns in vertical pipe

The function of the sensor is illustrated on examples of flow visualization for a constant $U_L = 0.2$ m/s. The pictures in Figure 5.17 show the transition of a few different flow regimes processed with both visualization techniques described above.

At the lowest gas flow rate, bubbly flow is observed. By increasing the gas superficial velocities, the transition to slug flow, churn turbulent flow, and finally to annular flow occurs. The vertical axis represents the time of 3 s. This time-axis may be transformed into a virtual z-axis, when it is scaled according to the velocity of the gaseous phase (Prasser *et al.* 2005a).

In Figure 5.17a, side projections are displayed from which the flow pattern can be easily recognized. However, the side projections have the same disadvantage which also occurs in visual observation of transparent pipes: with increasing gas fractions, the visualization of internal structures is no longer possible and the depth information of flow is lost. For this reason, the axial slice images are also presented (Figure 5.17b). Such slice images have the advantage of presenting the flow structure in the mid-plane of the pipe without the view obstruction by bubbles in the region close to the pipe wall. For instance, the images where $U_G \geq 0.47$ m/s, some irregular flow structures can still be identified, whereby for the side projections almost nothing can be identified. Thus, both visualization techniques complement each other in the visualization of flow structures.

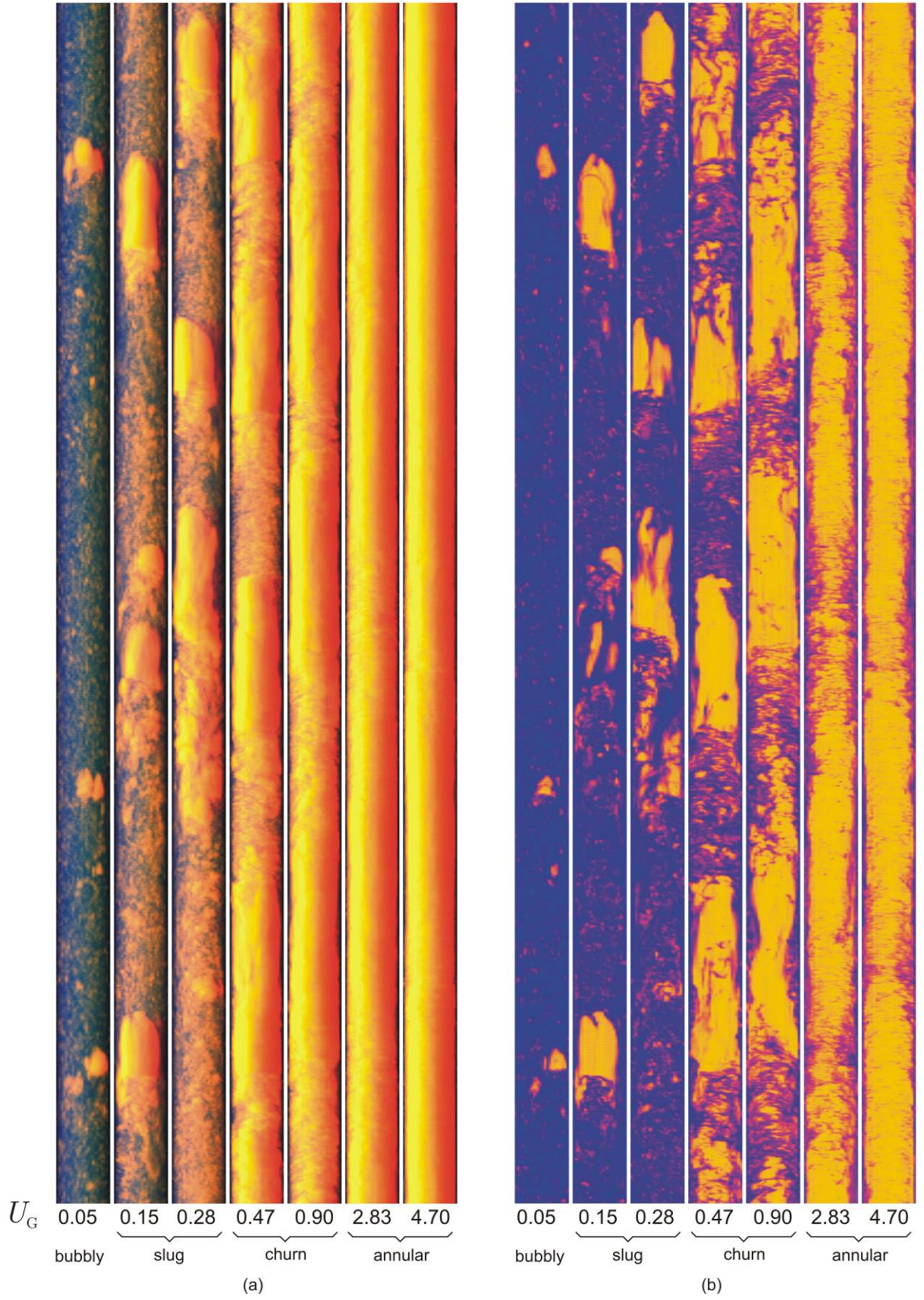


Figure 5.17: Visualization of wire-mesh sensor data obtained in the pipe flow measurement for $U_L = 0.2$ m/s; (a) side projections and (b) axial slice images. The corresponded flow patterns obtained are also indicated.

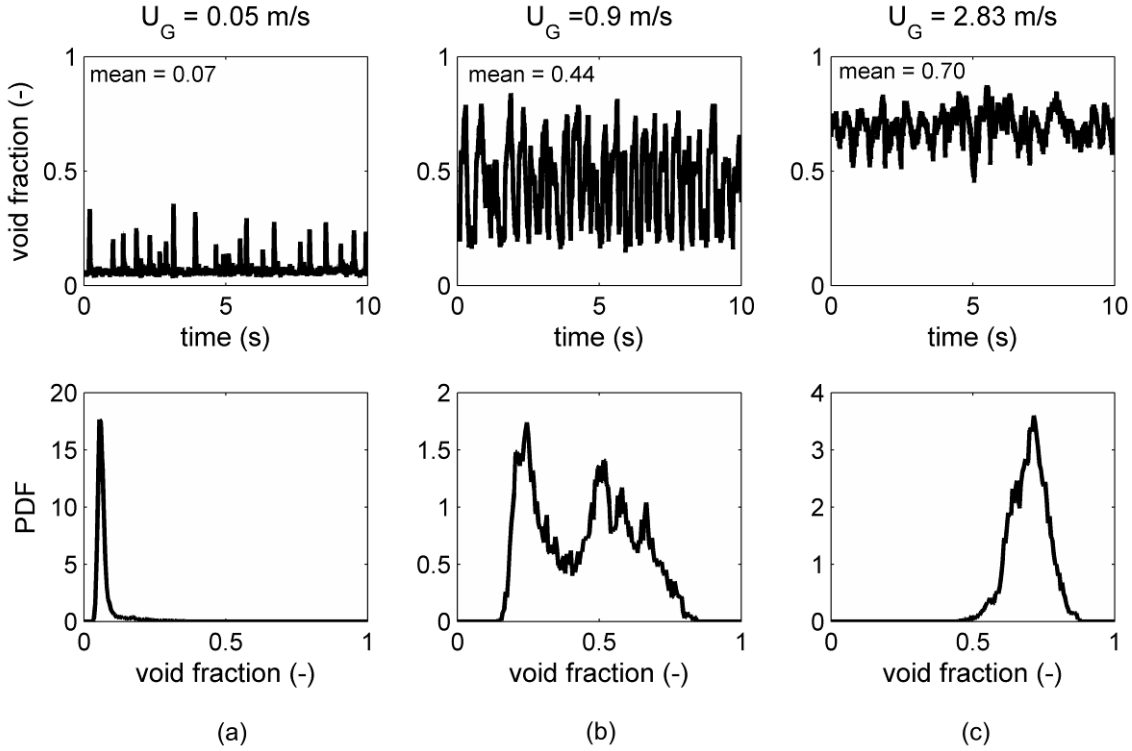


Figure 5.18: Time series and probably density functions (PDF) of the cross-sectional averaged data for three flow conditions; (a) bubbly, (b) slug and (c) churn flow.

Quantitative insights of the flow are obtained by the cross-sectional averaged time series of the void fraction measured by the wire-mesh sensor. For more details in the algorithmic calculation of such time series see Prasser *et al.* (2002a). Examples of time series are illustrated in Figure 5.18. The cases were selected to be in bubbly flow ($U_G = 0.05$ m/s), slug flow (0.9 m/s) and churn flow (2.83 m/s).

The low gas flow rate condition is characterized by low void fraction with quite regular peaks of higher void fraction probably representing clusters of bubbles. The slug flow data has alternate periods of high and low void fraction. The case for higher flow rate is churn flow which has mainly high void fractions with regular troughs of lower signal. In Figure 5.18 the probably density functions (PDF) of the time series are also plotted, showing the typical low void fraction peak for bubbly flow, the double peak for slug flow, and the broadened peak at higher void fractions for the churn flow (Costigan and Whalley 1997).

c) Comparison with high-speed camera images

For qualitative comparison purposes, the pipe flow was also investigated by means of a high-speed video system. Figure 5.19 shows two exemplary images for gas superficial velocities of 0.05 and 2.83 m/s. Even for the lowest gas flow rate it is

obvious that due to the swarms of small bubbles in the pipe the optical investigation of flow structures located in the inner circle of the pipe is difficult. However, a bigger bubble may be recognized (indicated by an arrow). For $U_G = 2.83$ m/s, the two-phase oil-air mixture forms a foam which completely obfuscates the pipe internal, thus no information of the flow structure can be obtained. For those observations, the limitation of optical visualization techniques in the investigation of multiphase flows becomes clear. Optical methods are only suitable for the case of very low void fraction values. Here the advantages of using a wire-mesh sensor for the flow visualization are fairly clear.

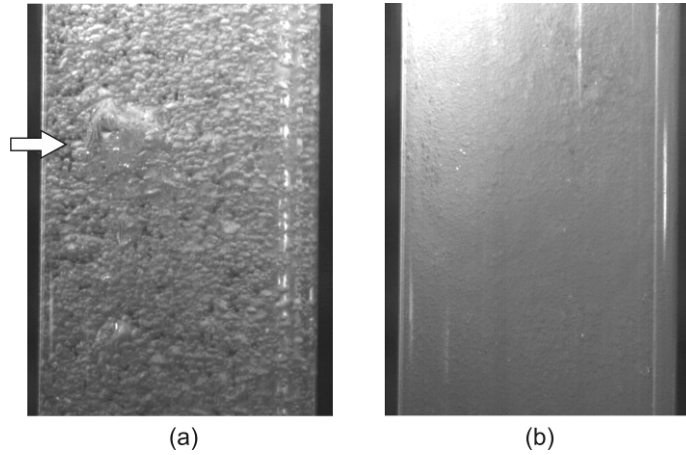


Figure 5.19: Video images of the oil-gas flow for two different gas superficial velocities U_g ; (a) 0.05 m/s; (b) 2.83 m/s.

As described above and from Figure 5.19, for the lowest gas superficial velocity, the flow is characterized by a swarm of small bubbles which disturb the optical visualization and from the visual inspection are expected to have diameters of a few millimeters only. Of course, the wire-mesh sensor cannot resolve bubbles smaller than its spatial resolution (2.8 mm for the sensor used), but the passage of such small bubbles between the crossing points of a wire-mesh sensor lower the measured signal. As a result, the bubbles are not fully resolved but their presence can be detected. This fact is readily appreciated in the PDF for $U_G = 0.05$ where the peak occurs at about 0.06 void fraction. Earlier studies with the wire-mesh sensor in air-water systems have shown that the peak for bubbly flow at similar conditions occurs at much lower void fraction values (Azzopardi *et al.* 2008) due to the fact that the swarm of small bubbles was not present. The main reason for the occurrence of small bubbles in the oil-air system is the much lower surface tension of oil than water which induces the formation of such small bubbles.

5.5.3 Three-phase flow

Three-phase gas-oil-water flow is a common occurrence in the petroleum industry. Although many different three-phase metering systems have been developed and tested (see section 2.2.1c), none can be referred to as generally applicable or universally accurate. Many current systems utilize radioactive sources in their measurement concept, so that such meters must comply with high security and reliability standards due to environmental and legal issues (Corneliussen *et al.* 2005). Therefore, there is a continuous search for new technologies which may substitute the radiation-based phase fractions distribution measurement.

A possible alternative to the current-in-use systems can be the newly developed capacitance wire-mesh sensor. The good accuracy achieved in the permittivity measurement (section 5.4.1) allows the wire-mesh system to securely distinguish each of the three phases of an air, oil and water flow. A preliminary test has been performed regarding the capability of the system to investigate a three-phase flow. The flow channel with integrated wire-mesh sensor was filled up with air, oil and water in such a way that each of these substances occupies one third of the cross-section area. It was also placed in a horizontal position. In this way, a three-layer structure as shown in Figure 5.20 was obtained which imitates a stratified flow. Prior to begin of the experiment a two-point calibration was realized with air and water as reference. One single image was acquired and Figure 5.20 depicts the result, in which a logarithmic color scale was used for the permittivity values. Although the permittivity values of air ($\varepsilon = 1$), oil ($\varepsilon = 2$) and water ($\varepsilon = 80$) lay in a high dynamic range, all three phases can be clearly recognized.

In order to further investigate the capability of the wire-mesh sensor for investigating transient three-phase flow, the flow channel with integrated sensor, having the three substances air, oil and water, was shaken to simulate a flow in the sensor box. The 16×16 wire-mesh sensor was configured to acquire 625 fps while the sensor box was agitated. Figure 5.21 depicts the slice image for the central electrode of the flow measured during three seconds. With the employed color scale, air is shown in red, oil in orange and water in blue color, respectively. Starting from the stratified condition at the beginning of the experiment, an oil slug followed by two water slugs can be clearly seen. The interfacial areas between each phase are also visible having intermediate colors.

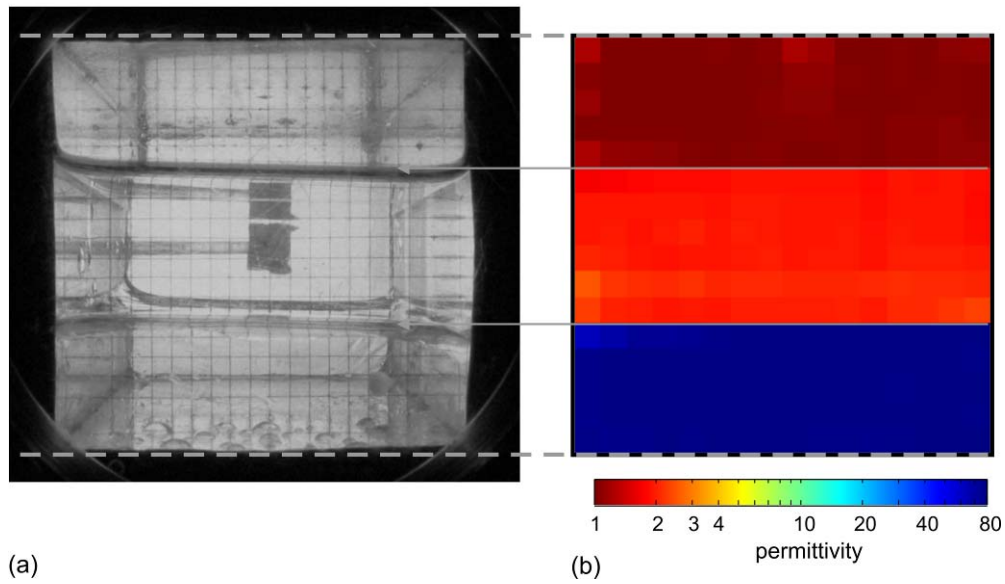


Figure 5.20: (a) Photo and (b) cross-sectional image of an imitated three-phase stratified flow constituted of air, oil and water. A logarithmic color scale was used for the permittivity values.

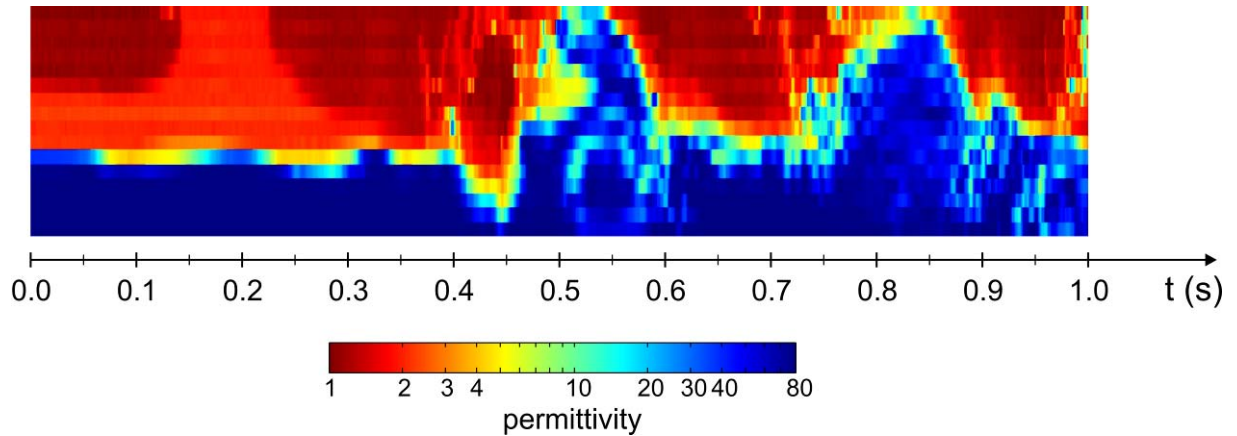


Figure 5.21: Slice image for the central electrode of the three-phase flow.

A last experiment was carried out aiming to monitor the separation process of a three-phase air-oil-water mixture. For this reason, the sensor box (as previously used) containing the three substances was heftily agitated in order to properly homogenize the multiphase mixture. As a result of the mixing process, an emulsion is formed which was also visually observed. After the agitation the sensor was put at rest. The agitation and the following separation process were monitored by the wire-mesh sensor and in parallel with a video camera. Figure 5.22 depicts the process evolution where a slice image of the central electrode for a period of 60 s is displayed. The gaseous phase separates very rapidly from the liquid mixture due to the large

difference in density between gas and liquid phases. The emulsion formed by the agitation can be clearly observed as light blue region in the axial view having a permittivity value between 2 (for oil) and 80 (for water). The emulsion is continuously broken up and at the end of the 50 s period the three phases are completely separated. This behavior was also monitored by the video camera. The three static video images at exemplary time steps in Figure 5.22 also show the evolution of the separation process. The emulsion is seen as opaque region due to high light scattering.

The simple experiments described in this section have shown promising results in the investigation of three-phase flow problems, thus encouraging for the further investigation of the performance of the wire-mesh sensor in real three-phase flows.

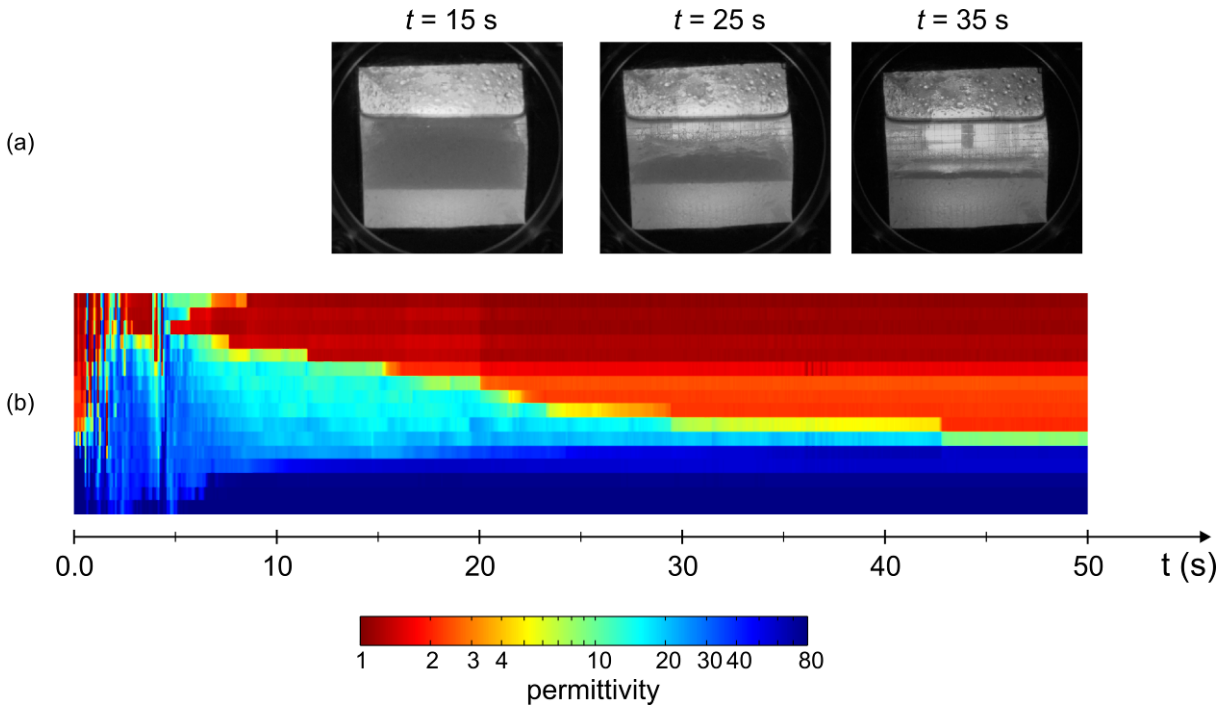


Figure 5.22: Measurement of the separation process of an air-oil-water mixture. (a) Video images, (b) slice image for the central electrode.

5.6 Conclusions

In this chapter the development, evaluation and application of a new wire-mesh sensor imaging system was presented. The system is based on capacitance (permittivity) measurements and can measure the phase fraction distribution in a flow cross-section with high spatial and temporal resolution. This new sensor is able

to measure in either electrically non-conducting or conducting fluids. The investigation of the conductivity influence on the capacitive measuring circuit shows that the wire-mesh sensor may be also applied to investigate conductive fluids with conductivity values σ up to 1 S/m. In addition to the improved range of measurable substances, another special advantage of the capacitance wire-mesh sensor is the possibility to use electrically isolated wires, which enables to operate the sensor with protective wire coatings, for instance in aggressive media.

The spatial sensitivity of a crossing point in the wire-mesh sensor for different geometries has been analyzed by means of simulations with a commercial FEM software. The results support the hitherto accepted assumption that the measurement volume of a crossing point can be approximated by a cube centered at the crossing point. Nevertheless, the exact sensitivity may be taken into account leading to an improved measurement accuracy of a wire-mesh sensor.

The experimental evaluation of the prototype wire-mesh sensor system has shown good reproducibility and accuracy in capacitance measurements even at a rather short response time, thus allowing the system to be employed in the investigation of a wide range of substances even with close permittivity values, such as for air and oil. The good system accuracy also allows for the investigation of three-phase air-oil-water mixtures. In preliminary experiments, the three phases in a stratified condition as well as in a simulated flow were correctly acquired, and the emulsion formation was also properly captured by the sensor. The evaluation of performance and limitations of the sensor for three-phase flow applications must still be deeper investigated in the future.

6 Planar array sensor

This chapter introduces a novel sensor modality for imaging near-wall multiphase flows. The planar sensor is formed by a matrix of interdigital sensing structures and an associated electronics that measures very fast the conductivity or permittivity of the multiphase mixture at each individual sensing structure. In this way, instantaneous images of fluid distributions over sensor's surface are obtained.

6.1 Introduction

Interdigital electrode structures have been used for decades in a large diversity of sensing applications and research fields. Among them, the most common are nondestructive testing, chemical and physical sensing, biotechnology and telecommunications (Mamishhev *et al.* 2004, Mukhopadhyay 2005). The working principle of interdigital sensors is based on the interaction of the electrical field generated by the sensor with the material or substance under test. The perturbation of the electrical field can be detected at a sensing electrode and is related to conductive or dielectric properties of the substance/material in the vicinity of the sensor. An important advantage of such electrode systems is the simple and cheap fabrication process and the possibility to investigate materials or substances from measurements with a single-side surface contact. Most of the current technical implementations of such sensors use one or a few sensing structures to investigate the material under test. The measurement accuracy must be high in order to assess chemical or physical material properties whereas the measuring time is normally not a concern and typically ranges from hundreds of milliseconds to a few minutes depending on application and accuracy needs (Mamishhev *et al.*, 2004, Kaatz and Feldman 2006). More recently multichannel sensors have been introduced to improve

the capability of sensing systems (Wittstock 2002). As a result, either the simultaneous measurement of multiple parameters or the introduction of imaging capability has been achieved (Gardner *et al.* 1995, Hermes *et al.* 1994, Wang *et al.* 1996).

The characteristics described above combined with high-speed measurements make interdigital sensors very attractive to be employed in the investigation of flow phenomena. The sensor can be mounted onto the wall of pipes or vessels and thus have a minimal influence on the flow.

For the investigation of highly transient multiphase flows, a novel high-speed imaging system was developed based on electrical impedance measurements of a multichannel interdigital sensor (Da Silva *et al.* 2007c). The sensor comprises of a matrix of sensing structures which are individually measured in a multiplexed manner. By measuring the electrical conductivity or the permittivity of the interdigital sensing structures, phases of a multiphase flow or component concentration can be visualized and monitored. The images obtained from the sensor thus represent the component or phase distribution over the sensing area.

This chapter initially describes the developed planar array sensors. Two different sensing principles were applied to operate the planar sensors: conductivity-based and permittivity-based. Each sensor modality is described individually in separated sections. Moreover, for each type of measuring principle developed, the sensor system is experimentally evaluated and some flow applications are presented and discussed.

6.2 Interdigital array sensor

The planar array sensors used to investigate flow problems were manufactured using standard printed-circuit board (PCB) fabrication technology. The simplicity and low cost of this fabrication technology permits a rapid design and manufacturing of arbitrary sensor geometries. Two examples of manufactured sensors are shown in Figure 6.1 and Figure 6.2. The former was built in a rectangular geometry with 4096 interdigital sensing structures evenly distributed over an area of 620 mm \times 500 mm. The interdigital sensing structures are multiplexed in a matrix with 64 driver (rows) and 64 sensing electrodes (columns). The sensor board was designed to fit to an experimental flow channel. Four high-density connectors at the back side of the sensor (not shown in Figure 6.1) allow the sensor to be connected to the measuring electronics.

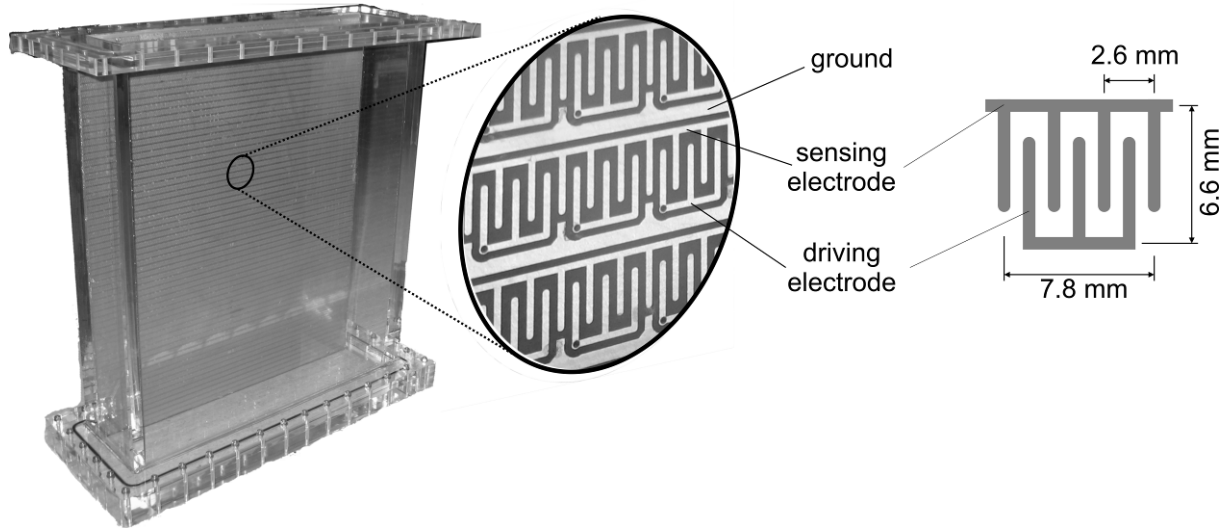


Figure 6.1: Printed-circuit board of a planar sensor containing 64×64 interdigital sensing structures fitted to an experimental flow channel. The size of each sensing structure is $5.8 \text{ mm} \times 6.6 \text{ mm}$ and the size of the whole sensor is 620 mm by 500 mm .

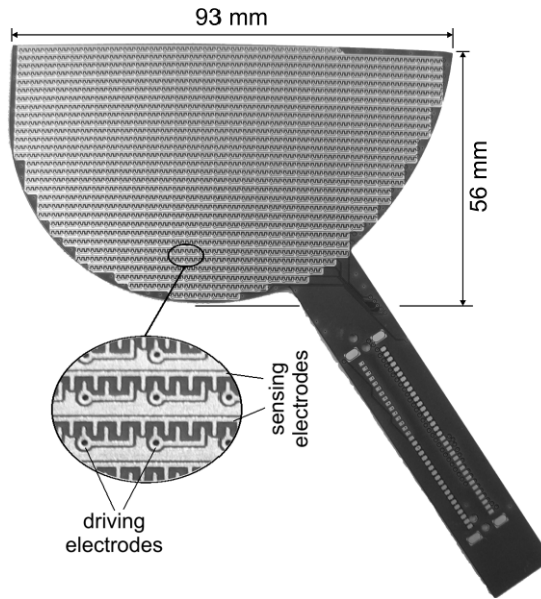


Figure 6.2: Printed circuit board of a planar sensor constructed for mounting inside a fluid coupling with a modified layout of 32×32 interdigital electrodes and an interdigital sensing structure in detail. The spatial resolution of a single sensing structure is $2 \text{ mm} \times 3 \text{ mm}$.

The sensor of Figure 6.2 has a modified half-moon shape with approximately 1 000 sensing structures arranged in a 32×32 matrix. This sensor was employed to investigate the fluid distribution inside a fluid coupling (see section 6.3.5). A bar-line extension of the board carries the ground shielded sensor lines to a connector. In both

cases the electrodes are gold plated to reduce electrochemical effects during electrical measurement.

6.3 Conductivity-based planar sensor

6.3.1 System description

The measuring electronics applied for the conductivity measurement is similar to the electronics of a conductivity wire-mesh sensor (Prasser *et al.* 1998) and is described below. Figure 6.3 depicts the block diagram of the measuring electronics for an exemplary 64×64 electrodes configuration as well as the timing diagram for the excitation-measuring scheme.

The transmitter electrodes are connected to a bipolar voltage source in a successive order while all the other transmitter electrodes are connected to ground potential by means of a set of analog switches. The outputs of the switches are buffered by operational amplifiers in order to create a low impedance path. This step assures that the potential of all transmitter electrodes, except the one of the currently activated electrode, are at ground potential. A bipolar excitation voltage (dc-free) is employed to avoid electrolysis effects.

The electrical currents flowing from the activated electrode to the sensing electrode are converted to voltage by a set of auto-balancing bridge circuits. Since the quantity of interest here is the electrical conductivity of the fluid over a sensing structure, the auto-balancing bridge circuit is dimensioned to be resistance-dominant. The capacitors in the feedback network of the opamps showed in Figure 6.3 serve only for frequency compensation. Typical wave forms for the excitation and the measured voltages are also shown in Figure 6.3. All voltages are analog-to-digital converted simultaneously at the rising edge of the sample-and-hold signal. This routine is repeated for all transmitter electrodes being activated. Once all transmitter electrodes have been activated and all currents have been measured, one frame is obtained containing 4096 values (for this sensor type) which corresponds to the distribution of the electrical conductivity over the sensor surface.

The various frames acquired during a measurement are saved in an $N_x \times N_y \times N_t$ data matrix in computer memory, where N_x , N_y are the number of transmitter and receiver electrodes and N_t denotes the number of time steps. The electronics is able to produce up to 2 500 images per second.

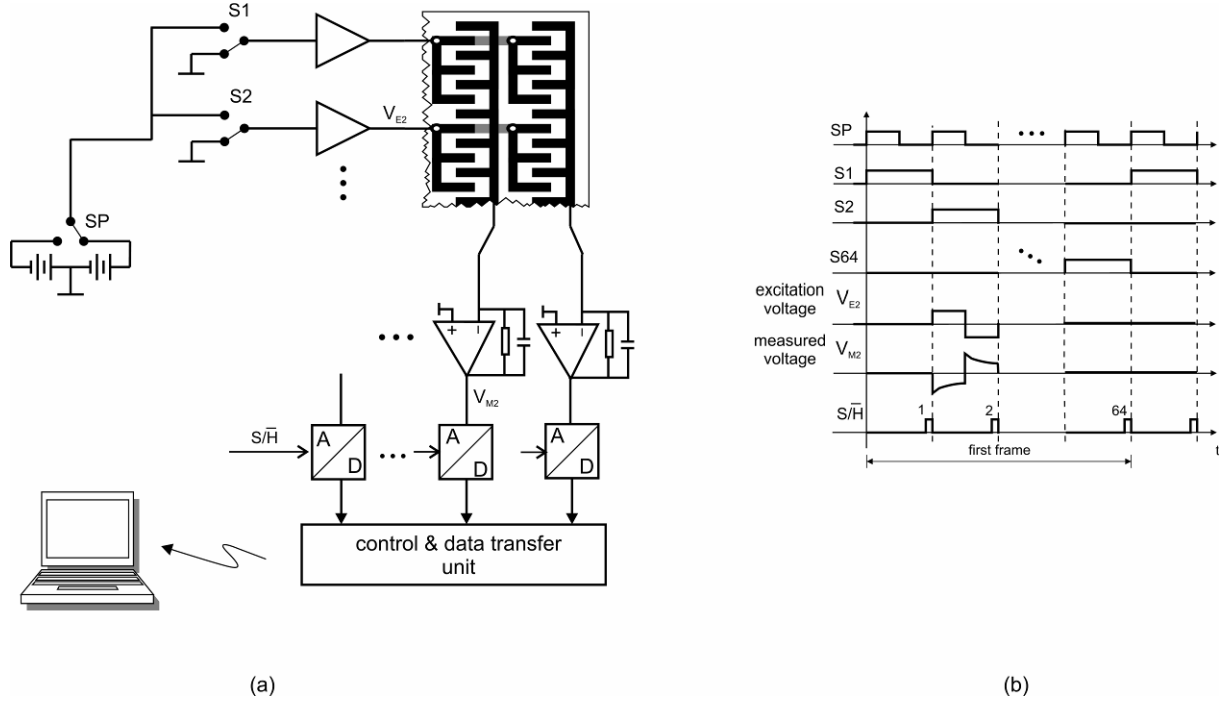


Figure 6.3: (a) Simplified block diagram of the measuring electronics. (b) Timing diagram for the multiplexed excitation and measuring scheme for the sensor. Voltages are sampled at the rising edge of the sample-and-hold signal. One frame is complete when the 64 transmitter electrodes have been activated and all currents have been measured. The signal SP denotes the polarity switch and S1 to S64 the analog switches.

6.3.2 Data processing

The voltage values measured by the surface sensor are proportional to the electrical current flowing from the transmitter electrode to the receiver electrode. This current basically depends on two parameters:

- the electrical conductivity σ of the liquid and
- the liquid wetting level (or liquid film thickness) of a sensing structure.

Depending on the application one of those two parameters can be explored to generate information about the fluid distribution across the sensor. Since the system generates only one measurement for two unknowns, one of the parameters must be known beforehand or kept constant during the experiments to generate an unambiguous output. In this way, two different situations can be investigated. In the case the wetting level is constant, that means, the sensing structures are always covered by a liquid, conductivity tracers can be applied to evaluate the flow in the

channel. The other choice is to measure the liquid distribution across the sensor assuming the conductivity being constant. For instance, the presence of gas bubbles on the surface can be detected due to the fact that the bubbles will change the wetting level of a sensing structure.

The acquired voltages for all sensing structures are saved in a data matrix, in the form $V(i, j, k)$ where i and j denote spatial coordinates and k the temporal point index. In principle, the evaluation of the measured voltage matrix $V(i, j, k)$ would be sufficient to investigate the component or phase distribution across the sensor surface. However, differences in the electrical response of the individual transmitter-receiver pairs, due to tolerances of electronic component or sensor elements, cause a variance in the measured signals which in turn produces artifacts in the resulting images. To compensate this variance two strategies are used to correct sensor's outputs depending on the measurement type, which are described bellow.

In the case that absolute conductivity values are to be assessed, the formula

$$\sigma(i, j, k) = V(i, j, k) \cdot a(i, j) + b(i, j) \quad (6.1)$$

may be used for calibration, since the measured voltage is directly proportional to the electrical conductivity of the liquid at the sensing structure. The parameters $a(i, j)$ and $b(i, j)$ are determined from measurements with substances of known conductivity. For this reason, data are firstly acquired with a substance of low conductivity σ^L covering the whole sensor, thus producing the reference data matrix $V^L(i, j)$. Normally average values over a certain time are used to reduce statistical signal fluctuations. This procedure is then repeated with the entire sensor surface covered with another substance having a higher conductivity value σ^H , which gives the second data matrix $V^H(i, j)$. In this fashion, applying (6.1) for both measurement situations, it is possible to determine them from

$$a(i, j) = \frac{\sigma^H - \sigma^L}{V^H(i, j) - V^L(i, j)}, \quad (6.2)$$

$$b(i, j) = \frac{V^H(i, j) \cdot \sigma^L - V^L(i, j) \cdot \sigma^H}{V^H(i, j) - V^L(i, j)}. \quad (6.3)$$

Assuming the second situation described above, where the wetting level or phase distributions are to be determined instead of conductivity values, the parameter

"wetting level" $w(i, j, k)$ may be introduced, which is determined from the ratio of the measured voltage and a reference point, hence

$$w(i, j, k) = \frac{V(i, j, k)}{C(i, j)}, \quad (6.4)$$

where $C(i, j)$ is the reference point which is obtained from a measurement when the whole sensor is covered by liquid. In this way, the wetting level w assumes values between zero and one, meaning a fully dry or a fully wet sensing structure, respectively.

With the described procedures in this section, images of the instantaneous fluid distributions across the sensor can be generated by mapping the wetting level $w(i, j, k)$ or conductivity values $\sigma(i, j, k)$ to a color scale and then plotting them in the spatial directions of i and j for a fixed value of index k . Sequences of these distributions can be viewed as video sequences by stepwise incrementing the temporal index k .

6.3.3 System evaluation

a) Measurement uncertainty

The system was firstly investigated regarding its accuracy in measuring the electrical conductivity. For this purpose different concentrations of sodium chloride were dissolved in deionized water thus obtaining solutions with different electrical conductivity values. The flow channel of Figure 6.1 was sequentially filled with NaCl-water solution with known conductivity value. Reference conductivity of the samples was measured by the conductivity meter Cond 330i (WTW GmbH, Germany, 0.5% uncertainty). For each reference conductivity value, 10 frames were acquired with the array sensor at a frequency of 2 500 Hz and averaged.

Figure 6.4a depicts the measured voltage values in dependence on the reference conductivity for all 4096 sensing structures. The error bars represent the maximal signal deviation from the mean values (circles). The three solid lines denote the linear fits for mean, maximal and minimal values within a same reference conductivity value. A linear dependence of measured voltage V versus conductivity values σ is obtained, as anticipated by (6.1). Each driving-sensing electrode pair has its own response. The large signal deviation is clearly shown in the plot. Its maximal value accounts to 32% when compared to the mean value. In principle, 4 096 lines with

different slopes and constant terms are obtained. Thus, the need of a calibration routine is evident, as already described in section 6.3.2.

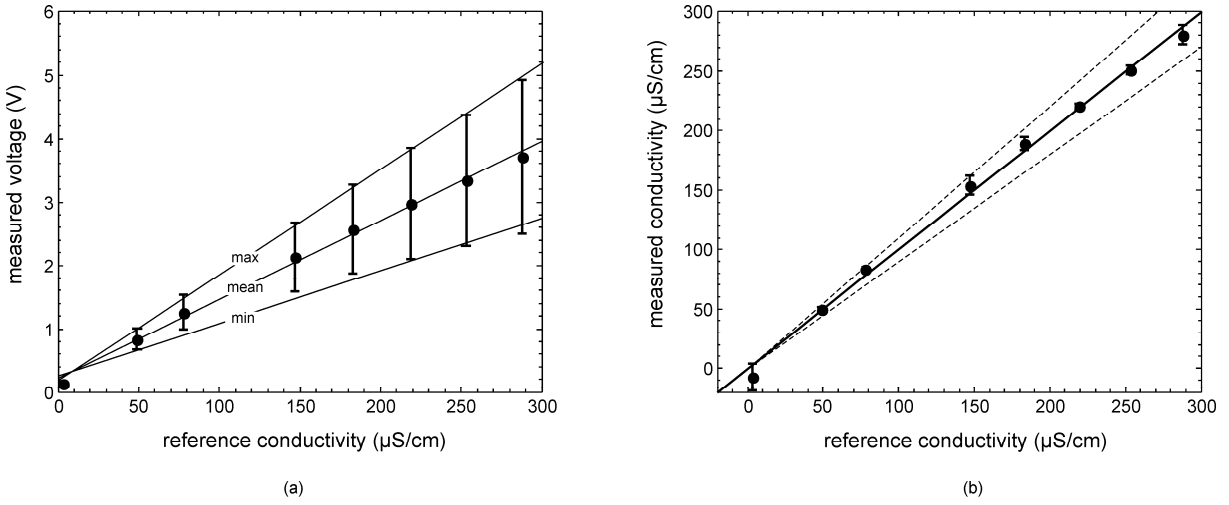


Figure 6.4: (a) Measured voltage in dependence of the electrical conductivity. The three solid lines represent the linear fits for mean, maximal and minimal values within a same reference conductivity value. (b) Comparison of calculated values after calibration by (6.1) and reference conductivity values. The dashed lines represent the 10% deviation from the ideal line (solid line). In both plots the errors bars denote the maximal voltage deviation from mean values (full circles).

The results obtained after the calibration routine are compared with the reference conductivity values in Figure 6.4b. The error bars represent the maximal signal deviation within a single conductivity value. The maximal value for the deviation is reduced to 7%, excluding the measurement at $3 \mu\text{S/cm}$. Furthermore, all measurements for conductivity values of more than $3 \mu\text{S/cm}$ fall within a 10% deviation (dashed lines). The measurements for the conductivity value of $3 \mu\text{S/cm}$ (first data point) have a too low voltage level (mean value of 130 mV) being more sensitive to noise and consequently lowering the accuracy. If lower conductivity values are to be investigated with the sensor, some parameters of the electronics such as amplifier gains or the amplitude of excitation voltage can be easily adapted for a new operation range.

The conductivity-based sensor was next evaluated regarding instrumental noise. For that, 1 000 frames at 2 500 Hz were acquired for the flow channel filled with water having a conductivity value of $150 \mu\text{S/cm}$. The standard deviation for each sensing structure over the 1 000 frames was determined. The maximal noise value found was 0.49%, which is one order of magnitude lower than the value obtained in the uncertainty evaluation (Figure 6.4).

b) *Depth sensitivity*

In order to experimentally evaluate the depth sensitivity of the sensor, the following experiment was carried out. The flow channel of Figure 6.1 with the integrated planar sensor was firstly put in the horizontal position. An electrically non-conducting glass plate of 120 mm \times 200 mm size and 3 mm thickness was placed over the planar sensor so that one of its endpoints was raised by a thin plastic spacer of 1.5 mm thickness while the other one was in direct contact with the sensor, forming an inclined plane as shown in Figure 6.5a. The flow channel was then filled up with water (conductivity 250 μ S/cm). In this way, a continuously growing water thickness over the sensor in an area of 15 \times 25 sensing structures was generated. In the following analysis only this area was taken into account. Ten frames at 2 500 fps were acquired and averaged. From the measured voltage values, the wetting levels were computed from (6.4) and a calibration measurement which was previously taken when the whole sensor was fully covered by water without plate. Figure 6.5b shows the mean values over the 15 rows for the calculated wetting levels. The form of the curve is an exponential rise which commensurate with previous analysis of interdigital structures (Li *et al.* 2006).

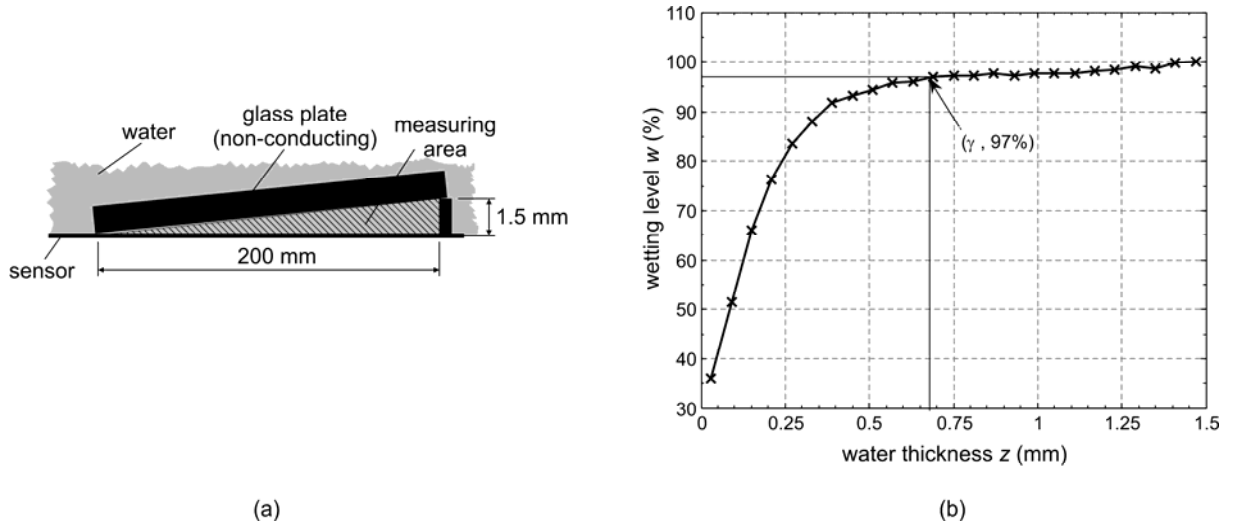


Figure 6.5: (a) Experimental setup for the depth sensitivity estimation. (b) Wetting level response for different water thickness over the sensor surface.

There is no strict definition of penetration depth. Therefore the penetration depth γ_{97} of the sensor was defined as the liquid thickness producing a signal level which

represents 97% of the asymptotic value ($w = 1$), i.e. the value for the case the thickness is infinite. In this way,

$$\frac{V(z = \gamma_{97})}{V(z = \infty)} = 0.97 \quad , \quad (6.5)$$

where z is the water thickness across the sensor. By using interpolation of the measured data, one obtains a value of $\gamma_{97} = 0.69$ mm. This value denotes the maximal liquid thickness which influences the measurements at a planar sensor.

Similar accuracy, noise and depth sensitivity results have also been obtained in the evaluation of the sensor of Figure 6.2 having smaller interdigital structures. Since they are quite similar to the values obtained in this section, these results are omitted here and the reader is referred to Da Silva *et al.* (2008).

6.3.4 Measurement of a buoyancy-driven flow

Buoyancy driven flow is often found in many engineering applications such as mixing process of fluids with different density. In nuclear reactors, fluid mixing induced by buoyancy effect is relevant for

- boron dilution issues, when highly borated water with different temperature mixes with the ambient water in the reactor pressure vessel,
- pressurized thermal shock scenarios, when cold emergency cooling water is injected into the reactor and is contacted with the vessel wall, and
- containment analysis, when in the case of severe accidents, hot hydrogen and steam mix with the containment atmosphere.

Especially the problems related to the fluid mixing of borated and unborated water has been the scope of investigation at FZD (Rohde *et al.* 2005; Prasser *et al.* 2003). In certain situations, when a lack of boron concentration occurs in the reactor, additional borated water is added to the core via an emergency injection system. This borated water has usually a colder temperature than the ambient coolant. Therefore, both the boron concentration and the temperature will affect the density difference of the fluids being mixed and therefore affect the mixing processes that occur in such situations. Thus, the degree of mixing of weakly and highly borated coolant is a critical issue with respect to the reactivity insertion into the reactor core. In this way,

understanding the impact of such phenomena can help in the design and operation of nuclear reactors.

The aim of the present study was to analyze the mixing processes related to the boron dilution problem for safety-relevant scenarios in reactors. A simple vertical test facility was constructed as nuclear reactor geometries are complex leading to the mixing processes that are not widely understood or where the influence of the buoyancy may not be significant.

a) *Experimental setup*

A vertical mixing test facility with simple geometry having rectangular cross section was designed and constructed (Figure 6.6). Five identical rectangular segments as described in Figure 6.1 are stacked together. Each segment is made of acrylic glass which is 500 mm wide by 625 mm high by 100 mm deep. The whole test section is 3.32 m high. A flow inlet is located in between segments 1 and 2, while an outlet is positioned in between segments 4 and 5. Segment number 2, right after the inlet, is instrumented with the planar sensor. In this region the most interesting mixing process occurs. The facility ensures that the gravity force acts along a significant length scale.

In order to visualize the mixing process of two liquids having different densities in a controlled manner, the following experiment was carried out. Water-glucose mixtures were used to produce density gradients. A glucose-water solution containing 6% glucose has a corresponding density of $1020 \text{ kg}\cdot\text{m}^{-3}$, i.e. 2% density difference to clean water. This is equivalent to about 60 K temperature difference. Furthermore, sodium chloride was added to the higher density water-glucose solution acting as tracer. In this way, the mixing process of clean water with the glucose-water solution can be monitored by means of the planar sensor. It has been shown that the conductivity measurement can be linked to the temperature or density gradients by (Prasser *et al.* 2003)

$$\theta(i, j, k) = \frac{\sigma(i, j, k) - \sigma_L}{\sigma_H - \sigma_L} \cong \frac{T(i, j, k) - T_L}{T_H - T_L} \cong \frac{\rho(i, j, k) - \rho_L}{\rho_H - \rho_L}, \quad (6.6)$$

where θ is called mixing scalar (assuming values between 0 and 1), σ is the measured conductivity, T temperature and ρ density. The subscripts H and L stand for the high and low values, respectively, which represent the parameter difference of the used liquids. In the experiment described below, clean water and water-glucose

solution having a conductivity of $60 \mu\text{S}/\text{cm}$ and $200 \mu\text{S}/\text{cm}$, respectively, were used. The execution of the experiment consists of few subsequent steps.

1. Clean water is added into the test section up to the bottom of segment 2.
2. Water-glucose solution is very slowly inserted from the bottom taking care not to mix both components. In this way, a layered structured is obtained having clean water in segments 1-2 and the more dense water-glucose solution in segments 3-5. This step ensures the formation of a well-defined initial condition which is very important for later comparison purposes with CFD simulations.
3. Finally, the mixing process is initiated by flowing water-glucose solution through the inlet with a constant flow rate of 0.35 L/s .

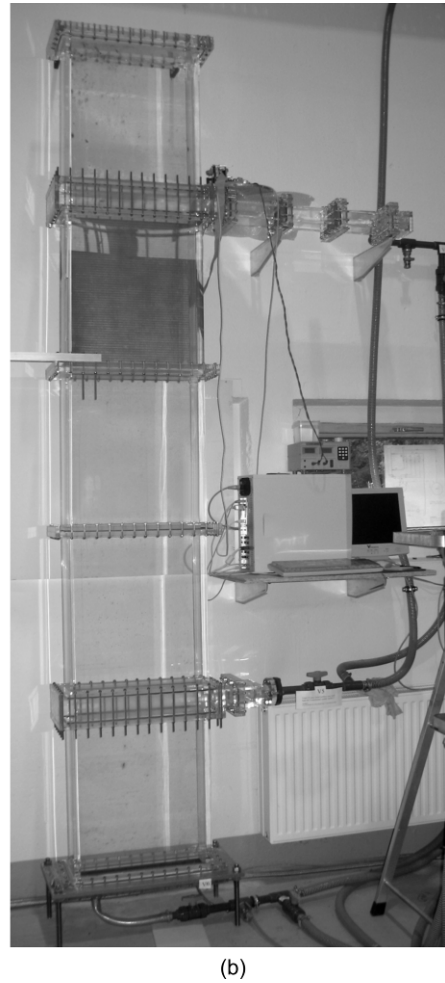
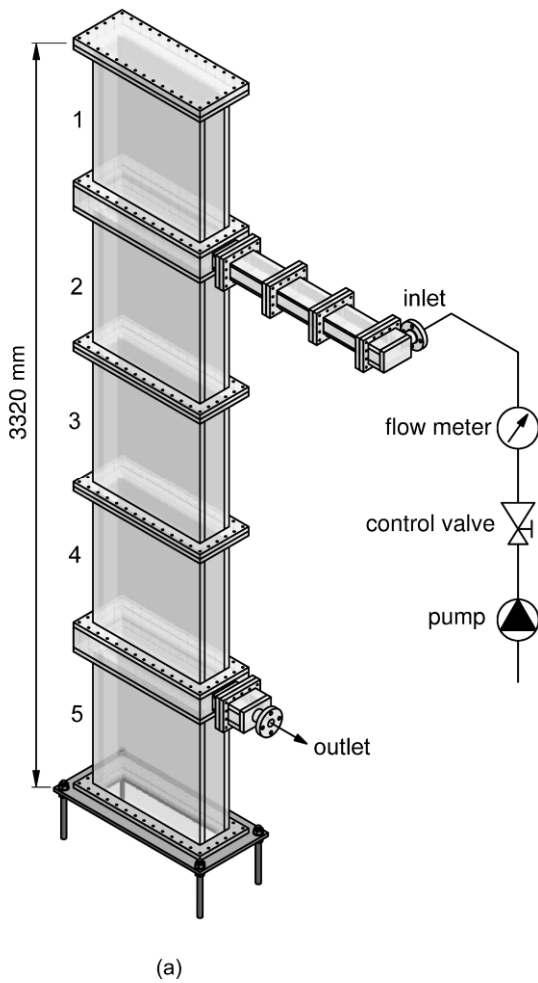


Figure 6.6: Schematic diagram (a) and photograph (b) of the test facility used in the buoyancy-driven flow experiment.

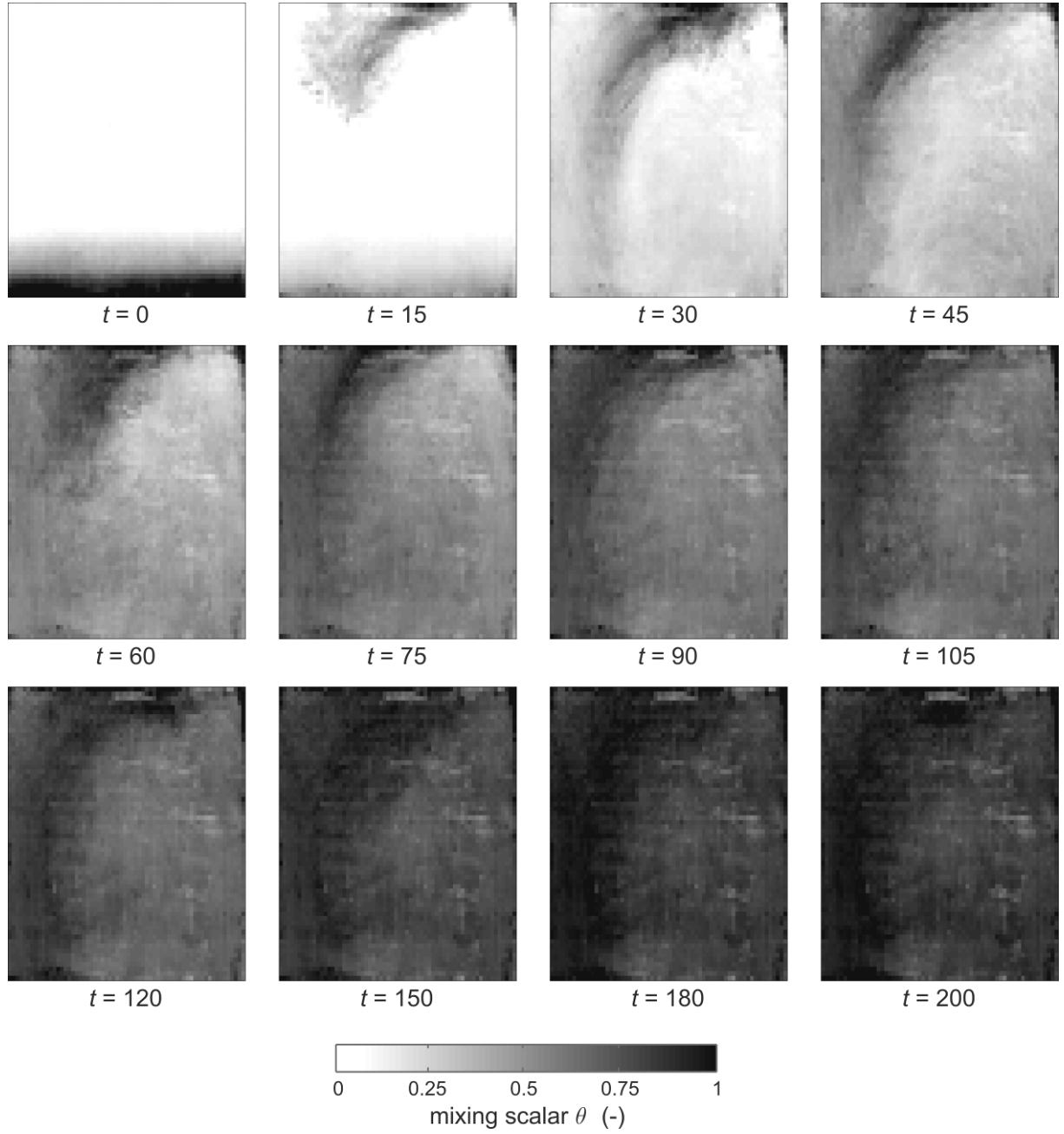


Figure 6.7: Instantaneous images of the mixing scalar θ . For details about the experiment see text.

b) Results

The mixing process was monitored with the planar sensor for 200 s at 300 fps. Since the process is rather slow the frame frequency could also be lowered. Figure 6.7 depicts 12 instantaneous mixing scalar θ distributions over the sensor surface. In the image for $t = 0$, the boundary between the two components and a transition region can be observed. As the water-glucose solution flows into the channel, the formation of a circular jet can be clearly seen. The subsequent images show the mixing of the

two substances. At the time $t = 200$ the mean value of the mixing scalar was $\theta = 0.92$, indicating an almost complete mixing. The further analysis of the image sequences may reveal additional details about the mixing behavior of two miscible liquids with different densities.

The main objective of such an experiment is to generate experimental data for the validation of CFD codes related to the influence of buoyancy in turbulence models. A preliminary analysis referring to this is presented by Vaibar *et al.* (2007). Later, other experiments with different flow rates and density gradients may be carried out and compared with CFD predictions.

6.3.5 Fluid distributions in a fluid coupling

Fluid couplings are widely employed as torque conversion elements in heavy load rotating drive systems and can be found in numerous technical systems such as power plants, naval vessels, railed vehicles, busses and trucks. Although there are many different designs of such couplings, the operation principle is the same. Figure 6.8 shows an elementary fluid coupling which consists of a metal housing and two bladed wheels, called pump and turbine. In such couplings, the mechanical input power at the pump impeller is converted into kinetic energy in the working fluid, and then reconverted into mechanical energy in the turbine. The inherent speed difference between turbine and pump wheels is quantified by the so-called slip s which is defined according to

$$s = 1 - \frac{\omega_T}{\omega_P} , \quad (6.7)$$

where ω is the rotational speed and the subscripts T and P denote turbine and pump, respectively.

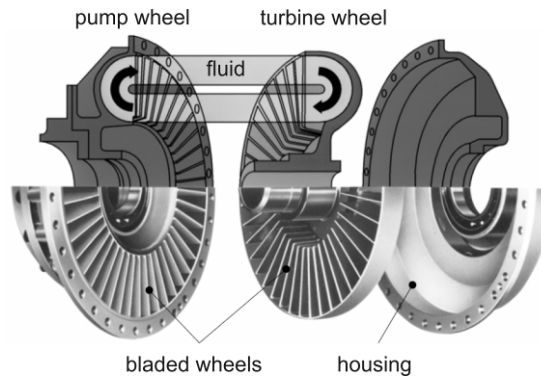


Figure 6.8: Mechanical assembly and functional principle of a fluid coupling.

The power transmission characteristics of fluid couplings are highly influenced by the fluid flow structure inside the coupling. The experimental investigation of the flow characteristics inside a fluid coupling during operation is thus of great importance for the optimization of static and transient behavior of those devices (Höller 2000). However, so far it has been considered as impossible to perform measurements on running fluid couplings due to their complex design as well as fast rotational speed.

As an initial step towards the experimental investigation of fluid couplings, the planar sensor technology was adapted to the measurement of two-phase flow patterns in a blade channel of a fluid coupling during regular operation. In the following sections, the experimental setup and some initial results are presented and discussed.

a) Experimental Setup

Experiments on a fluid coupling were carried out in the coupling test field of Voith Turbo in Crailsheim, Germany. The coupling used in the experiments is a special test coupling with a profile diameter of 422 mm which operates with water and has some deviations from a standard design. Both shafts of the coupling extend to one side, which is achieved by a hollow pump shaft enclosing the axial turbine shaft. This gives full access to the coupling from one side and, thus, facilitated the mounting of the electronics on the pump wheel. Both shafts are driven independently by two speed-controlled electric motors. In this way, the rotational speed of the pump and turbine and thereby the slip rate can be adjusted.

Two half-moon sensors (Figure 6.2) were mounted on the pressure-side and the suction-side walls of a blade channel inside a test coupling (Figure 6.9). Two sensors are required in order to visualize the flow at the two blade walls, pressure side wall (upon which liquid is pushed by the tangential force), and the suction side wall (from which liquid escapes by the action of tangential forces). Since it was technologically easier, the sensors were mounted into different blade channels. This has no impact on the measurement results since, due to symmetry, the flow can be considered being similar in different channels.

A modified version of the conductivity-based electronics discussed in section 6.3.1 was used for such measurements. A major revision of the planar sensor electronics was required to meet the requirements imposed by the conditions of a running fluid coupling. The electronics have to be small, compact, and also able to rotate with the coupling wheel. To comply with those constraints, the electronics was conceived (i) to

be supplied by a battery, (ii) to contain enough memory to save the measured data acquired during operation, and (iii) to be controlled by a wireless link. Thus, the whole system is fully autonomous. A detailed system description and evaluation can be found in Da Silva *et al.* (2008).

Figure 6.9 shows some photos of the setup, where the pump wheel of the test coupling with two mounted sensors as well as the developed electronics attached to the pump side can be seen. A metal cover (not shown in the figure) enclosed the electronics for safety reasons during the experiments.

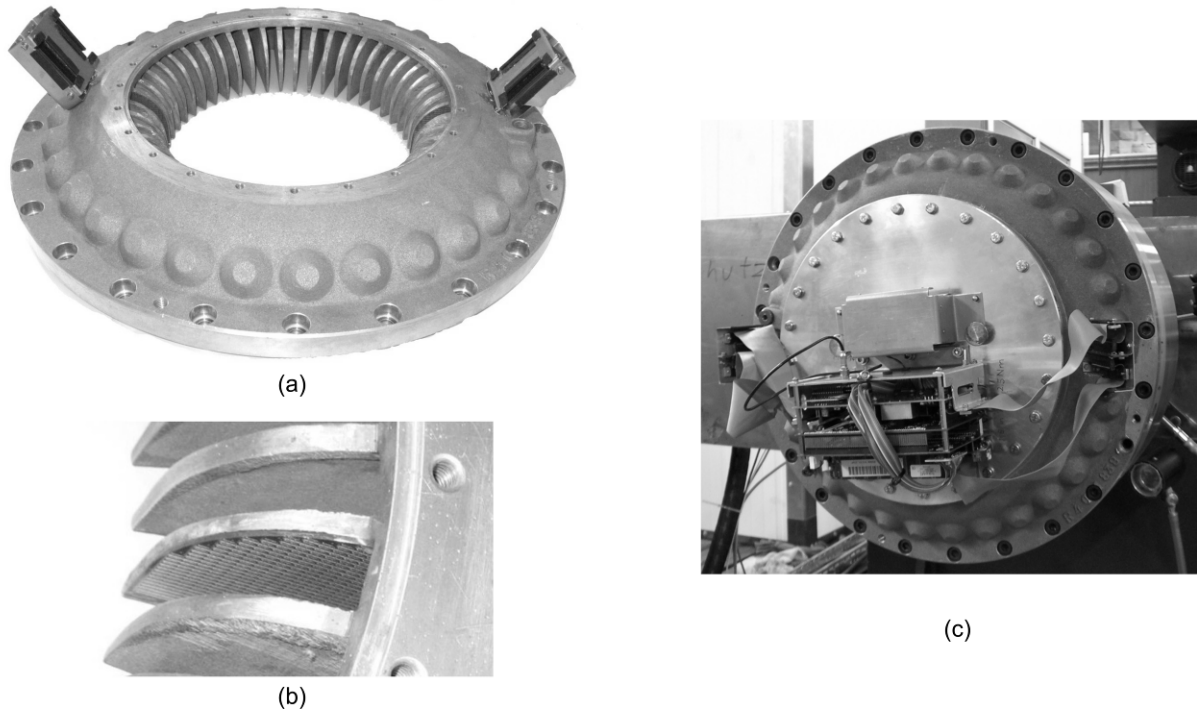


Figure 6.9: (a) Surface sensors mounted on the wall of a blade channel. The metallic fixations outside the coupling serve as protection and mechanical stability for the cables connecting the sensor with the electronics. (b) Detail view of one blade channel. (c) Measurement electronics mounted on the test coupling without the metal cover.

b) Results

Measurements with the new sensor system were performed in the test coupling during regular operation. The experiments were run with pump rotational speed of 790 rpm while the turbine speed was set for two conditions, namely 790 rpm and 474 rpm, i.e. at slip rates of 0% and 40%. Furthermore, the coupling was operated at a partial filling of 80% and the planar sensor electronics was set up for acquiring images at 10 000 fps.

Figure 6.10a shows two exemplary images of instantaneous liquid distributions at slip rates of 0% and 40% for the pressure and suction-side sensors. The images show the wetting level w . It was calculated from (6.4) using as reference value a measurement taken prior to begin of the experiment, whereby the sensor was completely covered by water. At zero slip, a steady flow condition is established. The liquid level is parallel to the rotation axis and the phase transition between air and water is very sharp. For an increased slip value, the liquid level moves into a diagonal position and the phase boundary starts oscillating. In Figure 6.10b the raw images for the slip condition of 40% were processed and fitted in an illustration of a blade channel to give an idea of the real condition inside the coupling. In order to show the high-speed capability of the system, a sequence of successive images of the pressure-side sensor for a slip rate of 40% is depicted in Figure 6.11. A water wave can be clearly observed moving along the sensor in the direction indicated by the arrow in the first picture. Note that only every 20th image from the data acquired at 10 000 fps is shown in the figure.

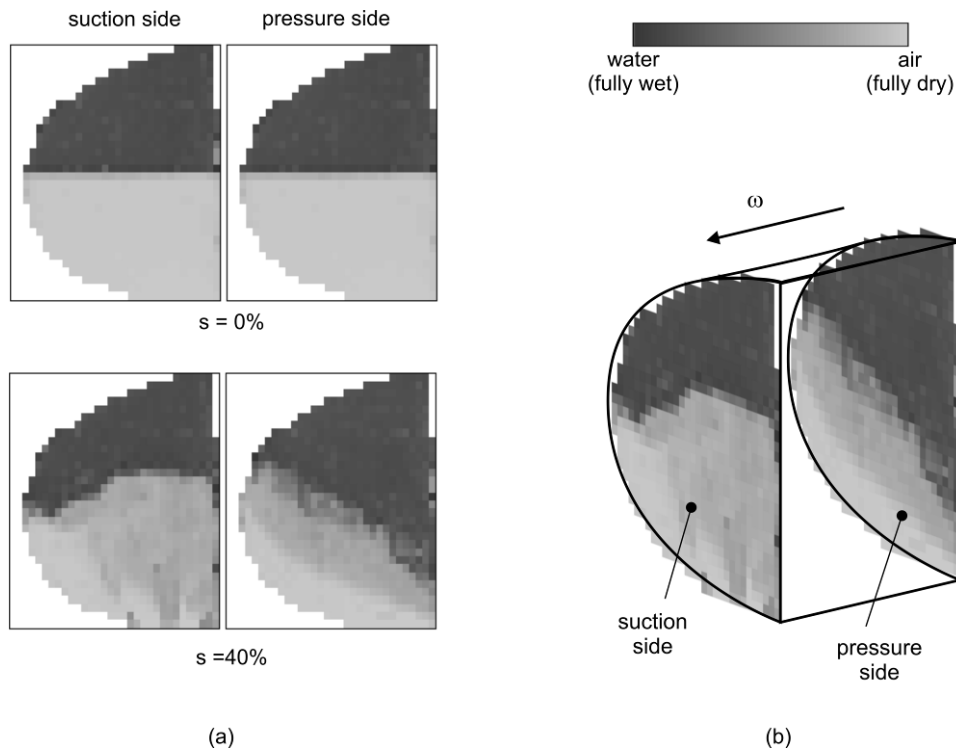


Figure 6.10: (a) Selected instantaneous liquid distribution images for the pressure and suction-side blade walls at the indicated slip values for the test coupling. For operating conditions see text. The right images display the liquid distribution at the suction side and the left image at the pressure side. (b) Exemplary images obtained from the suction and pressure-side sensors and illustration of a blade channel with the images fitted in it for $s = 40\%$.

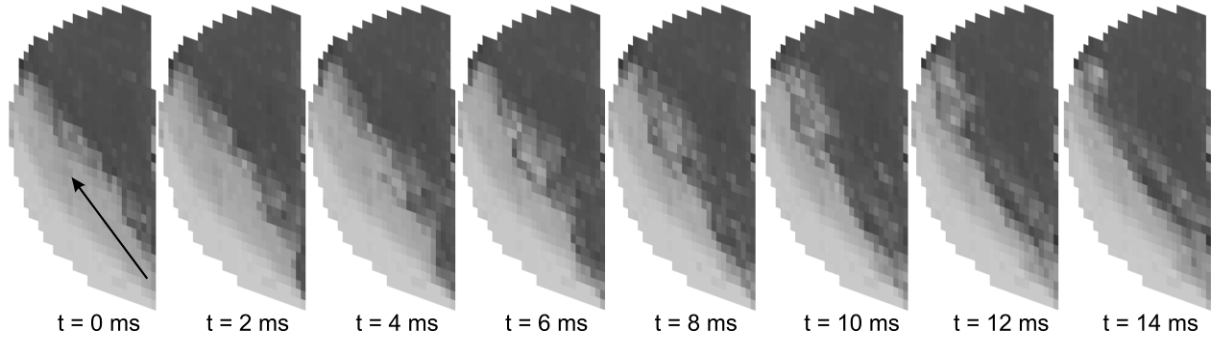


Figure 6.11: Sequence of successive images of pressure-side sensor obtained for $s = 40\%$ which shows some details, such as droplet impinging on the sensor and a water wave moving along it. The arrow indicates the wave direction. Only every 20th image from the acquired data at 10 000 fps is shown.

A primary objective of the work described in this section was to present a new tool for high-speed time-resolved investigation of the fluid distribution in the coupling wheel channels. The data produced by the planar sensor may help to improve the understanding of the behavior of industrial couplings. In addition, these data may also be used to validate theoretical models of flow processes and computational simulations of current couplings or to support the design of new couplings.

6.4 Permittivity-based planar sensor

6.4.1 System description

The electronics used to operate the planar sensor is based on a capacitance wire-mesh sensor (see section 5.2.1) and is briefly described below. The block diagram of the electronics for an exemplary sensor with 32×32 electrodes configuration as well the time diagram of the excitation signals are shown in Figure 6.12. For a detailed system description and evaluation see Thiele *et al.* (2008). The time-multiplexed excitation and measurement scheme is also used here. The transmitter electrodes are successively connected to a sinusoidal voltage while the transmitter electrodes are measured in parallel. When all 32 transmitter electrodes have been activated and all sensing blocks have been sampled, one obtains a matrix of 1 024 elements with values corresponding to the distribution of the capacitance (permittivity) over the sensor surface. From the data matrix, an image can be easily achieved without any reconstruction algorithm. A data logger with 512 Mbyte storage capacity is connected

via USB interface to a computer, where the digitized data are processed and visualized. A microcontroller controls the excitation and acquisition signals timing as well as the frequency of excitation voltage. The electronics is able to produce up to 10 000 fps for a sensor with 32×32 sensing structures.

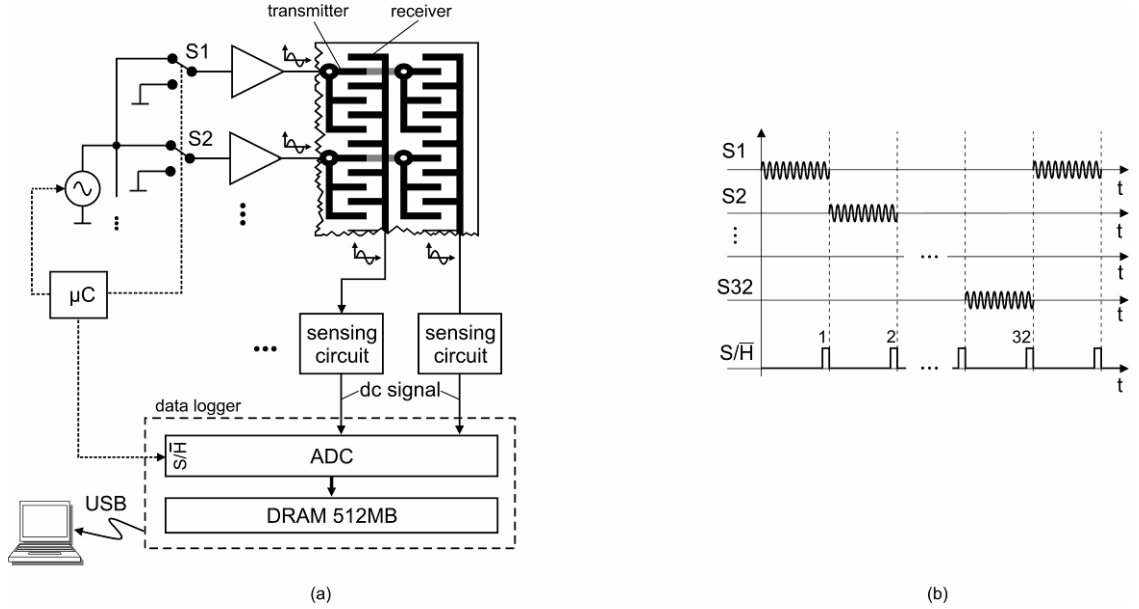


Figure 6.12: (a) Block diagram of capacitance planar sensor system. (b) Temporal excitation scheme of the transmitter electrodes S1 to S32 with sinusoidal voltage excitation and the point of digitalization with an ADC controlled by the sample-and-hold signal.

6.4.2 Permittivity measurement

The auto-balancing bridge method was employed to measure the capacitance of the interdigital sensing structures. An equivalent circuit for one sensing structure is shown in Figure 6.13. The same structure as in the capacitance wire-mesh sensor has been maintained (see section 5.2.1), except that a signal conditioning block was included in order to adapt the signal levels to the new capacitance range of the planar sensor. The sensing circuit is formed by three basic stages which are described as follows. The auto-balancing bridge which has its voltage output proportional to the unknown capacitance (permittivity) according to

$$V_x = -V_i \cdot \frac{C_x}{C_f}, \quad (6.8)$$

when the feedback network of the opamp, C_f and R_f , are so dimensioned that the auto-balancing bridge circuit is made capacitance dominant (for a complete discussion see 5.2.1). As previously mentioned, the circuit is immune to stray capacitances C_{s1} and C_{s2} . Referring to (3.22), the capacitance at each sensing structure C_x is directly proportional to the permittivity ϵ_x of the fluid

$$C_x = k_g \epsilon_0 \epsilon_x \quad (6.9)$$

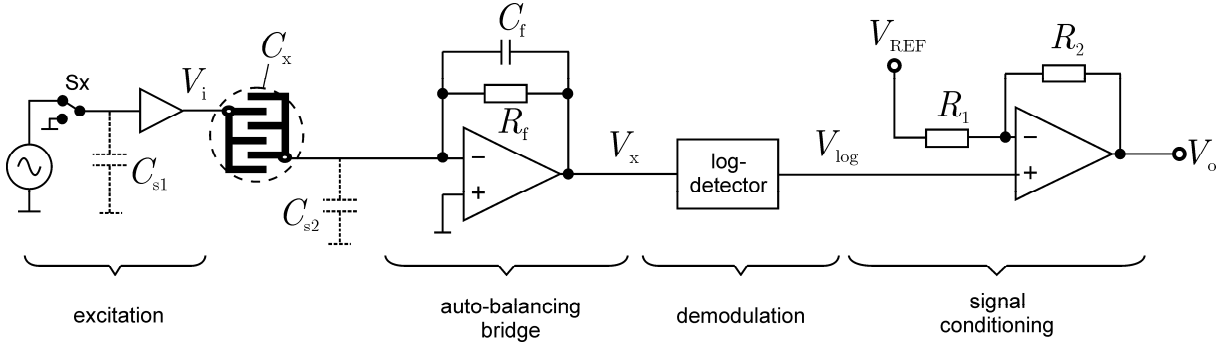


Figure 6.13: Equivalent one-channel circuit for measuring the permittivity.

Hence, from (6.8) and (6.9), V_x is also proportional to the permittivity of the fluid over the interdigital sensor. The second stage, a logarithmic detector IC (AD8307) demodulates the sine-wave opamp's output voltage, i.e. converts it into a proportional dc voltage. Its transfer function is given by

$$V_{\log} = V_a \cdot \ln \left(\frac{V_x}{V_b} \right), \quad (6.10)$$

where V_a , V_b are constants of the integrated circuit. Before being digitized the voltage V_{\log} passes a conditioning block, which removes the dc offset introduced by the log detector and scales it for the full ADC range (0...5 V). The conditioning block has the following transfer function

$$V_o = V_{\log} \left(\frac{R_1 + R_2}{R_1} \right) - V_{\text{REF}} \frac{R_2}{R_1}, \quad (6.11)$$

where R_1 and R_2 and V_{REF} are constants. Combining equations (6.8) to (6.11) it can be shown that

$$V_o = a \cdot \ln(\varepsilon_x) + b, \quad (6.12)$$

where a and b are constants that encompass all the circuit constants. Consequently, the measured voltage V_o effectively represents the permittivity of the sensing structures. The logarithmic response assures the measurement of even very small permittivity values.

Due to small intrinsic differences of the employed ICs and tolerances in resistor and capacitor values, there is a variance in the measured voltage over all measurement channels. Thus, calibration of these channels is necessary to achieve reliable output readings. A similar calibration routine as described in section 5.2.2 must be performed and is shortly described below.

For the calibration routine, first the surface sensor is fully covered with a substance of low permittivity ε_L , in most cases air $\varepsilon_L = 1$, and the data matrix V_o^L is acquired for all sensing structures i and j . Usually average values over a definite time are used to reduce the influence of noise. A second data matrix V_o^H is acquired for the situation the sensor is covered with a substance of high permittivity ε_H . In the case that the lower permittivity reference substance is air with $\varepsilon = 1$, the calculation of ε_x simplifies to (section 5.2.2)

$$\varepsilon_x(i, j, k) = \exp\left(\frac{V_o(i, j, k) - V_o^L(i, j)}{V_o^H(i, j) - V_o^L(i, j)} \ln(\varepsilon_H)\right). \quad (6.13)$$

6.4.3 System evaluation

a) Measurement uncertainty

A similar approach as described in section 6.3.3 for the evaluation of the conductivity-based system was also applied. The sensor used for the experimental evaluation is shown in Figure 6.14. The geometry of the interdigital structure is the same as for the sensor of Figure 6.2, but a rectangular sensor geometry was used. An acrylic box of 35 mm height is mounted around the sensing area serving as vessel for the liquids to be investigated.

First, the system was evaluated regarding accuracy, where five different substances and air (empty sensor) in a permittivity range from 1 to 80 were measured. The reference permittivity values ε are listed in Table 6.1. For each substance, 10 frames were acquired at 10 kHz and an average value was taken to reduce random noise.

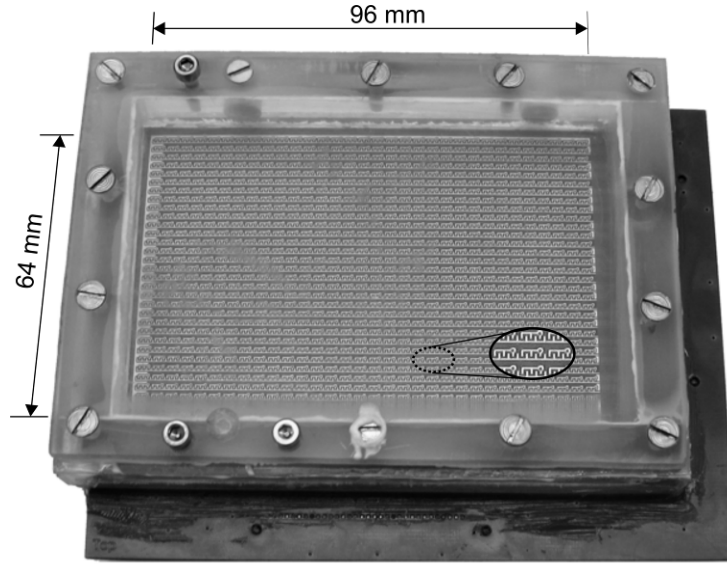


Figure 6.14: Planar array sensor employed for the experimental evaluation of the permittivity-based electronics. The size of interdigital structures is $2 \text{ mm} \times 3 \text{ mm}$.

Figure 6.15a shows the measured voltage values V_o for all substances analyzed. Each cross in the figure represents the value obtained for one interdigital structure. Measured points belonging to the same interdigital structure were connected by means of straight lines. As the figure displays a semi-logarithmic plot, the relationship between measured voltage and permittivity appears as linear functions, as predicted from (6.12). In principle, there are 1 024 different lines. One can also easily indentify the variations in the measured voltages for the measurements at the same substance. A deviation of up to 36% from minimum to maximum value is encountered. As stated earlier, these variations are caused by the differences in the characteristic of each transmitter-receiver pair which can be compensated by a calibration routine.

Table 6.1: Substances analyzed for the evaluation of sensor accuracy. Reference relative permittivity values were taken from Lide (2005).

substance	relative permittivity (-)
air	1.0
oil	2.1
isopropanol	20.1
ethanol	25.1
ethylene glycol	40.3
deionized water	79.9

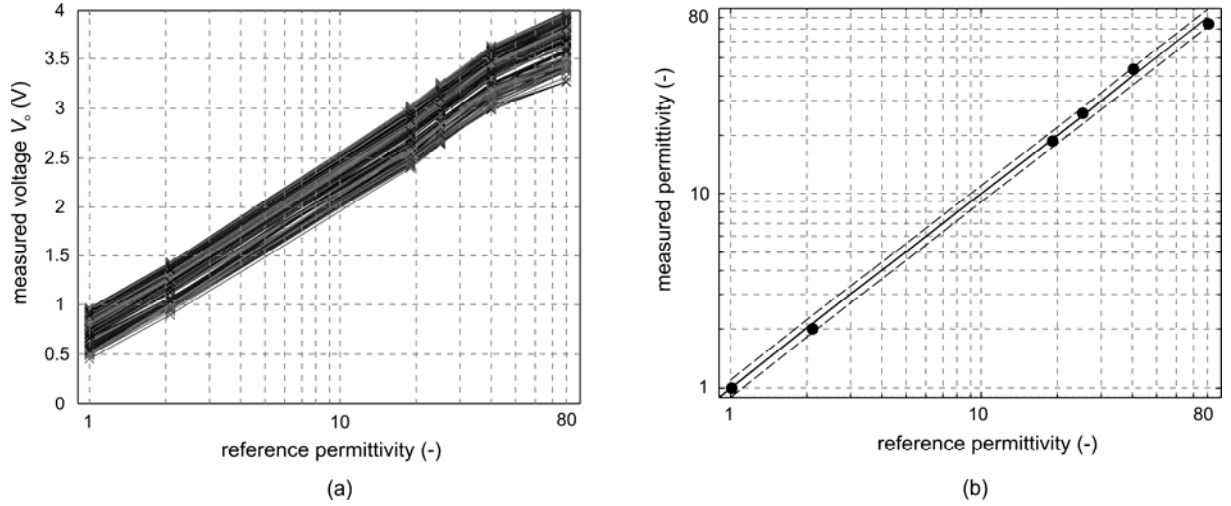


Figure 6.15: Results for the measurement of different substances in a relative permittivity range of 1 to 80. (a) Measured voltages. (b) Permittivity values calculated with (6.13) in comparison with reference ones. Dotted lines represent a $\pm 10\%$ deviation line.

The calibration procedure described in the previous section was applied to the measured voltages in order to estimate the measured permittivity values. Figure 6.15b illustrates the results of the measured permittivity compared with reference ones. The graphic was plotted in a log-log scale to emphasize the good linearity even for small permittivity values. All measured relative permittivity values fall within the 10% deviation lines (dashed lines). The size of error bars in the figure is of the same magnitude of the symbols and therefore error bars are only roughly recognized. They represent the maximal deviation of measured permittivity within one substance. The highest value found was 3.3% for water.

The system was also investigated regarding instrumental noise. The surface sensor was fully covered with isopropanol. The standard deviation of the measured permittivity over the 1 000 frames at a repetition rate of 5 kHz was taken to estimate the instrumental noise. A maximal value of the standard deviation over all sensing structures of 0.97% was obtained. This value is much lower than the obtained accuracy as described above and can therefore be neglected.

b) Depth sensitivity

An important parameter for the correct interpretation of the images generated by the planar sensor is the determination of the depth sensitivity. For this purpose a similar procedure as described in section 6.3.3b) was applied. An electrically non-conducting

polyvinyl chloride plate ($\varepsilon = 4$) is placed across the sensor in such a way that an inclined plane is created. This assembly was immersed in ethanol ($\varepsilon = 25$) which resulted in a liquid film of continuously increasing thickness on the sensor surface (compare Figure 6.5a). The plate was covering the whole sensitive area of the sensor. Ten frames at 5 kHz were acquired and averaged. From the measured voltage values the wetting levels for all sensing structures were computed by

$$w(i, j) = \frac{V_o(i, j) - A_p(i, j)}{E(i, j) - A(i, j)}, \quad (6.14)$$

where $A(i, j)$ denotes a reference measurement of air (or empty sensor), $A_p(i, j)$ a further reference measurement with the plate placed over the sensor in the same configuration as described above, but without liquid, and finally $E(i, j)$ a reference measurement when the sensor was fully covered by ethanol without the plate. Note that (6.14) is a modified version of (6.4). In the numerator of (6.14), the influence in the measured voltages caused by the presence of the plate is eliminated. The denominator is a reference value to determine the wetting level. Since air has a permittivity of one and already produces voltage readings at sensor output, those values are subtracted from the ethanol reference. In this fashion, only the liquid portion of the signal is evaluated in (6.14).

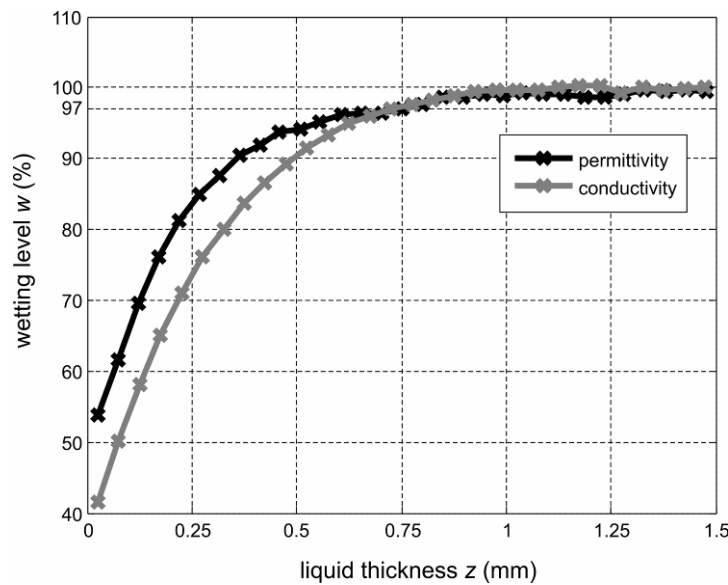


Figure 6.16: Wetting level as a function of liquid film thickness obtained in the experimental evaluation of depth sensitivity for the planar sensor of Figure 6.14 being operated by the conductivity-based as well as by the permittivity-based electronics.

The mean values over the 8 central rows with varying wetting level are depicted in Figure 6.16. For comparison purposes, the depth sensitivity of the planar sensor was also determined from measurements with the conductivity-based electronics by the same procedure as described in section 6.3.3b). The resulting wetting level values w are shown in Figure 6.16 as well. Both curves show similar behavior, an exponential rise to a maximum, corroborating with previous analysis (section 6.3.3b), Li *et al.* 2006). The values from the permittivity measurements are slightly higher than the conductivity ones in the lower range of thickness values. This small disagreement may be explained by the influence of the polyvinyl chloride plate which was not fully eliminated in (6.14). However, it is expected that the both curves would be identical, if the permittivity value of the plate were $\varepsilon = 1$. The penetration depth was again defined as the thickness value for which the wetting level reaches the value of 97%. In spite of the small deviation of both curves in Figure 6.16, penetration depth was found $\gamma_{97} = 0.75$ mm for both measurements. This value represents the maximal liquid thickness which influences the measurements at the planar sensor.

6.4.4 Two substances mixing measurement

To show the capability of the surface sensor in investigating transient flow phenomena, a simple mixing experiment of two non-conductive fluids was carried out. The planar sensor with attached acrylic box (Figure 6.14) was used in this experiment. The liquids could be introduced into the vessel by a small opening. Further, the sensor was tilted about 40° . For simplicity reasons the images obtained will be displayed horizontally so that the liquid level will appear inclined.

The initial condition for the mixing experiment was obtained by firstly filling the vessel with 40 mL isopropanol ($\varepsilon = 20.1$) and then by very carefully introducing 40 mL of benzene ($\varepsilon = 2.0$) to avoid the pre-mixing of both fluids. The upper part of the sensing area was left empty (air). Calibration measurements as described in section 6.4.2 were carried out using isopropanol and air before the execution of the mixing experiment. From the initial stratified condition, the both liquids were brought into motion by simple agitation of the sensor box for 10 s. The permittivity value distribution over the sensor surface was monitored for 15 s at the repetition rate of 1 kHz. Some selected images of the calibrated data by (6.13) are shown in Figure 6.17, where the dynamic mixing process can be observed. At $t = 0$ a three-layer stratified structure formed by isopropanol, benzene and air can be easily

recognized. The interfaces air-benzene and benzene-isopropanol are correctly captured by the sensor and the fast transition is an indication of low crosstalk between the sensor structures. Any crosstalk would have caused a smearing of the imaging of the inter-phase surface. At $t = 15$ s both liquids are fully mixed. The upper images in Figure 6.17 show further two instantaneous distributions. The whole mixing process is rather turbulent and occasionally some structures like waves or jets can be identified. The lower images depict the temporal evolution of one exemplary jet with a time resolution of 10 ms, i.e. only every tenth image is shown. Thus, the acquisition frequency used is sufficient for the investigation of this mixing process.

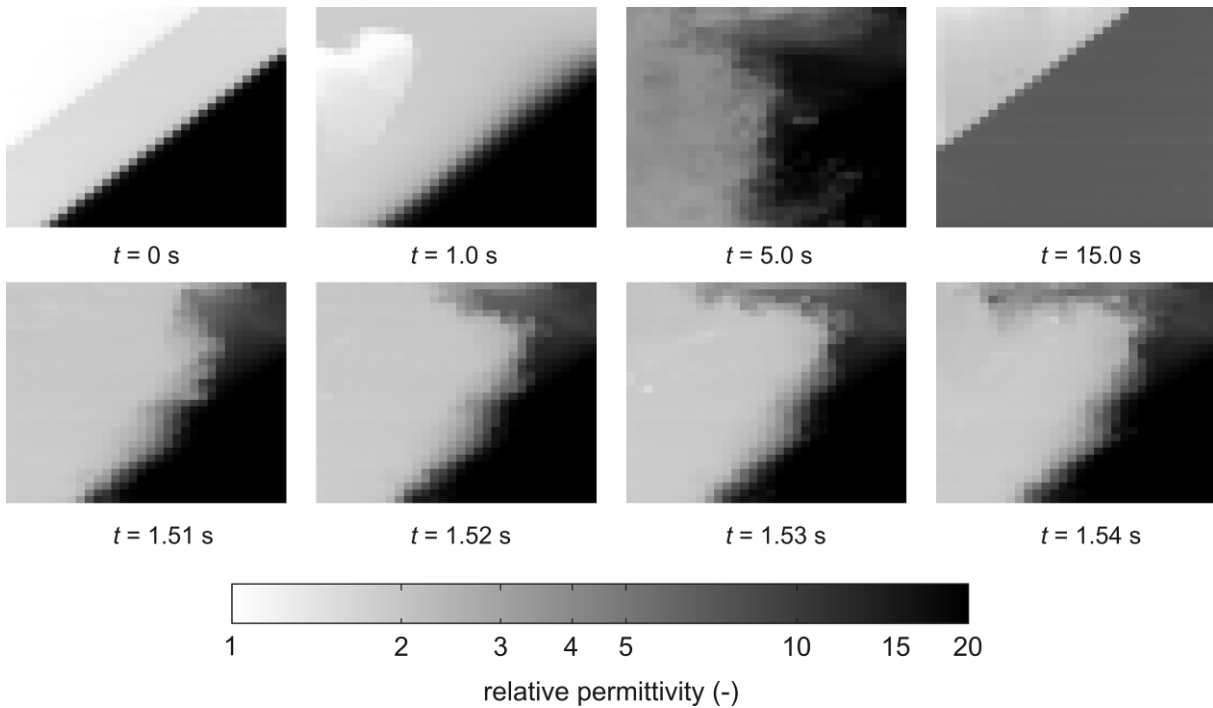


Figure 6.17: Images of a two-component mixing experiment. At $t = 0$ (initial condition) a three-layer stratified structure formed by isopropanol, benzene and air can be easily recognized. The following images show the mixing process caused by the agitation of the sensor box. At $t = 15$ s the complete mixing was reached.

After reaching the full mixing the measured mixture permittivity was $\varepsilon_m = 7.9$, which is obtained from the average value for the area covered by the liquid. Further, the final effective permittivity value of the mixture can be theoretically calculated with help of the Birchak formula (Birchak *et al.* 1974)

$$\sqrt{\varepsilon_m} = c_i \cdot \sqrt{\varepsilon_i} + (1 - c_i) \sqrt{\varepsilon_b} , \quad (6.15)$$

where c_i is the isopropanol concentration, ε_i and ε_b are the permittivities of isopropanol and benzene, respectively. The isopropanol concentration is obtained from the volume fractions of each liquid $c_i = 0.5$ ($= 40 \text{ mL}/80 \text{ mL}$). Since $\varepsilon_i = 20.1$ and $\varepsilon_b = 2.0$, from (6.15) the mixture permittivity is calculated to be 8.69. The measured value is very close to the theoretical value and the relative deviation of the measured permittivity is 9.1%.

6.5 Conclusions

A new sensor modality for the investigation of fluid flow phenomena has been developed and tested. The planar sensor comprises an array of interdigital sensors which are individually interrogated in a multiplexed manner at very fast repetition rate. The coplanar electrodes configuration allows the sensor to be placed on the wall of pipes or vessels and thus having a minimal influence on the flow.

The new sensor can be operated either with a conductivity-based electronics or a permittivity-based one. The planar sensor is able to detect phases or components in dynamic fluid flow. The electronics performs a two-dimensional measurement of an electrical parameter (conductivity or permittivity) of interdigital sensing structures, which effectively gives images of the instantaneous fluid distribution over the sensor surface.

Both systems are able to perform measurements at up to 10 000 fps which allows the investigation of highly transient flows. Both electronics present good accuracy and low noise even at rather high measuring frequencies. The depth sensitivity has been also experimentally determined showing results compatible with other studies. Besides the sensor characterization, a few flow measurement experiments were presented and discussed, thus indicating some application fields for the novel sensors.

Further work may encompass optimization of the interdigital electrode structure with help of electric field simulations to improve depth sensitivity or signal quality. Furthermore, the use of the presented sensors in similar flow problems is planned serving as basis for better understanding of such flows or as validation data base for CFD codes.

7 Conclusions

In this concluding chapter the main achievements of the thesis are summarized as well as some issues for future work are discussed.

7.1 Conclusions

The experimental investigation of multiphase flow is essential to the better understanding and optimization of processes and devices in many engineering applications. The measurement of multiphase flow also forms the basis for validation of models and simulations. In this work, impedance sensors for the measurement and imaging of gas-liquid multiphase flows were investigated and tested. Specifically three different sensor systems were developed, characterized with indications to measurement uncertainty, advantages and limitations, as well as applied in some potential applications.

The complex permittivity needle probe (Chapter 4) may be used for local multiphase flow measurement. It measures simultaneously and very fast the conductivity and permittivity values of fluids at the probe tip. It has been applied to measure oil-gas-water three-phase flow and also to monitor the mixing of two substances in a chemical reactor.

Cross-sectional images of a pipe flow can be obtained by means of the newly developed capacitance wire-mesh sensor (Chapter 5). It is a further development of current conductivity sensors. The range of substances, it may be applied to, is now not limited to conducting liquids. Maximal frame rates of 10 kfps have been reached, which places this sensor among the fastest imaging techniques. High spatial and temporal resolution images of gas-oil two-phase flow have been obtained. Furthermore, the sensor may also be applied for the investigation of three-phase flows, whereby initial measurements have shown promising results.

A new sensor modality was also presented within the work of this thesis. A planar array sensor was proposed to investigate fluid distributions along the surface of objects and near-wall flows (Chapter 6). It can be operated by a conductivity-based as well as permittivity-based electronics. In this way, a number of applications are possible. This sensor was successfully applied to investigate the liquid distribution inside a fluid coupling during regular operation rotating at 790 rpm, to the visualization of mixing process of scenarios relevant to nuclear safety, and to the visualization of mixing of two non-conducting liquids.

All sensor systems present high-speed capability thus being well suited for investigation of transient phenomena. The applications presented within this work are evidently not exhaustive, but serve as basis to the deployment of the developed sensor systems for future work.

The main contribution of this research work to the field of multiphase flow measurement technology is therefore the development, characterization and application of new sensors based on electrical impedance measurement. All sensors were optimized with respect to a very high measurement speed and two of them offer the capability for two-dimensional measurement (phase fraction imaging). The sensors are furthermore very robust and can easily be employed in a number of applications in research and industry.

7.2 Outlook

As already stated, the main task for the future is to employ the newly developed sensors for systematic investigation of flow phenomena or to search industrial applications for them. Nevertheless, for future research, it is interesting to have a closer look at following points.

- The needle probe may be provided with a miniature thermocouple thus generating a three-modality probe. Further, the temperature information may be used to compensate conductivity/permittivity readings.
- The exact spatial sensitivity distribution of a wire-mesh sensor, as described in section 5.3.3, may be taken into account in the image processing algorithm possibility leading to an improvement in the measurement accuracy.

- The capability and limitations of the use of the capacitance wire-mesh sensor for the investigation of three-phase flows should be carried on, as already started in section 5.5.3.
- Other geometries for the sensing structures of planar sensors may be investigated aiming to optimize signal sensitivity or penetration depth.
- The development of dual-modality electronics for wire-mesh and planar array may be investigated which perform simultaneous conductivity and permittivity measurements.

References

- Adrian, R.J. 1991 Particle-imaging techniques for experimental fluid mechanics. *Annual Review of Fluid Mechanics* **23** 261–304.
- Agilent 2006a *Basics of Measuring the Dielectric Properties of Materials*. Application Note, Agilent Technologies, June 2006. Available at: <<http://www.agilent.com>>
- Agilent 2006b *The Impedance Measurement Handbook*. Application Note, Agilent Technologies, July 2006. Available at: <<http://www.agilent.com>>
- Ahmed W.H. 2006 Capacitance sensors for void-fraction measurements and flow-pattern identification in air–oil two-phase flow. *IEEE Sensors Journal* **6** 1153–1163.
- Andreussi P., Di Donfrancesco A. and Messia M. 1988 An impedance method for the measurement of liquid hold-up in two phase flow. *International Journal of Multiphase Flow* **14** 777–785.
- Ansys, Inc. 2008 *Ansys CFX* [online]. [Accessed 10th March 2008]: <<http://www.ansys.com/Products/cfx.asp>>.
- Asali J.C., Hanratty T.J., and Andreussi P. 1985 Interfacial drag and film height for vertical annular flow. *AIChE Journal* **31** 895–902.
- Azzopardi B. 2006 *Gas-liquid Flows*. New York: Begell House.
- Azzopardi B.J., Hernandez Perez V., Kaji R., da Silva M.J., Beyer M., and Hampel U. 2008 Wire mesh sensor studies in a vertical pipe. In: *HEAT 2008, Fifth International Conference on Transport Phenomena in Multiphase Systems*, June 30 - July 3, Bialystok, Poland.
- Babelli I.M.M. 2002 In search of an ideal multiphase flow meter for the oil industry. *The Arabian Journal for Science and Engineering* **27** 113–126.
- Baker R.C. 2000 *Flow Measurement Handbook: Industrial Designs, Operating Principles, Performance, and Applications*. Cambridge, UK: Cambridge University Press.

- Barnea D. 1987 A unified model for predicting flow-pattern transitions for the whole range of pipe inclinations. *International Journal of Multiphase Flow* **13** 1-12.
- Bauckhage K. 1996 Gleichzeitige Erfassung von Partikelmerkmalen und Eigenschaften mehrphasiger Strömungen mit Hilfe der Phasen-Doppler-Anemometrie. *Chemie Ingenieur Technik* **68** 253-266.
- Bera S.C. and Chattopadhyay S. 2003 A modified Schering bridge for measurement of the dielectric parameters of a material and the capacitance of a capacitive transducer. *Measurement* **33** 3-7.
- Bertola V. 2003 Two-phase flow measurement techniques, p. 281-323. In: *Modeling and Experimentation in Two-Phase Flow*, Bertola V. (ed) New York: Springer.
- Bieberle M., Fischer F., Schleicher E., Hampel U., Koch D., Aktay K.S.C., Menz H.-J., and Mayer H.-G. 2007 Ultrafast limited-angle-type x-ray tomography. *Applied Physics Letters* **91** 123516.
- Birchak J.R., Gardner C.G., Hipp J.E., and Victor J.M. 1974 High dielectric-constant microwave probes for sensing soil-moisture. *Proceedings of the IEEE* **62** 93-98.
- Bode H.W. 1959 *Network Analysis and Feedback Amplifier Design*. New York: Van Nostrand.
- Boyer C, Duquenne A.M., and Wild G. 2002 Measuring techniques in gas-liquid and gas-liquid-solid reactors. *Chemical Engineering Science* **57** 3185-3215.
- Brennen C.E. 2005 *Fundamentals of Multiphase Flow*. New York: Cambridge University Press.
- Bröder D. and Sommerfeld M. 2002 An advanced LIF-PLV system for analysing the hydrodynamics in a laboratory bubble column at higher void fractions. *Experiments in Fluids* **33** 826-837.
- Brückner F. 2005 *Impedanzmessung mehrphasiger Fluide*. Diploma Thesis, Hochschule für Technik und Wirtschaft, Dresden, Germany.
- Bruuns H.H. 1995 *Hot Wire Anemometry. Principles and Signal Analysis*. New York: Oxford University Press.
- Buckley F. and Maryott A.A. 1958 *Tables of Dielectric Dispersion Data for Pure Liquids and Dilute Solutions*. U.S. Dept. of Commerce, National Bureau of Standards, Circular 589, 1958, USA.
- Cao Z., Wang H., Yang W.Q., and Yan Y. 2007 A calculable sensor for electrical impedance tomography *Sensors and Actuators A* **140** 156-161.

- Carey S.J., McCann H., Hindle F.P., Ozanyan K.B., Winterbone D.E., and Clough E. 2000 Chemical species tomography by near infra-red absorption. *Chemical Engineering Journal* **77** 111-118.
- Cartellier A. and Achard J.L. 1990 Local phase detection probes in fluid/fluid two-phase flows. *Review of Scientific Instruments* **62** 279-303.
- Ceccio S.L. and D.L. George 1996 A review of electrical impedance techniques for the measurement of multiphase flows. *Journal Fluids Engineering* **118** 391-399.
- Chanson H. 2002 Air-water flow measurements with intrusive phase-detection probes. Can we improve their interpretation? *Journal of Hydraulic Engineering* **128** 252-255.
- Chaouki J., Larachi F., and Dudukovic M.P. 1997 Noninvasive tomographic and velocimetric monitoring of multiphase flows. *Industrial and Engineering Chemistry Research* **36** 4476-4503.
- Comsol AG 2008 *COMSOL - Multiphysics Modeling* [online]. [Accessed 10th March 2008]: <<http://www.comsol.com/>>
- Corneliussen S., Couput J.-P., Dahl E., Dykesteen E., Frøysa K.-E., Malde E., Moestue H., Moksnes P., Scheers L., and Tunheim H. 2005 *Handbook of Multiphase Flow Metering, Rev.2*, The Norwegian Society for Oil and Gas Measurement and The Norwegian Society of Chartered Technical and Scientific Professionals. Available at: <<http://www.nfogm.no>>
- Costigan G., and Whalley P.B. 1997 Slug flow regime identification from dynamic void fraction measurements in vertical air-water flows. *International Journal of Multiphase Flow* **23** 263-282.
- Crowe C.T. (ed) 2006 *Multiphase Flow Handbook*. Boca Raton, FL: Taylor & Francis.
- Da Silva M.J., Lu Y., Sühnel T., Schleicher E., Thiele S., Kernchen R., and Hampel U. 2008 Autonomous planar conductivity array sensor for fast liquid distribution imaging in a fluid coupling, *Sensors and Actuators A* **147** 508-515.
- Da Silva M.J., Schleicher E., and Hampel U. 2007a A novel needle probe based on high-speed complex permittivity measurements for investigation of dynamic fluid flows. *IEEE Transactions on Instrumentation and Measurement* **56** 1249-1256.
- Da Silva M.J., Schleicher E., and Hampel U. 2007b Capacitance wire-mesh sensor for fast measurement of phase fraction distributions. *Measurement Science and Technology* **18** 2245-2251.

- Da Silva M.J., Sühnel T., Schleicher E., Vaibar R., Lucas D., and Hampel U. 2007c Planar array sensor for high-speed component distribution imaging in fluid flow applications. *Sensors* **7** 2430-2445.
- Da Silva M.J., Schleicher E., and Hampel U. 2005 Neue Konzepte für die kombinierte Leitfähigkeits- und Impedanzmessung in hochtransienten Mehrphasenströmungen. In: *Proceedings of 7. Dresdner Sensor-Symposium*, p. 139-142, Dresden, Germany, December 2005.
- Delhay J.M., Giot M., and Riethmuller M.L. 1981 *Thermohydraulics of Two-Phase Systems for Industrial Design and Nuclear Engineering*. New York: McGraw Hill.
- Dorf R.C. (ed) 2000 *The Electrical Engineering Handbook* Boca Raton: CRC Press LLC.
- Dudlik A., Schönfeld S.B.H., Schlüter S., Fahlenkamp H., and Prasser H.-M. 2002 Prevention of water hammer and cavitation hammer in pipeline systems. *Chemical Engineering and Technology* **2** 888-890.
- Dyakowski T. 1996 Process tomography applied to multi-phase flow measurement *Measurement Science and Technology* **7** 343-353.
- Dyakowski T., Jeanmeure L.F.C., and Jaworski A.J. 2000 Applications of electrical tomography for gas-solids and liquid-solids flows - a review. *Powder Technology* **112** 174-192.
- Dyakowski T., Hale J.M., Jaworski A., White N.M., Nowakowski A., Meng G., and Rwifa S. 2005 Dual-modality probe for characterization of heterogeneous mixtures. *IEEE Sensors Journal* **5** 134-138.
- Dykesteen E., Hallanger A., Hammer E., Samnoy E., and Thorn R. 1985 Non-intrusive three-component ratio measurement using an impedance sensor. *Journal of Physics E: Scientific Instruments* **18** 540-544.
- Elkow K.J. and Rezkallah K.S. 1996 Void fraction measurements in gas-liquid flows using capacitance sensors. *Measurement Science and Technology* **7** 1153-1163.
- Falcone G., Hewitt G.F., Alimonti C., and Harrison B. 2002 Multiphase flow metering: Current trends and future developments. *Journal of Petroleum Technology* **54** 77-84.
- Fluent, Inc. 2008 *CFD Flow Modeling Software & Solutions from Fluent* [online]. [Accessed 10th March 2008]: <<http://www.fluent.com>>.

- Folgerø K. 1998 Broad-band dielectric spectroscopy of low-permittivity fluids using one measurement cell. *IEEE Transactions on Instrumentation and Measurement* **47** 881-885.
- Fordham E.J., Ramos R.T., Holmes A., Simonian S., Huang S.M., and Lenn C.P. 1999 Multi-phase-fluid discrimination with local fibre-optical probes: III. Three-phase flows. *Measurement Science and Technology* **10** 1347-1352.
- Fossa M. 1998 Design and performance of a conductance probe for measuring liquid fraction in two-phase gas-liquid flow. *Flow Measurement and Instrumentation* **9** 103-109.
- Gamio J.C., Yang W.Q., and Stott A.L. 2001 Analysis of non-ideal characteristics of an ac-based capacitance transducer for tomography. *Measurement Science and Technology* **12** 1076-1082.
- García-Golding F., Giallorenzo M., Moreno N., and Chang V. 1995 Sensor for determining the water-content of oil-in-water emulsion by specific admittance measurement. *Sensors and Actuators A* **47** 337-341.
- Gardner J.W., Pike A., de Rooij N.F., Koudelka-Hep M., Clerc P.A., Hierlemann A., and Opel W.G. 1995 Integrated array sensor for detecting organic solvents. *Sensors and Actuators B* **26-27**, 135–139.
- Georgakopoulos D., Yang W.Q., and Waterfall R.C. 2003 Best value design of electrical tomography systems. In: *Proceedings of 3rd World Congress on Industrial Process Tomography*, Banf, Canada, 2003.
- Geraci G., Azzopardi B.J., and van Maanen H.R.E. 2007 Effect of inclination on circumferential film thickness variation in annular gas/liquid flow. *Chemical Engineering Science* **62** 3032-3042.
- Geraets J.J.M. and Borst J.C. 1988 A capacitance sensor for two-phase void fraction measurement and flow pattern identification. *International Journal of Multiphase Flow* **14** 305-320.
- Ghajar A.J. 2005 Non-boiling heat transfer in gas-liquid flow in pipes: a tutorial. *Journal of the Brazilian Society of Mechanical Sciences and Engineering* **27** 46-73.
- Gregory A.P. and Clarke R.N. 2006 A review of RF and microwave techniques for dielectric measurements on polar liquids. *IEEE Transactions on Dielectrics and Electrical Insulation* **13** 727-743

- Hall L.D. 2005 Roles for magnetic resonance imaging in process tomography. *IEEE Sensors Journal* **5** 125-133.
- Hammer E.A., Johansen G.A., Dyakowski T, Roberts E.P.L., Cullivans J.C., Williams R.A., Hassan Y.A., and Claiborn C.S. 2006 Advanced experimental techniques. In: *Multiphase Flow Handbook*, Crowe C.T. (ed), Boca Raton: CRC Press.
- Hampel U., Bieberle A., Hoppe D., Kronenberg J., Schleicher E., Suhnel T., Zimmermann F., and Zippe C. 2007 High resolution gamma ray tomography scanner for flow measurement and non-destructive testing applications. *Review of Scientific Instruments* **78** 103704.
- Hassan Y.A. 2002 Multiphase bubbly flow visualization using particle image velocimetry. *Annals of the New York Academy of Sciences* **972** 223-228.
- Hayt W.H. and Buck J.A. 2000 *Engineering Electromagnetics*, 6th ed. Boston: McGraw-Hill.
- Heindel T.J., Gray J.N., and Jensen T.C. 2008 An X-ray system for visualizing fluid flows. *Flow Measurement and Instrumentation* (in press)
doi:10.1016/j.flowmeasinst.2007.09.003
- Hermes T., Bühner M., Bücher S., Sundermeier C., Dumschat C., Borchardt M., Cammann K., and Knoll M. 1994 An amperometric microsensor array with 1024 individually addressable elements for two-dimensional concentration mapping. *Sensors and Actuators B* **21**, 33-37.
- Hernandez Perez V., Azzopardi B.J., and Morvan H. 2007 Slug flow in inclined pipes. In: *Proceedings of 6th International Conference on Multiphase Flow 2007*, Leipzig, Germany, July 9 – 13, 2007, Paper No. S5_Thu_C_53.
- Hervieu E., Jouet E., and Desbat L. 2002 Development and validation of an x-ray tomograph for two-phase flow *Annals of the New York Academy of Sciences* **972** 87–94.
- Hewitt G.F. 1978 *Measurement of Two Phase Flow Parameters*. London: Academic Press.
- Hewitt G.F. 1999 Introduction and basic models, p. 197-203. In: *Handbook of Phase Change, Boiling and Condensation*, S.G. Kandlikar, M. Shoji and V.K. Dhir (eds), Philadelphia: Taylor & Francis.
- Hewitt G.F. 2005 Three-phase gas-liquid-liquid flows in the steady and transient states. *Nuclear Engineering and Design* **235** 1303–1316.

- Hindle F.P., Carey S.J., Ozanyan K., Winterbone D.E., Clough E., and McCann H. 2001 Measurement of gaseous hydrocarbon distribution by a near-infrared absorption tomography system. *Journal of Electronic Imaging* **10** 593-600.
- Hjertaker B.T., Tjugum S.-A., Hammer E.A. and Johansen G.A. 2005 Multimodality tomography for multiphase hydrocarbon flow measurements. *IEEE Sensors Journal* **5** 153-160.
- Höller H. 2000 *Hydrodynamic Couplings with Constant Filling*. Publication No. cr584, Voith Turbo.
Available at <<http://www.voithturbo.com/publications-media.php3>>
- Hori K., Fujimoto T., and Kawanishi K. 1998 Development of ultra-fast X-ray computed tomography scanner system. *IEEE Transactions on Nuclear Science* **45** 2089-2094.
- Hoyle B.S. 1996 Process tomography using ultrasonic sensors. *Measurement Science and Technology* **7** 272-280.
- Hoyle B.S., Jia X., Podd F.J.W., Schlager H.I., Tan H.S., Wang M., West R.M., Williams R.A., and York T.A. 2001 Design and application of a multi-modality process tomography system. *Measurement Science and Technology* **12** 1157-1165.
- Hu B., Stewart C., Hale C.P., Lawrence C.J., Hall A.R.W., Zwiens H., and Hewitt G.F. (2005) Development of an X-ray computed tomography (CT) system with sparse sources: application to three-phase pipe flow visualization. *Experiments in Fluids* **39** 667-678.
- Huang S.M., Plaskowski A.B., Xie C.G., and Beck M.S. 1989 Tomographic imaging of two-component flow using capacitance sensors. *Journal of Physics E: Scientific Instruments* **22** 173-177.
- Huang S.M., Stott A.L., Green R.G., and Beck M.S. 1988 Electronic transducers for industrial measurement of low value capacitances. *Journal of Physics E: Scientific Instruments* **21** 242-250.
- Hussein E.M.A., Meneley D.A., and Banerjee S. 1986 Single exposure neutron tomography of two-phase flow. *International Journal of Multiphase Flow* **12** 1-36.
- ISO 1995 *Guide to the Expression of Uncertainty in Measurement*. Geneva: ISO Publishing.

- Jana A.K., Mandal T.K., Chakrabarti D.P., Das G., and Das P.K. 2007 An optical probe for liquid-liquid two-phase flows. *Measurement Science and Technology* **18** 1563-1575.
- Johansen G.A., Froystein T., Hjertaker B.T., and Olsen Ø 1996 A dual sensor flow imaging tomographic system. *Measurement Science and Technology* **7** 297-307.
- Johansen G.A. 2005 Nuclear tomography methods in industry. *Nuclear Physics A* **752** 696c-705c.
- Jones O.C. and Delhay J.M. 1976 Transient and statistical measurement techniques for two-phase flows. *International Journal of Multiphase Flow* **3** 89-116.
- Kaatze U. and Feldman Y. 2006 Broadband dielectric spectrometry of liquids and biosystems. *Measurement Science and Technology* **17** R17-R35.
- Kak A.C. and Slaney M. 1988 *Principles of Computerized Tomographic Imaging*. New York: IEEE Press.
- Keskin C. and Zhang H.-Q. 2007 Identification and classification of new three-phase gas/oil/water flow patterns. In: *2007 SPE Annual Technical Conference and Exhibition*, Anaheim, CA, USA, 11-14 November.
- Kim S. and Ishii M. 2001 Micro four-sensor probe measurement of interfacial area transport for bubbly flow in round pipes. *Nuclear Engineering and Design* **205** 123-131.
- Kumar S.B., Moslemian D., Dudukovic M.P. 1995 A γ -ray tomographic scanner for imaging voidage distribution in two-phase flow systems. *Flow Measurements and Instrumentation* **6** 61-73.
- Lage P.L.C. and Esposito R.O. 1999 Experimental determination of bubble size distributions in bubble columns: Prediction of mean bubble diameter and gas hold up. *Powder Technology* **101** 142-150.
- Letton W., Svaeren J.A., and Conort G. 1997 Topside and subsea experience with the multiphase flow meter. In: *SPE Annual Technical Conference*, San Antonio, USA, 5-8 October, Paper No. 38783.
- Li X.B., Larson S.D., Zyuzin A.S., and Mamishev A.V. 2006 Design principles for multichannel fringing electric field sensors. *IEEE Sensors* **6** 434-440.
- Lide D.R. (ed) 2005 *CRC Handbook of Chemistry and Physics*, 85th ed. Boca Raton, FL: CRC Press, pp. 6-155 - 6-177.

- Lucas G.P., Cory J., Waterfall R.C., Loh W.W., and Dickin F.J. 1999 Measurement of the solids volume fraction and velocity distributions in solids–liquid flows using dual-plane electrical resistance tomography. *Flow Measurement and Instrumentation* **10** 249–258.
- Ma Y., Chung N., Pei B., and Lin W. (1991) Two simplified methods to determine void fractions for two phase flow. *Nuclear Technology* **94** 124–133.
- Macdonald J.R. 1987 *Impedance Spectroscopy*. New York: John Wiley & Sons.
- Mamishv A.V., Sundara-Rajan K., Yang F., Du Y., and Zahn M. 2004 Interdigital sensors and transducers. *Proceedings of the IEEE* **92**, 808–845.
- Manera A, Prasser H.-M, Lucas D., and van der Hagen T.H.J.J. 2006 Three-dimensional flow pattern visualization and bubble size distributions in stationary and transient upward flashing flow. *International Journal of Multiphase Flow* **32** 996–1016.
- Mantle M.D. and Sederman A.J. 2003 Dynamic MRI in chemical process and reaction engineering. *Progress in Nuclear Magnetic Resonance Spectroscopy* **43** 3–60.
- Marashdeh Q., Warsito W., Fan L.-S., and Teixeira F.L. 2007 A Multimodal Tomography System Based on ECT Sensors. *IEEE Sensors Journal* **7** 426–433.
- McCann H., Scott D.M. (eds.) 2005 *Process Imaging For Automatic Control*. Boca Raton, FL: CRC Press.
- McKeen T.R. and Pugsley T.S. 2002 The influence of permittivity models on phantom images obtained from electrical capacitance tomography. *Measurement Science and Technology* **13** 1822–1830.
- Mishra R., Singh S.N., and Seshadri V 1997 Velocity measurement in solid-liquid flows using an impact probe. *Flow Measurement and Instrumentation* **8** 157–165.
- Morris A.S. 2001 *Measurement and Instrumentation Principles*. Oxford: Butterworth-Heinemann.
- Mukhopadhyay S.C. 2005 Novel planar electromagnetic sensors: Modeling and performance evaluation. *Sensors* **5** 546–579.
- Nelson S., Kraszewski A., and You T. 1991 Solid and particulate material permittivity relationships. *Journal of Microwave Power and Electromagnetic Energy* **26** 45–51.
- Oddie G. and Pearson J.R.A. 2004 Flow-rate measurement in two-phase flow. *Annual Review of Fluid Mechanics* **36** 149–172.

- Oliver B.M. and Cage J.M. 1971 *Electronic Measurements and Instrumentation*. New York: McGraw-Hill.
- OpenCFD Limited 2008 *OpenFOAM: The Open Source Computational Fluid Dynamics* [online]. [Accessed 10th March 2008]:
<<http://www.opencfd.co.uk/openfoam/index.html>>.
- Pallas-Areny R. and Webster J.G. 2001 *Sensors and Signal Conditioning*, 2nd ed. New York: Wiley.
- Parker D.J. and McNeil P.A. 1996 Positron emission tomography for process applications. *Measurement Science and Technology* **7** 287–296.
- Parker D.J., Broadbent C.J., Fowles P., Hawkesworth M.R., and McNeil P.A. 1993 Positron emission particle tracking - a technique for studying flow within engineering equipment. *Nuclear Instruments and Methods in Physics Research A* **326** 592–607.
- Perkin R.G. and Lewis E.L. 1980 The practical salinity scale 1978: Fitting the data. *IEEE Journal of Oceanic Engineering* **5** 9–16.
- Peyton A.J., Yu Z.Z., Lyon G., Al-Zeibak S., Ferreira J., Velez J., Linhares F., Borges A.R., Xiong H.L., Saunders N.H., and Beck M.S. 1996 An overview of electromagnetic inductance tomography: Description of three different systems. *Measurement Science and Technology* **7** 261–271.
- Pietruske H. and Prasser, H.-M. 2007 Wire-mesh sensors for high-resolving two-phase flow studies at high pressures and temperatures. *Flow Measurement and Instrumentation* **18** 87–94.
- Prasser H.-M., Böttger A., and Zschau J. 1998 A new electrode-mesh tomograph for gas-liquid flows. *Flow Measurement and Instrumentation* **9** 111–119.
- Prasser H.-M., Scholz D., and Zippe C. 2001 Bubble size measurement using wire-mesh sensors. *Flow Measurement and Instrumentation* **12** 299–312.
- Prasser H.-M., Krepper E., and Lucas D. 2002a Evolution of the two-phase flow in a vertical tube - decomposition of gas fraction profiles according to bubble size classes using wire-mesh sensors. *International Journal of Thermal Sciences* **41** 17–28.
- Prasser H.-M., Zschau J., Peters D., Pietzsch G., Taubert W., and Trepte M. 2002b Fast wire-mesh sensors for gas-liquid flows visualization with up to 10 000 frames per second. In: *Proc. Int. Congr. on Advanced Nuclear Power Plants*, Hollywood, USA, 2002. Paper #1055.

- Prasser H.-M., Grunwald G., Höhne T., Kliem S., Rohde U., and Weiss F.-P. 2003 Coolant mixing in a pressurized water reactor: Deboration transients, steam-line breaks, and emergency core cooling injection. *Nuclear Technology* **143** 37-56
- Prasser H.-M., Beyer M., Böttger A., Carl H., Lucas D., Schaffrath A., Schütz P., Weiss F.P., and Zschau J. 2005a Influence of the pipe diameter on the structure of the gas-liquid interface in a vertical two-phase pipe flow. *Nuclear Technology* **152** 3-22.
- Prasser H.-M., Misawa M., and Tiseanu I. 2005b Comparison between wire-mesh sensor and ultra-fast x-ray tomograph for an air-water flow in a vertical pipe. *Flow Measurement and Instrumentation* **16** 73-83.
- Prasser H.-M., Beyer M., Carl H., Gregor S., Lucas D., Pietruske H., Schütz P., and Weiss F.-P. 2007 Evolution of the structure of a gas-liquid two-phase flow in a large vertical pipe. *Nuclear Engineering and Design* **237** 1848-1861.
- Prasser H.-M. 2008 Novel experimental measuring techniques required to provide data for CFD validation *Nuclear Engineering and Design* **238** 744-770.
- Rahiman M.H.F., Rahim R.A., Rahiman M.H.F., and Tajjudin M. 2006 Ultrasonic transmission-mode tomography imaging for liquid/gas two-phase flow. *IEEE Sensors Journal* **6** 1706 - 1715.
- Raju G.G. 2003 *Dielectrics in Electric Fields*. New York: CRC Press.
- Ramo S., Whinnery J.R., and Van Duzer T. 1994 *Fields and Waves in Communications Electronics*. New York: John Wiley & Sons.
- Ramos R.T., Holmes A., Wu X., and Dussan E. 2001 A local optical probe using fluorescence and reflectance for measurement of volume fractions in multi-phase flows. *Measurement Science and Technology* **12** 871-876.
- Reyes Jr. J.N., Lafi A.Y., and Saloner D. 1998 The use of MRI to quantify multi-phase flow patterns and transitions: An application to horizontal slug flow. *Nuclear Engineering and Design* **184** 213-228.
- Reinecke N., Boddem M., Petritsch G., Mewes D. (1996) Tomographisches Messen der relativen Phasenanteile in zweiphasigen Strömungen fluidier Phasen. *Chemie Ingenieur Technik* **68** 1404-1412.
- Reinecke N., Petritsch G., Boddem M., Mewes D (1998) Tomographic imaging of the phase distribution in two-phase slug flow. *International Journal of Multiphase Flow* **24** 617-634.

- Richter S., Aritomi M., Prasser H.-M., and Hampel R. 2002 Approach towards spatial phase reconstruction in transient bubbly flow using a wire-mesh sensor. *International Journal of Heat and Mass Transfer* **45** 1063-1075.
- Rohde U., Kliem S., Höhne T., Karlsson R., Hemström B., Lillington J., Toppila T., Elter J., and Bezrukov Y. 2005 Fluid mixing and flow distribution in the reactor circuit, measurement data base. *Nuclear Engineering and Design* **235** 421-443.
- Rouhani S.Z. and Sohal M.S. 1983 Two-phase flow patterns: a review of research results. *Progress in Nuclear Energy* **11** 219-259.
- Ruzairi A.R. and Chan K.S. 2004 Optical tomography system for process measurement using light emitting diodes as a light source. *Optical Engineering* **43** 1251-1257.
- Rzasa M.R. and Plaskowski A. 2003 Application of optical tomography for measurements of aeration parameters in large water tanks. *Measurement Science and Technology* **14** 199-204.
- Sami M., Abouelwafa A.A., and Kendall J.M. 1980 The use of capacitance for phase percentage determination in multiphase pipelines. *IEEE Transactions on Measurement and Instrumentation* **29** 24-27.
- Scheicher E., Sühnel T., Boden D., Fischer F., and Futterschneider H. 2007 *Gittersensor* Patent application DE 10 2007 019926.2-52.
- Schleicher E., Da Silva M.J., and Hampel U. 2008a Enhanced local void and temperature measurements for highly transient two-phase flows. *IEEE Transactions on Instrumentation and Measurement* **57** 401-405.
- Schleicher E., Hampel U., Da Silva M.J., Thiele S., Li A., and Wollrab E. 2008b Design of an optical tomograph for the investigation of single and two phase pipe flows *Measurement Science and Technology* **19** (in press).
- Stott A.L., Green R.G., and Seraji K. 1985 Comparison of the use of internal and external electrodes for the measurement of the capacitance and conductance of fluids in pipes. *Journal of Physics E: Scientific Instruments* **18** 587-592.
- Supardan M.D., Masuda Y., Maezawa A., and Uchida S. 2007 The investigation of gas holdup distribution in a two-phase bubble column using ultrasonic computed tomography. *Chemical Engineering Journal* **130** 125-133.
- Tapp H.S., Peyton A.J., Kemsley E.K., and Wilson R.H. 2003 Chemical engineering applications of electrical process tomography. *Sensors and Actuators B* **92** 17-24.

- Tayebi D., Svendsen H.F., Jakobsen H.A., and Grislingas A. 2001 Measurement techniques and data interpretations for validating CFD multi phase reactor models. *Chemical Engineering Communications* **186** 56-159.
- Thiele S. 2007 *Entwicklung und Aufbau eines kapazitiven Oberflächensensors für die Phasenverteilung- und Geschwindigkeitsmessung zweiphasiger Strömungen*. Diploma Thesis, Technische Universität Dresden, Dresden, Germany.
- Thiele S., Da Silva M.J., and Hampel U. 2008 Capacitive planar array sensor for high-speed multiphase flow imaging. *IEEE Sensors Journal* (submitted)
- Tsochatzidis N.A., Karapantios T.D., Kostoglou M.V., and Karabelas A.J. 1992 A conductance method for measuring liquid fraction in pipes and packed beds. *International Journal of Multiphase Flow* **5** 653-667.
- Vaibar R., Sühnel T., Da Silva M.J. 2007 Buoyancy driven turbulent flow and experimental validation at the VeMix test facility. *Applied and Computational Mechanics* **1**, 677-684.
- Wang H.X., Yin W., Yang W.Q., and Beck M.S. 1996 Optimum design of segmented capacitance sensing array for multi-phase interface measurement. *Measurement Science and Technology* **7** 79-86.
- Wangjiraniran W., Motegi Y., Richter S., Kikura H., Aritomi M., and Yamamoto K. 2003 Intrusive effect of wire mesh tomography on gas-liquid flow measurement. *Journal of Nuclear Science and Technology* **40** 932-940.
- Werther J. 1999 Measurement techniques in fluidized beds. *Powder Technology* **102** 15-36.
- Williams R.A. and Beck M.S. (eds.) 1995 *Process Tomography: Principles, Techniques and Applications*. Oxford, UK: Butterworth-Heinemann.
- Williams R.A. and Jia X. 2003 Tomographic imaging of particulate systems. *Advanced Powder Technology* **14** 1-16.
- Wittstock G. 2002 Sensor arrays and array sensors. *Analytical and Bioanalytical Chemistry* **372**, 16-17.
- Wollrab E. 2006 *Entwicklung eines Kapazitätsgittersensors für die Untersuchung von Mehrphasenströmungen*. Diploma Thesis, Hochschule für Technik und Wirtschaft, Dresden, Germany.
- Wörner M. 2003 A compact introduction to the numerical modeling of multiphase flows. *Report Forschungszentrum Karlsruhe, FZKA 6932*.
Available at: <http://bibliothek.fzk.de/zb/berichte/FZKA6932.pdf>

- Xie C.G., Reinecke N., Beck M.S., Mewes D., and Williams R.A. 1995 Electrical tomography techniques for process engineering applications. *The Chemical Engineering Journal* **56** 127-133.
- Yang M., Schlager H.I., Hoyle B.S., Beck M.S., and Lenn C. 1999 Real-time ultrasound process tomography for two-phase flow imaging using a reduced number of transducers *IEEE Transactions on Ultrasonics, Ferroelectrics and Frequency Control* **46** 492-501.
- Yang W.Q. and Peng L. 2003 Image reconstruction algorithms for electrical capacitance tomography. *Measurement Science and Technology* **14** R1-R13.
- Yang W.Q. and York T.A 1999 New ac-based capacitance tomography system. *IEE Proceedings - Science, Measurement and Technology* **146** 47-53.
- Yeung H. 2007 Multiphase flow measurement - the holy grail. In: *SENSOR Conference 2007 Proceedings I*, May 2007, Nurnberg, Germany, p. 193-197.
- York T.A. 2001 Status of electrical tomography in industrial applications. *Journal of Electronic Imaging* **10** 608-619.
- Zaruba A., Krepper E. Prasser H.-M., and Schleicher E. 2005 Measurement of bubble velocity profiles and turbulent diffusion coefficients of the gaseous phase in rectangular bubble column using image processing. *Experimental Thermal and Fluid Science* **29** 851-860.

Appendix A – List of author's publications

This thesis is in part based on the following papers:

- Thiele S., Da Silva M.J., and Hampel U. 2008 Capacitive planar array sensor for high-speed multiphase flow imaging. *IEEE Sensors Journal* (in press).
- Da Silva M.J., Lu Y., Sühnel T., Schleicher E., Thiele S., Kernchen R., and Hampel U. 2008 Autonomous planar conductivity array sensor for fast liquid distribution imaging in a fluid coupling. *Sensors and Actuators A* **147** 508-515.
- Da Silva M. J., Sühnel T., Schleicher E., Vaibar R., Lucas D., and Hampel U. 2007 Planar array sensor for high-speed component distribution imaging in fluid flow applications. *Sensors* **7** 2430-2445.
- Da Silva M.J., Schleicher E., and Hampel U. 2007 Capacitance wire-mesh sensor for fast measurement of phase fraction distributions. *Measurement Science and Technology* **18** 2245-2251.
- Da Silva M.J., Schleicher E., and Hampel U. 2007 A novel needle probe based on high-speed complex permittivity measurements for investigation of dynamic fluid flows. *IEEE Transactions on Instrumentation and Measurement* **56** 1249-1256.
- Da Silva M.J., Schleicher E. and Hampel U. 2005 Neue Konzepte für die kombinierte Leitfähigkeits- und Impedanzmessung in hochtransienten Mehrphasenströmungen. In: *Proceedings of 7. Dresdner Sensor-Symposium*, p. 139-142, Dresden, Germany, December 2005.

Publications not included in this thesis (selected):

- Hampel U., Hoppe D., Bieberle A., Kernchen R., Diele K.-H., Schleicher E., Da Silva M.J., and Zippe C. 2008 Measurement of fluid distributions in a rotating fluid coupling using high resolution gamma ray tomography. *Journal of Fluids Engineering* **130** 091402.

Schleicher E., Da Silva M.J., and Hampel U. 2008a Enhanced local void and temperature measurements for highly transient two-phase flows. *IEEE Transactions on Instrumentation and Measurement* **57** 401-405.

Schleicher E., Hampel U., Da Silva M.J., Thiele S., Li A., and Wollrab E. 2008b Design of an optical tomograph for the investigation of single and two phase pipe flows. *Measurement Science and Technology* **19** 094006.

Vaibar R., Sühnel T., Da Silva M.J. 2007 Buoyancy driven turbulent flow and experimental validation at the VeMix test facility. *Applied and Computational Mechanics* **1** 677-684.

Supervised diploma theses:

Thiele S. 2007 *Entwicklung und Aufbau eines kapazitiven Oberflächensensors für die Phasenverteilung- und Geschwindigkeitsmessung zweiphasiger Strömungen*. Diploma Thesis, Technische Universität Dresden, Dresden, Germany.

Wollrab E. 2006 *Entwicklung eines Kapazitätsgittersensors für die Untersuchung von Mehrphasenströmungen*. Diploma Thesis, Hochschule für Technik und Wirtschaft, Dresden, Germany.

Brückner F. 2005 *Impedanzmessung mehrphasiger Fluide*. Diploma Thesis, Hochschule für Technik und Wirtschaft, Dresden, Germany.

Patents:

Schleicher E., Ritterath M., Da Silva M.J. and Hampel U. 2007 *Anordnung zur zweidimensionalen Messung der Temperaturverteilung in einem Messquerschnitt* DE 10 2007 019 925 (patent application).

Da Silva M.J., Schleicher E., Hampel U. and Prasser, H.-M. 2006 *Grid Sensor for the Two-Dimensional Measurement of Different Components in the Cross Section of a Multiphase Flow*. WO 2007 121708 A1, DE 10 2006 019178 A1.

Schleicher E., Da Silva M.J. and Hampel, U. 2005 *Assembly for Measuring the Local Electric Impedance and Temperature of Fluids*. DE 10 2005 046 662 B3, EP 1 929 262 A1, WO 2007 36195 A1.

Appendix B – Electromagnetic theory

In this appendix, some background information on the electromagnetic theory is presented.

B.1 Maxwell's equations

The most general formulation of the laws of electricity and magnetism is due to Maxwell who in 1864 unified the observations of Faraday, Gauss and Ampere in the following four equations

$$\nabla \times \mathbf{E}(\mathbf{r}, t) = -\frac{\partial \mathbf{B}(\mathbf{r}, t)}{\partial t} \quad (\text{Faraday's law}) \quad (\text{B.1})$$

$$\nabla \times \mathbf{H}(\mathbf{r}, t) = \mathbf{J}(\mathbf{r}, t) + \frac{\partial \mathbf{D}(\mathbf{r}, t)}{\partial t} \quad (\text{Ampere's law}) \quad (\text{B.2})$$

$$\nabla \cdot \mathbf{D}(\mathbf{r}, t) = \rho(\mathbf{r}, t) \quad (\text{Gaussian law}) \quad (\text{B.3})$$

$$\nabla \cdot \mathbf{B}(\mathbf{r}, t) = 0 \quad (\text{Gaussian law}) \quad (\text{B.4})$$

where the field variables are defined as:

E:	electric field strength	(V/m)
D:	electric displacement	(C/m ²)
H:	magnetic field strength	(A/m)
B:	magnetic flux density	(T; tesla)
J:	electric current density	(A/m ²)
ρ:	electric charge density	(C/m ³)

and \mathbf{r} and t are position vector and time, respectively. A good introductory textbook on electromagnetic theory is that one of Hayt and Buck (2000).

In order to solve electrodynamic problems, a further set of relationships among the field quantities \mathbf{D} , \mathbf{E} , \mathbf{B} , and \mathbf{H} must be established as there are more variables than equations contained within Maxwell's equations. These additional equations are known as constitutive relations and they arise from physical consideration of the media in the problem to be solved. The constitutive relations for an isotropic medium can be written simply as

$$\mathbf{D}(\mathbf{r}, t) = \varepsilon_0 \varepsilon \mathbf{E}(\mathbf{r}, t) \quad (\text{B.5})$$

$$\mathbf{B}(\mathbf{r}, t) = \mu_0 \mu \mathbf{H}(\mathbf{r}, t) \quad (\text{B.6})$$

where μ is the relative magnetic permeability and ε the relative electric permittivity. It has to be noted that the usual symbol for the relative permeability is μ_r and for relative permittivity is ε_r , but the subscripts are omitted for the sake of clarity, noting that μ and ε are dimensionless. In free space void of any matter, $\mu_0 = 4\pi \cdot 10^{-7}$ H/m and $\varepsilon_0 = 8.85 \cdot 10^{-12}$ F/m. Equations (B.5) and (B.6) assume an isotropic medium, whereby under isotropy is meant that the field vector \mathbf{E} is parallel to \mathbf{D} and the field vector \mathbf{H} is parallel to \mathbf{B} . In the case of anisotropic media, μ and ε become tensors, however these analyses is referred to a more advanced book (e.g. Ramo *et al.* 1994).

A third constitution relation is the Ohm's law

$$\mathbf{J}(\mathbf{r}, t) = \sigma \mathbf{E}(\mathbf{r}, t) \quad (\text{B.7})$$

where σ is the material's electrical conductivity (in S/m).

In linear media described by isotropic constitutive relations, the Maxwell's equations are linear and therefore the superposition principle can be used to decompose any time varying fields into a series of time harmonics for which solutions can be readily obtained. This procedure amounts to taking a Fourier transform of equations (B.1) to (B.4) which yields Maxwell's equations in the frequency domain.

$$\nabla \times \mathbf{E} = -j\omega \mathbf{B} \quad (\text{B.8})$$

$$\nabla \times \mathbf{H} = \mathbf{J} + j\omega \mathbf{D} \quad (\text{B.9})$$

$$\nabla \cdot \mathbf{D} = \rho \quad (\text{B.10})$$

$$\nabla \cdot \mathbf{B} = 0 \quad (\text{B.11})$$

The field variables are now expressed with the complex phasor convention. According to this convention, fields can be described by $\mathbf{E}(\mathbf{r}, t) = \text{Re}\{\mathbf{E} \exp(j\omega t)\}$, and so forth.

The constitutive equations are also updated for the frequency domain notation

$$\mathbf{D} = \varepsilon_0 \varepsilon \mathbf{E} \quad (\text{B.12})$$

$$\mathbf{B} = \mu_0 \boldsymbol{\mu} \mathbf{H} \quad (\text{B.13})$$

where ε and $\boldsymbol{\mu}$ are now complex quantities denoting complex permittivity and complex permeability, respectively. In this work, only dielectric materials were investigated so that the magnetic properties may be considered to be equal to vacuum, i.e. $\mu = 1$.

a) Electrostatic approximation and Poisson's equation

The electrostatic approximation of Maxwell's equations assumes that the rate of change of the magnetic field is low (or absent), hence

$$\frac{\partial \mathbf{B}}{\partial t} \approx 0. \quad (\text{B.14})$$

From Faraday's law (B.1), this implies that the electrical field \mathbf{E} is irrotational, i.e.

$$\nabla \times \mathbf{E} = 0. \quad (\text{B.15})$$

Furthermore, it is possible to express the electric field \mathbf{E} as the gradient of a scalar function, called the electrostatic potential or voltage V

$$\mathbf{E} = -\nabla V. \quad (\text{B.16})$$

Using this fact together with the Gaussian law (B.3) and the constitutive relation (B.5), yields

$$\nabla(\varepsilon_0 \varepsilon \nabla V) = \boldsymbol{\rho}, \quad (\text{B.17})$$

which is the Poisson's equation with spatially varying permittivity. The equation is linear, and the principle of superposition may be applied (Hayt and Buck 2000).

B.2 Polarization

When an external electric field is applied to a dielectric material (or insulator) where only relatively few free charges exist, the so-called bounded charges can be displaced or stretched. In such cases, the atom or molecule of the material forms an electric dipole that maintains an electric field. Consequently, each volume element of the material behaves as an electric dipole. The dipole field tends to oppose the applied field. Dielectric materials that exhibit non-zero distribution of such bound charge separations are said to be polarized. When a material is linear and isotropic in nature, the polarization density \mathbf{P} is related to applied electric field intensity \mathbf{E} as follows

$$\mathbf{P} = \varepsilon_0 \chi_e \mathbf{E}. \quad (\text{B.18})$$

where χ_e is called the electric susceptibility of the material. The electric polarization vector \mathbf{P} is an auxiliary vector in electrodynamics that accounts for the creation of atomic dipoles in a material due to an applied electric field. The polarization is hidden in the constitute equation (B.5) in the following way

$$\mathbf{D} = \varepsilon_0 \mathbf{E} + \mathbf{P} = \varepsilon_0 (1 + \chi_e) \mathbf{E} = \varepsilon_0 \varepsilon \mathbf{E}, \quad (\text{B.19})$$

where the electric displacement \mathbf{D} was separated into a vacuum contribution $\varepsilon_0 \mathbf{E}$, and one arising from the material \mathbf{P} . The relative permittivity of a material is thus given by $\varepsilon = 1 + \chi_e$.

The relationship (B.19) is the constitutive equation for the static case. In a time varying electric field the polarization is frequency-dependent. Polarization of a material may be classified according interfacial, orientational, atomic and electronic polarization mechanisms; each of them having a characteristic frequency where it occurs. The time required for polarization to occur is directly related to the distance over which charge is being displaced and the ease with which it can be displaced. Interfacial polarization which depends on the detailed electrode configuration is generally not observed at frequencies above 100 Hz. Orientational (or dipole) polarization typically takes place at microwave frequencies. Atomic polarization arises with molecular vibrations at frequencies around GHz and THz and electronic polarization shows up at infrared to ultraviolet range (10^{14} - 10^{16} Hz). For a detailed description on these phenomena see Raju (2003).

The frequency domain response of a dielectric medium may also be written in terms of the dielectric permittivity which is defined by the constitutive relation (B.12) in frequency domain, where

$$\epsilon = (\epsilon' - j\epsilon'') \quad (\text{B.20})$$

is the complex permittivity comprising a real part ϵ' (commonly called the permittivity) and imaginary part ϵ'' or the loss factor. In the case that the medium has several polarization mechanisms coexisting and not significantly interacting among themselves, the complex permittivity can be expressed as the sum of the contributions of the individual mechanisms:

$$\epsilon(\omega) = 1 + \sum_i \chi_i'(\omega) - j \sum_i \chi_i''(\omega) = \epsilon'(\omega) - j\epsilon''(\omega) \quad (\text{B.21})$$

where summation extends over all the separate polarization mechanisms labeled with the index i .

Figure B.1 illustrates an exemplary function for (B.21). The real part of the permittivity $\epsilon'(\omega)$ is made up of contributions of all loss processes at frequencies higher than the frequency in question. Though in Figure B.1 the polarization mechanisms are shown, for the sake of clarity, as distinct and clearly separable, in reality the peaks may be broader and often overlap.

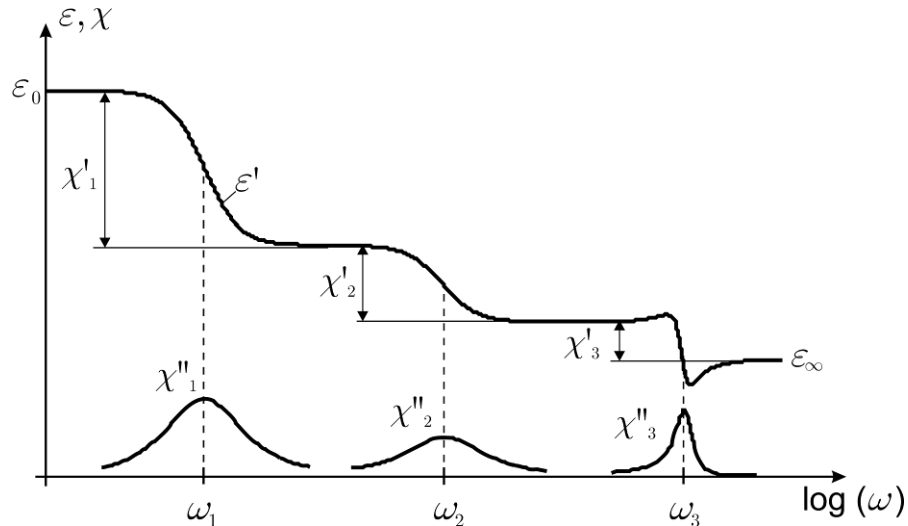


Figure B.1: Schematic illustration of different polarization mechanisms. Three contributing processes are shown denoted by the subscripts $i = 1, 2$ and 3 . The processes associated with χ_1 and χ_2 are Debye-type relaxation processes and χ_3 is a resonance process.

B.3 Debye relaxation model

When a direct voltage applied to a dielectric for a sufficiently long duration is suddenly removed, the decay of polarization to zero value is not instantaneous but takes a finite time. This is the time required for the dipoles to revert to a random distribution, in equilibrium with the temperature of the medium, from a field-oriented alignment. Similarly, the building up of polarization following the sudden application of a direct voltage takes also a finite time interval before the polarization attains its maximum value. This phenomenon is described by the general term dielectric relaxation.

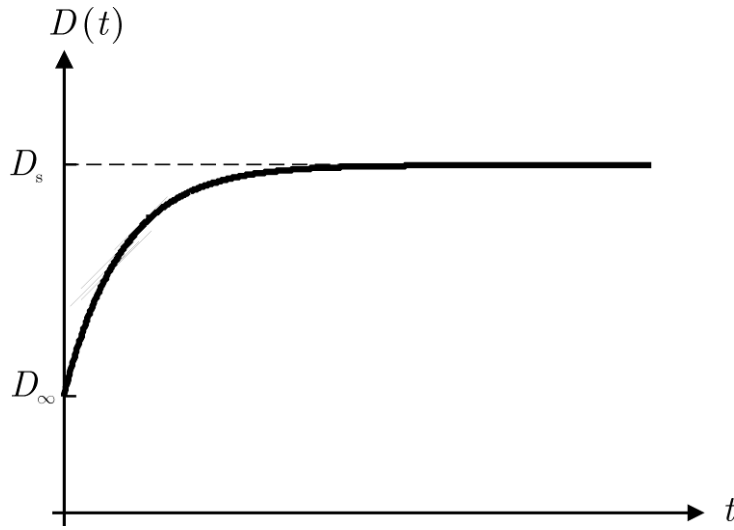


Figure B.2: Transient response of a generic sample showing single relaxation.

In the simplest case, the polarization of a sample will relax towards the steady state as a first-order process characterized by a single time constant τ . A typical transient response on the application of a unit step function is given in Figure B.2. This has the form

$$D(t) = D_{\infty} + (D_s - D_{\infty}) \left(1 - \exp\left(-\frac{t}{\tau}\right) \right), \quad (\text{B.22})$$

which is characterized by an instantaneous response D_{∞} following an exponential growth to the static value D_s . From (B.22), this relationship may also be written in terms of permittivity

$$\varepsilon(t) = \varepsilon_{\infty} + (\varepsilon_s - \varepsilon_{\infty}) \left(1 - \exp\left(-\frac{t}{\tau}\right) \right). \quad (\text{B.23})$$

Taking the Laplace transform to convert to the complex frequency (s) domain

$$\frac{\{\varepsilon\}}{s} = \frac{\varepsilon_\infty}{s} + \frac{(\varepsilon_s - \varepsilon_\infty)}{s} - \frac{(\varepsilon_s - \varepsilon_\infty)}{s + 1/\tau} \quad (\text{B.24})$$

where $\{\varepsilon\}$ is the Laplace-transformed function of $\varepsilon(t)$. Rearranging the terms yields

$$\{\varepsilon\} = \varepsilon_\infty + \frac{\varepsilon_s - \varepsilon_\infty}{1 + s\tau}. \quad (\text{B.25})$$

Setting $s = j\omega$ to obtain the frequency domain response

$$\varepsilon = \varepsilon_\infty + \frac{\varepsilon_s - \varepsilon_\infty}{1 + j\omega\tau}, \quad (\text{B.26})$$

which is a single relaxation Debye equation, where ε is the complex permittivity function.

Since all media invariably possess a finite (although, possibly, very small) conductivity σ , this contribution will show up in any measurement of the dielectric response. From Ampere's law (B.9), and the constitutive relations (B.7) and (B.5), one obtains

$$\nabla \times \mathbf{H} = \sigma \mathbf{E} - j\omega\varepsilon \mathbf{E} = j\omega\varepsilon_{\text{eff}} \mathbf{E}, \quad (\text{B.27})$$

where the effective permittivity ε_{eff} was chosen such that

$$\varepsilon_{\text{eff}} = \varepsilon - j \frac{\sigma}{\omega\varepsilon_0}. \quad (\text{B.28})$$

Equation (B.28) demonstrates that static conductivity shows up as losses increase in a dielectric measurement. Furthermore, even if σ is relatively small as it is the case in the insulating fluids, it may dominate ε_{eff} at sufficiently low frequencies. In order to extract the actual complex permittivity ε of the material from the measured permittivity ε_{eff} , an independent measurement of σ is required.

In the general form, by inserting (B.20) into (B.28), one obtains

$$\varepsilon_{\text{eff}} = \varepsilon' - j \left(\varepsilon'' + \frac{\sigma}{\omega\varepsilon_0} \right). \quad (\text{B.29})$$

For the case of low frequencies, where the dielectric losses $\varepsilon'' = 0$ and $\varepsilon' = \varepsilon$ (static relative permittivity)

$$\varepsilon_{\text{eff}} = \varepsilon = \varepsilon - j \frac{\sigma}{\omega\varepsilon_0}. \quad (\text{B.30})$$

Here for the sake of clarity $\epsilon_{\text{eff}} = \epsilon$. This equation was already presented in chapter 3 as (3.20).